University of Tennessee, Knoxville

TRACE: Tennessee Research and Creative Exchange

Masters Theses

Graduate School

12-1995

Zirconia based coatings via chemical vapor deposition

Mark Andrew Borst

Follow this and additional works at: https://trace.tennessee.edu/utk_gradthes

Recommended Citation

Borst, Mark Andrew, "Zirconia based coatings via chemical vapor deposition. " Master's Thesis, University of Tennessee, 1995.
https://trace.tennessee.edu/utk_gradthes/11050

This Thesis is brought to you for free and open access by the Graduate School at TRACE: Tennessee Research and Creative Exchange. It has been accepted for inclusion in Masters Theses by an authorized administrator of TRACE: Tennessee Research and Creative Exchange. For more information, please contact trace@utk.edu.

To the Graduate Council:

I am submitting herewith a thesis written by Mark Andrew Borst entitled "Zirconia based coatings via chemical vapor deposition." I have examined the final electronic copy of this thesis for form and content and recommend that it be accepted in partial fulfillment of the requirements for the degree of Master of Science, with a major in Metallurgical Engineering.

Peter K. Liaw, Major Professor

We have read this thesis and recommend its acceptance:

Woo Y Lee, Thomas Meek

Accepted for the Council:
Carolyn R. Hodges

Vice Provost and Dean of the Graduate School

(Original signatures are on file with official student records.)

To the Graduate Council:

I am submitting herewith a thesis written by Mark Andrew Borst entitled "Zirconia Based Coatings Via Chemical Vapor Deposition". I have examined the final copy of this thesis for form and content and recommend that it be accepted in partial fulfillment of the requirements for the degree of Master of Science in Metallurgical Engineering.

Peter K. Liaw Ph.D., Major Professor

We have read this thesis and
recommend its acceptance

Accepted for the Council:

Associate Vice Chancellor
and Dean of the Graduate School

ZIRCONIA BASED COATINGS VIA CHEMICAL VAPOR DEPOSITION

A Thesis

Presented for the

Master of Science

Degree

The University of Tennessee, Knoxville

Mark Andrew Borst

December 1995

DEDICATION

This work is dedicated to the Horowitz brothers and their colleague, Mr. Fine. I am unable to think of any whose work more accurately delineated institutions of higher learning.

ACKNOWLEDGMENTS

I wish to thank my parents and family for all their support throughout the writing of this thesis as well as my entire life. Also, I would like to acknowledge and thank my major professor, Dr. Peter K. Liaw, and mentor, Dr. Woo Y. Lee, for all their helpful advice in performing this research as well as writing this thesis. I also wish to thank Dr. Thomas Meek for all of his comments and assistance concerning this work. The support and enthusiasm of Dr. Tom Hutchinson was also greatly appreciated. In addition, I would like to thank those at the University of Tennessee and at Oak Ridge National Laboratory who lent time, advice, tolerance or good humor during the writing of this, my Master's thesis. An alphabetical listing follows:

Y. W. Bae, Ph.D.
Theodore Bessman, Ph.D.
Peter J. Blau, Ph.D.
David Braski
Dorothy Coffey
Kevin Cooley
Chuck Herd
Carla Lawrence
Richard Lowden
Sandy Maples
Rebecca Martin
Bill Matlin
Jerry C. Mclaughlin
Patricia Mejia
Jan Palmer
Gary Samples
David Schenk
Otto Schwarz
Subu Shamugham
David Stinton
Michael Stott
Norm Vaughn
Jeffery "Cotton" Williams

Finally, I would be remiss if I did not thank the good people at GROVE Worldwide in Shady Grove, Pennsylvania, for hiring me. I could have never completed this thing if a job hadn't been waiting in the wings.

This research was performed in cooperation with the University of Tennessee under contract No. 11X-SP662V and sponsored by the Laboratory Directed Research Program of Oak Ridge National Laboratory, managed for the Department of Energy by Lockheed Martin Energy Systems, Inc., under contract No. DE-AC05-84OR21400 and in part by the Southeastern Universities Research Association (SURA).

ABSTRACT

This work was concerned with the production of ZrO_2 based coatings using chemical vapor deposition (CVD). Such coatings, produced by air plasma spray and electron beam physical vapor deposition (EBPVD), have seen use as thermal barrier coatings in gas turbine engines.

The coatings which were examined were pure ZrO_2, Y_2O_3-stabilized ZrO_2 and alternating layers of ZrO_2 and Al_2O_3. The selection of Zr precursors for the deposition of ZrO_2 was addressed by studying the chlorination of metallic Zr, the vaporization of $ZrCl_4$ and the vaporization of Zr based metalorganics. Major parameters such as temperature, pressure and reactant flow rates were varied in an attempt to determine the optimum conditions for the deposition of ZrO_2. The effects of these parameters on the microstructure of the ZrO_2 deposits were studied. It was initially intended that once ZrO_2 was satisfactorily deposited, an Y based organometallic might be introduced along with the Zr precursor to stabilize the ZrO_2.

In addition to the deposition of ZrO_2 and Y_2O_3-stabilized ZrO_2 coatings, the formation of a coating which consisted of alternating layers of ZrO_2 and Al_2O_3 was examined to determine the feasibility of and challenges associated with producing such a coating.

It appeared that the chlorination of Zr provided the optimum precursor for the deposition of ZrO_2. The vaporization of $ZrCl_4$ typically resulted in clogged lines while the metalorganic chosen, zirconium tetramethyl heptadionate [$Zr(tmhd)_4$] resulted in coatings with undesirable characteristics. Also, it became evident that the deposition of Y_2O_3-stabilized ZrO_2 was much more difficult than first suspected. Effective parameters were difficult to determine. The Y_2O_3-stabilized ZrO_2 coatings that were produced appeared soft and seemed to be plagued by carbon contamination.

Finally, a coating which consisted of alternating layers of ZrO_2 and Al_2O_3 was produced. The properties of this coating, however, have yet to be fully analyzed.

TABLE OF CONTENTS

CHAPTER	PAGE
1. INTRODUCTION	1
2. LITERATURE SURVEY	5
Deposition of Zirconia	5
Deposition of Yttria	10
Deposition of Yttria-Stabilized Zirconia via Electrochemical Vapor Deposition	12
Deposition of Yttria-Stabilized Zirconia via Plasma Spray	15
Deposition of Yttria-Stabilized Zirconia via Chemical Vapor Deposition	18
Thermal Diffusivity and Conductivity of Yttria-Stabilized Zirconia	31
Failure Mechanism of Thermal Barrier Coatings	37
3: PROJECT OUTLINE	41
4: EXPERIMENTAL APPARATUS	45
Reactor 1	45
Reactor 2	48
Reactor 3	52
Reactor 4	53

CHAPTER	PAGE
5. PROCEDURES	55
Reactor 1	55
Reactor 2	57
Reactor 3	60
Reactor 4	61
6. RESULTS AND DISCUSSION	62
Reactor 1	62
Reactor 2	74
Reactor 3	82
Reactor 4	82
7. CONCLUSIONS	91
8. SUGGESTED FUTURE WORK	93
LIST OF REFERENCES	94
APPENDIX	101
VITA	172

LIST OF FIGURES

FIGURE		PAGE
1.	The effects of supersaturation and temperature on the structure formed by chemical vapor deposition (Reproduced from "Protective Coatings for High Temperature Materials: Chemical Vapor Deposition and Pack Cementation Processes" by Duret and Pichoir[11]).	102
2.	Schematic of column separation during thermal expansion.	102
3.	Schematic diagram of electrochemical vapor deposition (EVD).	103
4.	Comparison of ideal vs. non-ideal YSZ deposition during CVD phase of EVD process.	103
5.	Arrhenius plots of gas-phase and surface reaction rate constants of ZrO_2 and Y_2O_3 (Reproduced from "LPMOCVD of YSZ Thin Film - Experiments and Model Analysis" by Akiyama et al.[29]).	104
6.	Growth rate distributions as determined by Akiyama et al.[29] (Reproduced from "LPMOCVD of YSZ Thin Film - Experiments and Model Analysis" by Akiyama et al.[29]).	104
7.	Growth rate and yttrium composition distributions as determined by Akiyama et al.[29] (Reproduced from "LPMOCVD of YSZ Thin Film - Experiments and Model Analysis" by Akiyama et al.[29]).	105

FIGURE		PAGE
8.	Schematic diagram of temperature profile of turbine blade with TBC and bond coat (Reproduced from "Thermal diffusivity of thermal barrier coatings of ZrO_2 stabilized with Y_2O_3" by Morrell and Taylor[31]).	105
9.	Schematic diagram of first CVD reactor.	106
10.	Photograph of first CVD reactor.	107
11.	Temperature profile of first CVD reactor used for the deposition of zirconia form $ZrCl_4$.	108
12.	Schematic diagram of second CVD reactor constructed for the deposition of zirconia, yttria-stabilized zirconia, nickel aluminide and alumina.	109
13.	Photograph of second CVD reactor constructed for the deposition of zirconia, yttria-stabilized zirconia, nickel aluminide and alumina.	110
14.	Temperature profile of second CVD reactor used for the deposition of zirconia, yttria and yttria-stabilized zirconia from $Zr(tmhd)_4$ and $Y(tmhd)_3$.	111
15.	Schematic diagram of third CVD reactor.	112
16.	Photograph of third CVD reactor used for the deposition of zirconia.	113
17.	Temperature profile of third CVD reactor.	114
18.	Schematic diagram of fourth CVD reactor.	115
19.	Temperature profile of fourth CVD reactor.	116
20.	Theoretical depiction of relationship between growth rate and flow rate.	116

FIGURE		PAGE

21.	Schematic diagram showing possible coating surface.	117
22.	Rate of ZrO_2 deposition vs. temperature at P = 5 Torr.	117
23.	Arrhenius behavior between Ln(deposition rate) and temperature (P = 5 Torr).	118
24.	SEM micrograph of zirconia deposit made on nickel substrate at P = 5 Torr, T = 950 °C (5,000X).	119
25.	SEM micrograph of zirconia deposit made on nickel substrate at P = 5 Torr, T = 950 °C (22,000X).	119
26.	X-ray diffraction pattern of zirconia deposit made at a pressure of 5 Torr and a deposition temperature of 950 °C.	120
27.	Schematic diagram of sectioned sample with ZrO_2 deposit made at P = 5 Torr, T = 950°C	121
28.	SEM micrograph of cross section of leading edge of ZrO_2 deposit made at P = 5 Torr, T = 950 °C (2,000X).	121
29.	SEM micrograph of cross section of top surface of zirconia deposit made at P = 5 Torr, T = 950 °C (5,000X).	122
30.	SEM micrograph of cross section of trailing edge of zirconia deposit made at P = 5 Torr, T = 950 °C (3,000X).	122
31.	Cross section of top surface of zirconia deposit made at P = 5 Torr, T = 950 °C (12,000X).	123
32.	First EDS scan of SEM micrograph from Figure 31.	124

FIGURE		PAGE

33. Second EDS scan of SEM micrograph from Figure 31. 124

34. Third EDS scan of SEM micrograph from Figure 31. 125

35. Fourth EDS scan of SEM micrograph from Figure 31. 125

36. Fifth EDS scan of SEM micrograph from Figure 31. 126

37. Sixth EDS scan of SEM micrograph from Figure 31. 126

38. Seventh EDS scan of SEM micrograph from Figure 31. 127

39. Eighth EDS scan of SEM micrograph from Figure 31. 127

40. SEM micrograph and XRD pattern of ZrO_2 deposited at P = 5 Torr, T = 1100 °C (1,000X). 128

41. EDS scan of deposit made at P = 5 Torr, T = 1100 °C.. 129

42. Rate of ZrO_2 deposition vs. temperature at P = 45 Torr. 130

43. Non-Arrhenius behavior of deposition rate at P = 45 Torr. 130

44. SEM micrograph of zirconia deposit on nickel substrate made at P = 45 Torr, T = 950 °C (5,000X). 131

FIGURE		PAGE

45. SEM micrograph of zirconia deposit on nickel substrate made at P = 45 Torr, T = 950 °C and what appears to be a microcrack (5000X). 131

46. X-ray diffraction pattern of zirconia deposit made at a pressure of 45 Torr and a deposition temperature of 950 °C. 132

47. Schematic diagram of sectioned sample with ZrO_2 deposit made at P = 45 Torr, T = 950 °C. 133

48. SEM micrograph of cross section of leading edge of ZrO_2 deposit made at P = 45 Torr, T = 950 °C (2,000X). 133

49. SEM micrograph of cross section of top surface of zirconia deposit made at P = 45 Torr, T = 950 °C (1,050X). 134

50. SEM micrograph of cross section of trailing edge of zirconia deposit made at P = 45 Torr, T = 950 °C (2,000X). 134

51. SEM micrograph of cross section of top surface of zirconia deposit made at P = 5 Torr, T = 950 °C (1,000X). 135

52. First EDS scan of SEM micrograph from Figure 51. 136

53. Second EDS scan of SEM micrograph from Figure 51. 136

54. Third EDS scan of SEM micrograph from Figure 51. 137

55. Fourth EDS scan of SEM micrograph from Figure 51. 137

FIGURE		PAGE

56. Fifth EDS scan of SEM micrograph from Figure 51. 138

57. Sixth EDS scan of SEM micrograph from Figure 51. 138

58. Seventh EDS scan of SEM micrograph from Figure 51. 139

59. Eighth EDS scan of SEM micrograph from Figure 51. 139

60. SEM micrograph and XRD pattern of ZrO_2 deposited at P = 45 Torr, T = 1050 °C (2000X). 140

61. EDS scan of the deposit made at P = 45 Torr T = 1050 °C. 141

62. Effect of pressure on deposition rate of ZrO_2 at 2 cm from zirconium source. 142

63. SEM micrograph of typical zirconia deposit produced using $Zr(tmhd)_4$ as a precursor (400X). 142

64. Magnified area of deposit made at 750 °C using zirconium metalorganic as a precursor and area scanned using AES. 143

65. AES scan and atomic concentration of boxed off area which appears in Figure 64. 144

66. Deposit made at 750 °C using zirconium metalorganic precursor and areas scanned using AES (denoted 1 and 2). 145

67. Result of first AES scan from Figure 66. 146

68. Result of second AES scan from Figure 66. 147

FIGURE		PAGE

69.	AES scan conducted on deposit made using $Zr(tmhd)_4$ precursor at 1050 °C.	148
70.	AES scan conducted on deposit made using $Y(tmhd)_3$ as a precursor.	149
71.	XRD scan of deposit made using zirconium and yttrium metalorganics as precursors.	150
72.	EDS scan of deposit made using zirconium and yttrium precursors.	151
73.	SEM micrograph of deposit made using Zr and Y metalorganic precursors (1,000X).	152
74.	SEM micrograph of scratch made using tweezers on surface of deposit obtained using Zr and Y metalorganic precursors (1,000X).	152
75.	SEM micrograph (1,000X) and EDS scan of large clump formation in deposit formed using zirconium and yttrium metalorganic precursors.	153
76.	SEM micrograph of zirconia coating made using Reactor 4 (2,000X).	154
77.	SEM micrograph of zirconia coating made using Reactor 4 (5,000X).	154
78.	SEM micrograph (10,000X) and EDS scan of zirconia deposit made using Reactor 4.	155
79.	Schematic diagram of layered ZrO_2/Al_2O_3 coating.	156
80.	SEM micrograph of surface (Al_2O_3) of layered coating (40X).	156
81.	SEM micrograph (2,000X) and EDS scan of a nugget which appeared in Figure 80.	157

FIGURE		PAGE

82.	SEM micrograph (2,000X) and EDS scan of smooth area which appeared in Figure 80.	158
83.	XRD pattern of multi-layered coating with alumina on top surface.	159
84.	SEM micrograph (150X) and EDS scan of surface of multi-layered coating.	160
85.	SEM micrograph (4,000X) and EDS scan of coating surface from Figure 84.	161
86.	SEM micrograph (12,000X) and EDS scan of ghost-like image from Figure 84.	162
87.	SEM micrograph of sectioned, layered coating (3,000X).	163
88.	SEM micrograph of sectioned, layered coating (5,000X).	163
89.	SEM micrograph showing what is believed to be a discontinuous alumina layer (4,000X).	164
90.	SEM micrograph of layered coating filling substrate flaw (4,000X).	165
91.	SEM micrograph of layered coating filling substrate flaws (7,000X).	165
92.	SEM micrograph of multi-layered coating (7,000X) showing where the sample was examined using spot EDS scans, numbered 0-9.	166
93.	First EDS scan of sample from Figure 92 (number 0).	166
94.	Second EDS scan of sample from Figure 92 (number 1).	167

FIGURE		PAGE

95. Third EDS scan of sample from Figure 92 (number 2). 167

96. Fourth EDS scan of sample from Figure 92 (number 3). 168

97. Fifth EDS scan of sample from Figure 92 (number 4). 168

98. Sixth EDS scan of sample from Figure 92 (number 5). 169

99. Seventh EDS scan of sample from Figure 92 (number 6). 169

100. Eighth EDS scan of sample from Figure 92 (number 7). 170

101. Ninth EDS scan of sample from Figure 92 (number 8). 170

102. Tenth and final EDS scan of sample from Figure 92 (number 9). 171

CHAPTER 1

INTRODUCTION

Ceramic coatings play an increasingly important role in applications where high temperatures, corrosion, oxidation and wear come into play. Business Communications Company, Inc. (BCC) estimates that the ceramic coating market will be $587 million in 1995.[1] The Freedonia Group (Cleveland, Ohio) predicts the estimated growth for ceramic coatings in the United States at roughly 12% per year, reaching $1.3 billion by 1995, and $2.15 billion by the year 2000.[1] Kline & Company (Fairfield, New Jersey) estimates the world coatings market will be $3 billion in 1995 and increase to $4.3 billion by 2000.[1] In short, the business of producing ceramic coatings is growing at a rapid pace and more effective methods of producing these coatings are being sought continuously by industry.

One important application of ceramic coatings is thermal barrier coatings (TBC's). These coatings are viewed as a major breakthrough in the protection of metals. Thermal barrier coatings are extensively used in the production of turbine engines as a method of extending the life of the turbine blades as well as combustor liners and stator vanes. These coatings are currently used to reduce maintenance. It is hoped that future TBC's will improve engine performance through increased turbine efficiency, simplification of design and improved fuel economy.

Thermal barrier coatings were first developed in the 1960's by the aerospace industry. The coating which is favored at present is 8 wt% Y_2O_3- stabilized ZrO_2 (YSZ). The small addition of yttria helps overcome the problem presented by the polymorphism of zirconia. YSZ offers low thermal conductivity ($\approx 1.4\frac{W}{mK}$), high resistance to thermal degradation, high toughness and a thermal expansion coefficient ($\approx 10^{-5}K^{-1}$) which is reasonably close to the superalloys which are used as substrates.[2,3] Thermal barrier coatings typically fail as a result of oxidation of the bond coat which is an intermediate coat between the metallic substrate and the YSZ which provides oxidation resistance and improves adherence.[4]

State-of-the-art YSZ coatings are currently produced by electron beam physical vapor deposition (EBPVD). This process, however, is extremely costly. An EBPVD system which is capable of coating five blades per hour costs in excess of $10 million. In addition, since EBPVD is a line-of-sight-process, it requires that the turbine parts be manipulated mechanically while in high vacuum deposition chamber environments. This requires extensive use of process controls, instrumentation and robotics. The complicated nature of the equipment associated with this process has caused it to be plagued by mechanical failures as well as inconsistency in the coatings produced. A less costly, more reliable process for the production of YSZ thermal barrier coatings is highly desirable.

One method under consideration is the production of YSZ coatings via chemical vapor deposition (CVD).[5] The advantages of a CVD method of production lie in the uniformity of coatings which may be applied to a large number of parts with a single run at a reduced cost and with minimal system failures. In addition, admixtures of precursors can be varied to produce functionally graded materials (FGM's) which act as a bond coatings. Once the bond coat has been produced the precursors may be adjusted accordingly to produce the YSZ coating. This can all be performed in a single, computer-controlled reactor. Bond coats are currently produced via CVD in a step separate from the electron beam physical vapor deposition of YSZ. This further increases costs through the increased labor caused by changing from one reactor to another.

The major disadvantages of the CVD system are the amount of time required to produce coatings of adequate thickness and the general complexity of the deposition processes. Typical YSZ thermal barrier coatings have a uniform thickness of nearly 250 μm. The growth rate of YSZ by CVD range from approximately 1 to 20 μm per hour. High deposition rates, however, do not necessarily produce the desired microstructure or adherence characteristics. Some have suggested that the coatings may not need to be as thick as 250 μm. There is evidence to suggest that at high temperatures (normal operating range of turbine engines) thermal diffusion occurs primarily by radiation. As a result, thermal barrier characteristics may be enhanced by the introduction of photon

scattering sites such as platinum inclusions. These inclusions could be produced by adding the necessary reactants to the admixture of precursors and deposited via CVD. Some have theorized that alternating layers of YSZ and alumina may prove to be an effective thermal barrier. It is thought that these coatings may need to be no more than 30 μm thick. Rapp et al.[6] as well as Wang[7] have submitted proposals concerning these layered coatings and their possible advantages, however, no results have been published in this area to date. In addition to the problem of the deposition rate, the physiochemical nature of the YSZ-CVD process has yet to be thoroughly understood.[4, 9] This prevented a realistic assessment of this method as a manufacturing process.

The purpose of this work was the production of ZrO_2 based coatings using chemical vapor deposition (CVD). The coatings which were examined were pure ZrO_2, Y_2O_3-stabilized ZrO_2 and alternating layers of ZrO_2 and Al_2O_3. The selection of Zr precursors for the deposition of ZrO_2 was addressed by studying the chlorination of metallic Zr, the vaporization of $ZrCl_4$ and the vaporization of Zr based metalorganics. Major parameters such as temperature, pressure and reactant flow rates were varied in an attempt to determine the optimum conditions for the deposition of ZrO_2. The effects of these parameters on the microstructure of the ZrO_2 deposits were studied.

CHAPTER 2

LITERATURE SURVEY

Thermal barrier coatings have undergone numerous changes since their introduction in the 1960's. Initially, pack cementation was used to produce alumina coatings such as TBC's.[9] Prior to 8 wt% yttria-stabilized zirconia, 22 wt% magnesia was used to stabilize zirconia.[10] Substantial interest has led to rapid changes in TBC's. Rapid advances have led to increased research in the area of thermal barrier coatings. A short listing of companies which are currently conducting research concerning TBC's include Pratt & Whitney, General Electric, Rolls-Royce, Cummins and Caterpillar. The impact which this technology has had on industry is substantial. By 1975, Rolls-Royce 2B11 turbine engines had been run in excess of 8000 hours with little sign of degradation.[11]

Deposition of Zirconia:

Since these thermal barrier coatings consist of 92 wt% ZrO_2, the production of zirconia is very important. Adherent zirconia coatings must be produced before this project can move on towards the production of YSZ coatings. As a result, a substantial amount of time was spent looking into the deposition of zirconia via chemical vapor deposition.

The deposition of zirconia may be accomplished by first chlorinating metallic zirconium and then reacting it with an oxygen source at an elevated temperature. One method of representing the series of reactions used by Sipp et al.[12] to deposit zirconia on alumina substrates is as follows.

$$2H_2(g) + 2CO_2(g) \leftrightarrow 2H_2O(g) + 2CO(g) \tag{1}$$

$$ZrCl_4(g) + 2H_2O(g) \leftrightarrow ZrO_2(s) + 4HCl(g) \tag{2}$$

or, by combining equations (1) and (2):

$$ZrCl_4(g) + 2CO_2(g) + 2H_2(g) \rightarrow ZrO_2(s) + 2CO(g) + 4HCl(g) \tag{3}$$

with a Gibb's free energy of $-189.85\frac{kJ}{mole}$.[12]

Sipp et al.[12] varied chlorinator temperature between 350 and 650 °C and deposition temperature between 1200 and 1600 °C. The substrate was hung on a microbalance using a tungsten filament. In this manner, Sipp et al.[12] were able to measure the mass of the zirconia which was deposited on the substrate continuously with an accuracy of 2.5 μg.

Sipp et al.[12] determined that at low pressures (7.5 to 15 Torr) the variation of the growth rate with temperature showed an Arrhenius relationship with an apparent activation energy of $40\frac{kJ}{mole}$ for 950 °C < T < 1250 °C.

Additional work conducted by Sipp et al.[12] focused on the effect of the total flow rate (Q_t). The influence of Q_t on the rate of deposition depends on the geometry of the reactor so this information is not directly applicable to our work (which used different reactor geometries). It is important to note, however, that in the reactor used by Sipp et al.[12], an increase in Q_t caused an increase in the rate at which zirconia was deposited. These experiments were performed using constant total pressure and gas phase composition. As a result, Sipp et al.[12] assigned the variations of the deposition rate to hydrodynamic effects rather than to the effects of the chemical reaction.

The work of Brennfleck et al.[13] indicated that no ZrO_2 coating was obtained below 800 °C (total gas pressure 25-50 Torr, cold-wall reactor). As the temperature increased, the rate of deposition increased exponentially to a maximum of 20 μm/hr at 950 °C. At temperatures above 950 °C the deposition rate decreased due to the formation of "dust". This dust formation occurred mainly at high oxygen partial pressures. Duret and Pichoir[14] (refer to Figure 1)[†] provided a simple schematic diagram which aids in determining what type of deposit will occur given certain conditions. As the temperature is increased, the microstructure of the deposit goes from a gas phase nucleated powder to more crystalline structures. Increasing the supersaturation of the reactants causes the microstructure to change from a crystalline deposit to a gas phase nucleated powder.

---

† All figures referenced in this text appear in the Appendix.

Brennfleck et al.[13] described large fluctuations in the structure of the coatings depending on reactor arrangement as well as deposition temperatures. Using a cold-wall reactor (only the substrate is heated) coarse-grained layers up to 100 μm thickness were deposited at 1000 °C. Using a hot-wall reactor at low temperatures (650 °C) resulted in fine-grained coatings which were poorly adherent when the thickness exceeded 10 μm. As a result, Brennfleck et al.[13] recommended the use of a cold wall reactor for the deposition of zirconia.

The ZrO_2 deposit produced by Brennfleck et al.[13] which had high density did not exhibit a columnar structure. The preferred microstructure for YSZ thermal barrier coatings is columnar (several μm in diameter) and oriented roughly perpendicular to the surface of the coated part [(100) and/or (111) directions].[3,5] It is speculated that this orientation allows physical separation of the individual columns during thermal cycling (Figure 2).[3] This ability to separate relieves the tensile stress between the component surface and the coating which occurs during thermal cycling.[3] This, in turn, reduces spallation and extends the life of the coating and hence the life of the turbine part.[3] It should be noted that this columnar structure has yet to be produced by any method which is economically acceptable for commercial production other than electron beam physical vapor deposition.

Another method for depositing zirconia involves the use of metalorganics.[5, 15-18] Metalorganics are essentially metallic elements with organic ligands attached. Desu et

al.[15] conducted research into which organometallic was most suitable for the deposition of zirconia. The most effective zirconium metalorganic appeared to be zirconium tetramethylheptadionate or $Zr(thd)_4$ (also $Zr(tmhd)_4$ or zirconium 2,2,6,6-tetramethyl-3,5-heptadionate). Organometallic alkoxides, such as zirconium i-propoxide $[Zr(OPr^i)_4]$ and zirconium t-butoxide $[Zr(OBu^t)_4]$ were not suitable precursors due to their instabilities. Desu et al.[15] as well as Hwang et al.[16] reported that high-quality zirconia films were deposited using zirconium trifluoroacetyl-acetonate $[Zr(C_5H_4F_3O_2)_4]$. However, fluorine contamination presented possible problems. The work of Desu et al.[15] with $ZrCl_4$ yielded results similar to those obtained by Brennfleck et al.[13]

Si et al.[17, 18] used $Zr(tmhd)_4$ to deposit high-quality zirconia films at low pressures (4-10 Torr). Deposits were formed at temperatures as low as 530 °C, though deposition rates were low. Brennfleck et al.[13] witnessed no deposition below 800 °C with $ZrCl_4$ as a precursor. Vapor pressures of $Zr(tmhd)_4$, as calculated by Si et al.[17, 18] using isothermal gravimetric (TGA) experiments, ranged from 1-100 mTorr. As a result, precursor temperatures were held between 230 and 240°C. Deposition rates of 0.36 to 1.08 μm/hr were observed with a deposition temperature of 550 °C (total pressure was varied between 4 to 10 Torr).

Deposition of Yttria:

Having examined work with deposition of zirconia via CVD, it is now required that some understanding of the deposition of yttria via CVD be developed. Sipp et al.[19] deposited yttria on alumina supports using reactions which may be represented as follows:

$$3H_2(g) + 3CO_2(g) \leftrightarrow 3H_2O(g) + 3CO(g) \tag{4}$$

$$2YCl_3(g) + 3H_2O(g) \leftrightarrow Y_2O_3(s) + 6HCl(g) \tag{5}$$

or by combining equations (4) and (5):

$$2YCl_3(g) + 3H_2(g) + 3CO_2(g) \rightarrow Y_2O_3(s) + 3CO(g) + 6HCl(g) \tag{6}$$

Note the similarities between the reactions for the deposition of zirconia using metal chlorides [equations (1), (2) and (3)].

Sipp et al.[19] determined that at a pressure of P = 30 Torr, T < 1100 °C and a total flow rate of $500 < Q_{tot} < 1000 \frac{cm^3}{\text{min}}$, the process was rate-controlled by surface reactions with an apparent activation energy of $616 \frac{kJ}{mole}$. Mass transfer across the boundary layer became the rate-limiting phenomena beyond these limits.

The coatings produced by Sipp et al.[19] contained yttrium oxychlorides (YOCl) with trace amounts of Y_2O_3. Yttria alone was deposited when the amount of CO_2 was

increased. According to the authors, solid YOCl was produced when the amount of CO_2 was insufficient. The Y_2O_3 deposits (obtained at T = 1090 °C, P = 30 Torr) were "well faceted and irregular platelet-like crystals"[19] with an average size of 10 μm.

Like zirconia, yttria may also be deposited using an organometallic. Dismukes et al.[20] were awarded a patent concerning the deposition of luminescent films in July, 1975. In this patent, the authors described deposits resulting from metal beta-diketonates of the form $M(tmhd)_3$ where the metal M is either yttrium (Y), lanthanum (La), gadolinium (Gd) or lutetium (Lu).

Varhue et al.[21] deposited Y_2O_3 on silicon substrates using plasma-enhanced chemical vapor deposition (PECVD). The organometallic used was yttrium tetramethylheptadionate [$Y(tmhd)_3$]. Yttria deposits were made at temperatures as low as 350 °C (substantially lower than the deposition temperatures used by Sipp et al.[19] to deposit yttria from YCl_3). Varhue et al.[21] determined that the deposition rate increased from 0.069 to 0.12 μm/hr as the reactor pressure was raised from 1.5 to 5.0 Torr. In addition, the authors determined that the deposition rate increased linearly with the substrate temperature. They attributed this trend to enhanced thermal decomposition of the organometallic precursor. Examination of the deposits using high-energy electron diffraction revealed coatings which were highly oriented, but textured. The films were polycrystalline with the grains aligned about an axis parallel to the surface of the substrate. While PECVD will not be used in this project, the work conducted by Varhue

et al.[21] reveals vital information concerning the deposition parameters which will be used to guide CVD reactor parameters in the deposition of yttria.

Deposition of Yttria-Stabilized Zirconia via Electrochemical Vapor Deposition:

In order to facilitate the production of yttria-stabilized zirconia, other methods of producing these coatings have been reviewed. One method of deposition which has been extensively studied is that of electrochemical vapor deposition (EVD). Schoonman et al.[22] attribute the development of this process to Arnold Isenberg of the Westinghouse R&D center in Pittsburgh, Pennsylvania. EVD is a modification of CVD which relies on the ionic and electronic conductivity of stabilized zirconia to produce gas-tight films of uniform thickness. Westinghouse uses the method to deposit two types of commercially important dense oxide films for solid oxide fuel cell applications; namely, yttria-stabilized zirconia electrolyte films and magnesium-doped lanthanum chromate interconnection films. These adherent coatings are gas-tight thin films in order to reduce the ohmic resistance of the cell.

Electrochemical vapor deposition is an important technology for making thin layers of YSZ for solid oxide fuel cells (SOFC's). SOFC's use hydrogen or hydrocarbon fuels and oxygen to generate direct-current electric power. SOFC's operate at extremely high fuel efficiency and are not Carnot limited.[22] These fuel cells convert the free energy of a chemical reaction directly to electrical energy and hence high fuel efficiency and

potentially very large power density ($\frac{W}{kg}$) are possible. Operating temperatures for SOFC's range from 900 to 1000 °C and this places stringent demands upon the materials used to construct these components. YSZ, with its relatively low cost, chemical inertness and high ionic conductivity, is a material which has been extensively studied for use in the construction of SOFC's.

Schoonman et al.[22] as well as Pal[23] described EVD as a process in which the solid-state transport through the film contributes to the film growth. A schematic of this process appears in Figure 3. The process involves passing halides of the cations over one side of a porous substrate. The halides chosen have a relatively high vapor pressure. Oxygen and/or steam is passed on the other side of the substrate. The deposition takes place in two stages. At first, the oxygen, steam and metal halides diffuse through the pores of the substrate. The metal halides oxidize and fill the pores with oxide. This portion of the reaction is identical to CVD. Once the pores have become filled a gradient in oxygen potential exists across the deposited oxide in the pores (between the halide side and oxygen side). This causes solid-state electrochemical transport of the ionic and electronic species. As a result, the oxide remains electrically neutral. The ions react with the gas phase and the oxide continues to grow as a film over the porous substrate.

Pal et al.[24] made deposits of 10 wt% yttria-stabilized zirconia via EVD using halide precursors. The reactor's pressure was held at 0.125 Torr and the chlorides were

vaporized in a predetermined ratio. $ZrCl_4$ and YCl_3 were passed over the outer surface of a porous tubular substrate along with argon and hydrogen. Oxygen and steam were passed inside the porous tubular substrate. During the CVD portion of the reaction (Stage 1 in Figure 3) molecular diffusion of oxygen, steam, metal chlorides and hydrogen occurred through the porous substrate and reacted, filling the pores with YSZ. Once the pores were filled, deposition of YSZ continued to occur via electrochemical vapor deposition (Stage 2 in Figure 3). Pal et al.[24] determined that the growth of YSZ occurred on the side of the substrate that was exposed to the halides of the cations. This indicated that the mobility of oxygen ions was much greater than that of the cations (Zr and Y). If the zirconium and yttrium cations had been more mobile than the oxygen ions, the YSZ coating would have grown inside the tubular porous substrate (oxygen and steam side).

The growth rate of YSZ via EVD is parabolic with time.[23-26] Dekker et al.[25] conducted work aimed at discovering the rate-limiting step in the EVD of YSZ system. Having derived an equation originating from the Wagner oxidation theory[23-25], Dekker et al.[25] fitted all of their reported values of film thickness versus deposition time to the following equation:

$$L^2 = 2Kt + C_0 \tag{7}$$

where K is the parabolic rate constant, L is the film thickness, t is the total deposition time and C_0 is a constant of integration.

Carolan and Michaels[26] assumed that the integration constant in equation (7) was zero and arrived at the following equation:

$$L = \sqrt{Kt} \tag{8}$$

where the variables have the same values as in equation (7). While equation (7) and (8) are similar in form, they are not exactly the same. None the less, they agree that the rate-limiting step in EVD is solid state diffusion.

Deposition of Yttria-stabilized Zirconia via Plasma Spray:

Another method which has been used to produce YSZ coatings is plasma spraying. This process involves injecting a powder of the material which is to be deposited into a plasma jet which melts the particles and blows them at a high velocity onto the substrate to be coated. The molten particles spread evenly and solidify to produce a coating made up of large numbers of rapidly solidified lamellae.[27] This process differs greatly from the others in that there is no precursor which needs to be reacted. If zirconia is to be deposited, it must be heated to its melting point (2700 °C).

In the deposition of YSZ, both zirconia and yttria powders or YSZ must be melted and sprayed onto the substrate surface. According to McPherson and

Houghton[27], as well as Suhr et al.[28], the ZrO_2 and Y_2O_3 particles struck the cold substrate and solidified, forming the high-temperature cubic phase. Since cooling rates for plasma spray are extremely fast, the majority of the cubic phase transformed directly into the metastable tetragonal phase of the same composition (displacive transformation). Suhr et al.[28] observed that the tetragonal phase was maintained at room temperature even though it was not at equilibrium. This form is not stable at high temperatures and transforms into a mixture of cubic and low Y_2O_3 content. It may undergo further transformation to form a monoclinic phase upon cooling to room temperature. The monoclinic transformation involves a large volume change which may cause the coating to fail due to delamination and spallation.

Suhr et al.[28] subjected plasma-sprayed YSZ coatings of various yttria content to cyclical as well as static heating. Cyclical thermal exposure tests consisted of heating the specimens to 1000 °C for 50 minutes followed by forced-air-cooling for 10 minutes. This step was repeated for 500 cycles or until cracks were observed to form in the ceramic coating. The static heating involved heating specimens to 1200 °C for 1, 10, and then 100 hours. They determined that a low Y_2O_3 content resulted in failure due to the presence of the monoclinic phase (poor thermal and mechanical stability). Coatings containing high amounts of yttria (Y_2O_3) failed due to the fact that the zirconia became fully stabilized. Fully stabilized zirconia has fracture toughness that is inferior to that of partially stabilized zirconia. In addition, Suhr et al.[28] determined that optimum toughness

was achieved at 6-8 wt% Y_2O_3. This was a result of the good mechanical properties of the metastable tetragonal phase and its slow conversion to a metastable mixture of cubic and tetragonal phases. These coatings would last until the bond coating no longer resisted oxidation by the formation of an adherent alumina scale.

Bratton et al.[29] conducted work similar to that performed by Suhr et al.[28], but in a more comprehensive manner. They performed burner rig tests on plasma sprayed YSZ coatings. In addition, the fuel used was either pure or contained impurities to simulate water-washed residual fuels.

The clean fuel tests were conducted using GT No. 2 fuel (ASTM 2880-76). While the gas temperature was held constant at 1150 °C, the metal substrates were heated to one of three temperatures (800, 850, or 900 °C). The specimens were subjected to 500 cycles with each cycle being 1 hour in duration. The results of this test showed that 8 wt% yttria stabilized zirconia performed the best.

Next, Bratton et al.[29] tested the coatings for fuel sensitivity. Two cases were studied. In the first instance, GT No. 2 fuel doped to 1 ppm Na, 2 ppm V, 2 ppm P, 0.5 ppm Ca, 2 ppm Fe and 6 ppm Mg. This mixture represented a water-washed crude oil. The second case consisted of GT No. 2 fuel doped to 1 ppm Na, 50 ppm V, 2 ppm P, 0.5 ppm Ca, 2 ppm Fe, and 150 ppm Mg. This mixture represented a water-washed residual oil. Both mixtures had a magnesium to vanadium ratio of 3, as per commercial practice, and a sulfur content of 0.25%. Tests consisted of 500, 1 hour long cycles at

1150 °C. These tests revealed that the 50 ppm vanadium fuel caused accelerated failures as compared to the 2 ppm vanadium fuel. However, the role of vanadium and its salts in the failure mechanism was unclear. Moreover, in the more severe test of 1 ppm sodium coupled with 50 ppm vanadium, the 8 wt% YSZ outperformed the other TBC's.

Plasma spray will not be used in this work, but the work done by others with regard to the behavior of electrochemical vapor deposition and plasma spray provide important information as to the failure modes of YSZ. By studying their work, pitfalls may be avoided and time saved in the production of YSZ via CVD.

Deposition of Yttria-stabilized Zirconia via Chemical Vapor Deposition:

As mentioned earlier, CVD of YSZ is a critical step in EVD. As a result, Carolan and Michaels.[30] looked into the role CVD plays in the manufacture of SOFC's. They deemed such a study as necessary since the CVD phase of EVD can determine the processing time and electrochemical properties of the finished electrolyte film. Using a porous substrate (such as would be used in EVD) Carolan and Michaels[30] examined the CVD stage of the EVD process. If the CVD process works ideally then the deposition of YSZ will occur on the metal chloride side of the substrate. A non-ideal CVD process, on the other hand, might plug pores deep within the substrate. Once the pore is plugged the deposition would occur via EVD on the metal chloride face. The film produced by the non-ideal case of CVD would be much thicker than that produced in the event of an

ideal CVD case. Figure 4 shows a comparison between the effects of ideal and non-ideal deposition of YSZ in the EVD process. The processing time of the non-ideal case would be longer and the ohmic resistance greater. In the non-ideal case, the zirconia is not deposited in a compact fashion. It deposits in a manner which narrows the pore significantly and this hinders the mass transport to an electrode which is deposited on the substrate side of the electrolyte. The non-ideal case causes a reduction in the efficiency of the electrochemical device. In addition, the composition of coatings formed from non-ideal deposition may differ from that deposited by the EVD process. As a result, the CVD phase of the EVD process is critical in forming good coatings which behave in a predictable fashion. Understanding how to control the morphology and composition of the electrolyte deposited during the CVD phase is of great importance.

Carolan and Michaels[30] deposited YSZ films on porous alumina substrates in an effort to determine the typical penetration depths and film growth times. Metal chlorides (YCl_3 and $ZrCl_4$) were used as precursors. The zirconium tetrachloride was heated to 160 °C while the yttrium trichloride was heated to 611 °C. These temperatures were chosen to obtain sufficient vapor pressure. The total gas pressure inside the reactor was 1.1 Torr and the deposition temperature was 1100 °C. The atmosphere consisted of an equimolar mixture of hydrogen and water. The water concentration (c_w^0) was varied in order to determine its effect on film morphology (either $c_w^0 = 8.6 \times 10^{-10} \frac{moles}{cm^3}$ or $c_m^0 = 1.3 \times 10^{-9} \frac{moles}{cm^3}$, i.e. $\frac{c_m^0}{c_w^0} = 1.5$ where c_m^0 is the concentration of the metal chlorides).

The film, grown on a substrate with 30 μm pores, did not penetrate the substrate more than 60 μm (twice the pore diameter). In order to determine the closure rate of the pore, the flow of hydrogen and water was interrupted at regular intervals. This effectively ceased the reaction. While still in the reactor, the gas permeability was measured. This provided insight into when the pores had become plugged. Carolan and Michaels[30] determined that the pores became plugged within 10 to 30 minutes. This rate was insensitive to the water to metal chloride ratio as well as the metal chloride flow rate.

Carolan and Michaels[30] determined that pore closure always occurred at the metal chloride face as a direct result of the kinetics of the reaction. In addition, the time for pore closure and the final pore radius are described by a single Thiele modulus (ratio of reaction velocity to diffusion velocity) which appears in equation 9. Furthermore, a higher Thiele modulus resulted in shorter run times. In addition, a high Thiele modulus produced films via CVD which neither penetrated nor narrowed the pores significantly.

$$\Phi_m = \frac{2L^2K}{D_m a} \qquad (9)$$

Φ_m = Thiele modulus
D_m = Diffusivity of metal chloride
a = Rate of change of pore radius
K = Rate constant
L = Distance over which diffusion occurs (total pore length in this instance)

It is interesting to note that Yeckel and Middleman[31] observed a similar relationship in depositing silicon dioxide films on wafers at low pressures.

Yamane and Hirai[32] also deposited YSZ films using metal chloride precursors. Using flat quartz substrates, YSZ coatings were prepared by CVD in a reactor which is similar to the one which will be employed during this study. The vaporized YCl_3 (900-1000 °C) and $ZrCl_4$ (280-310 °C) were transported to the substrate using argon flowing at 170 standard cubic centimeters per second (sccm) as a carrier gas. The transport rates depended on the vaporization temperature of the chlorides.

At a deposition temperature of 1100 °C, cubic YSZ was deposited with the weight percent (x) of YCl_3 being between 20 to 60% (equation 10).

$$x = \frac{YCl_3}{(YCl_3 + ZrCl_4)} \times 100 \qquad (10)$$

Films produced by Yamane and Hirai[32] with $x < 20\%$ consisted of monoclinic and cubic and/or tetragonal phases whose (100) planes were parallel to the surface of the substrate. With x = 20-45%, the films produced were colorless and transparent. X-ray diffraction (XRD) revealed the orientation of a (100) plane that was parallel to the surface of the substrate. As x was increased to 45-60%, the degree of orientation at the (100) plane diminished. The coatings produced at these higher values of x were colorless and translucent. The translucent appearance was thought to be a result of scattering at the

grain boundary which was oriented in different directions. At substrate temperatures between 1100 and 1200 °C, the deposit was cubic with a (111) orientation plane parallel to the surface of the substrate. By varying the amount of yttrium trichloride in the gas phase, Yamane and Hirai[32] determined that it was less incorporable into the film than the zirconium.

Electron micrographs showed that the (111) oriented YSZ exhibited a columnar structure.[32] No voids were present in either the (100) or (111) depositions, however, several transgranular cracks were present. These cracks were caused by differing thermal expansion values between the coatings and the substrate and the tension which resulted upon cooling. Since these cracks were destroying the internal structure of the granules, it suggested the existence of a tight bond between each grain in the film.[32]

Kim et al.[33] used plasma-enhanced chemical vapor deposition to deposit YSZ from organometallic precursors, namely $Y(tmhd)_3$ and $Zr(tmhd)_4$. Plasma enhanced chemical vapor deposition is very similar to the normal chemical vapor deposition process. Separate vaporizers were used to heat the organometallics in order to obtain a sufficient vapor pressure. A carrier gas, such as argon, was then used to transport the vapor to the reaction chamber. The main difference was that a plasma is generated within the reaction chamber by use of electrodes in order to enhance the deposition process.[33]

Using an oxygen flow rate of 40 $\frac{cm^3}{min}$ and argon flow rate of 130 $\frac{cm^3}{min}$ (pressure was set at 80 Pa or 0.600 Torr) Kim et al.[33] deposited YSZ on (100) silicon. They varied the Y_2O_3 content in the YSZ films by varying the temperature to which the $Y(tmhd)_3$ was heated. Kim et al.[33] determined that for vaporization temperatures above 150 °C with a deposition temperature of 405 °C, the coatings produced were fully stabilized zirconia (normally single phase cubic) which tended to grow with a (100) orientation.

Aleksandrov et al.[34,35] proposed a model for the calculation of the cubic lattice constants of ZrO_2. They assumed spherical packing of ions and calculated the average number of anion vacancies per unit cell. Their results appear in equation 11.

$$d = A\left[R_{Zr} + R_O + \frac{\Sigma_{k=1}^{n}(P_k m_k \Delta R_k)}{100 + \Sigma_{k=1}^{n} m_k(P_k - 1)}\right] \qquad (11)$$

R_{Zr} = Ionic radius of Zr^{4+} (0.81 Å).
R_O = Ionic radius of O^{2-} (1.40 Å).
R_Y = Ionic radius of Y^{+3} (0.90 Å)
ΔR_k = Difference between the ionic radii of the kth stabilizing element and zirconium (R_Y-R_{Zr}).
m_k = Mole percentage of kth stabilizer.
P_k = Number of ions per unit cell of each stabilizeing element of the oxide.
A = Constant based on geometry of fluorite structure unit cell (2.3094).

For YSZ, which is a binary system where $n = 1$ and $P = 2$, equation 11 reduces to equation 12.

$$d = 2.31R_{Zr} + R_O + \left(\frac{2m\Delta R}{100 + m}\right) \tag{12}$$

The equations derived by Aleksandrov et al.[34, 35] were used by Ingel and Lewis[36] to compare calculated and experimentally measured values of lattice parameters and densities for Y_2O_3-stabilized ZrO_2 single crystals. These samples had been prepared by a commercial manufacturer using a cold crucible directional solidification process known as skull melting. Concentrating on compositions with ≥ 8 mol% (≈ 14 wt%) they determined that the model devised by Aleksandrov et al.[34, 35] accurately predicted these values over a wide range of composition. Being able to predict these values allows for refinement of processing techniques.

The findings of Ingel and Lewis[36] indicate that crystals or pure ZrO_2 were monoclinic containing many twins. As Y_2O_3 content increased to 2.8 mol% (5 wt%) the ZrO_2 became less monoclinic, containing more cubic and/or tetragonal phases. Crystals with from 2.5 - 7 mol% (5 - 12 wt%) Y_2O_3 content contained decreasing amounts of the second-phase tetragonal ZrO_2 becoming cubic from 8.5 - 20 mol% (15 - 20 wt%) Y_2O_3 content.

Akiyama et al.[37] fabricated YSZ coatings using low-pressure metalorganic chemical vapor deposition (LPMOCVD). This method will be used in this research for the deposition of YSZ coatings on nickel and nickel alloy substrates. The

organometallics used were $Zr(tmhd)_4$ (heated to 160 °C) and $Y(tmhd)_3$ (heated to 110 ~ 120 °C). The substrate used was many short quartz tubes so that the local growth rate distribution along the flow of direction could be determined. Using a reactor similar to the reactor which will be used for this work, Akiyama et al.[37] deposited columnar, 8 wt% yttria-stabilized zirconia that was characterized by a columnar structure at a deposition temperature of 750°C. At a deposition temperature of 500°C, the deposit consisted of fine grains.

Akiyama et al.[37] modeled the CVD mechanism of YSZ as follows. The organometallics undergo a first-order gas-phase reaction to produce the gaseous precursors. These then diffuse to the surface of the substrate where an oxide film is deposited by first-order surface reactions.

Source materials	$\xrightarrow{r_g = k_g C_m}$	Precursors transport in the gas phase	(13)
Precursors transport in the gas phase	$\xrightarrow{r_s = k_s C_p}$	film	(14)

where r_g and k_g are the reaction rate constants of the homogeneous reaction while r_s and k_s are the reaction rate constants of the heterogeneous reaction. C_m and C_p are the concentrations of the source material (organometallics) and precursors, respectively.

Using a simple Monte Carlo simulation, Akiyama et al.[37] arrived at the following values $\left(R\left[\frac{J}{mole \bullet K}\right]\right)$:

For ZrO_2 growth:

$$k_g = 6.8 \times 10^{11} \exp\left(\frac{-140000}{RT}\right) \tag{15}$$

$$k_s = 1.3 \times 10^{12} \exp\left(\frac{-188000}{RT}\right) \quad \text{for T< 908 °K (635 °C)} \tag{16}$$

$$k_s = 3.1 \times 10^{3} \exp\left(\frac{-38000}{RT}\right) \quad \text{for T} \geq \text{908 °K (635 °C)} \tag{17}$$

For Y_2O_3 growth:

$$k_g = 7.9 \times 10^{10} \exp\left(\frac{-123000}{RT}\right) \tag{18}$$

$$k_s = 3.4 \times 10^{9} \exp\left(\frac{-134000}{RT}\right) \tag{19}$$

The values of r_g and r_s can be calculated using the values of k_g and k_s (refer to equations 13 and 14). The temperature dependencies of the reaction rate constants as determined by Akiyama et al.[37] using equations (15) - (19) appear in Figure 5.

Growth rates of YSZ via CVD varied along the flow direction. Akiyama et al.[37] held the feed ratio (*FR*) constant at 15 at% (equation 19) but varied the deposition temperature. The results obtained by Akiyama et al.[37] appear in Figures 6 and 7.

$$FR \equiv \frac{Y}{(Y+Zr)} \tag{20}$$

The width of the histograms is equal to the length of the quartz tube substrates and represents the experimental results that were observed. The dashed and dotted lines represent the deposition rate as calculated by Akiyama et al.[37] The dashed line represents the deposition rate of ZrO_2 and the dotted line represents the deposition rate of Y_2O_3. The calculated deposition rates are based on the reaction rate constants from equations (15) - (19) as well as the feed ratio of each component. The solid line is a result of the linear combination of the dashed and dotted lines and coincides with the experimental growth rate distribution as observed by Akiyama et al.[37] Figure 7 shows the growth rate of YSZ as well as the yttria composition of the film, $\frac{Y}{(Y+Zr)}$ (refer to equation 20), along the flow direction under various conditions. Additivity of each component was assumed and used to calculate the results (solid lines). These closely matched the experimental composition distributions (plots) but deviated near the entrance and exit. The reaction rate of each component was so high at 700 °C that the growth rate was limited by mass transfer rates. As a result, the film composition closely resembled the gas composition. At lower temperatures (500 °C) the growth rate was controlled by the

gas-phase and surface reaction rates. This caused the less stable Y to deposit faster than Zr, thus the film gradually became richer in Y than the feed gas and the Y composition decreased along the flow direction due to depletion of reactants.

Pulver et al.[38] also deposited YSZ via CVD using (tmhd)-organometallics. They examined the evaporation and deposition processes and correlated them with fluid-dynamical calculations. They determined that at temperatures below 610 °C the deposition of YSZ was kinetically controlled by the thermal decomposition of the molecules on the surface of the heated substrate. An activation energy of $E_A = 51.2\frac{kJ}{mole}$ was derived from the temperature dependency. Once the temperature exceeded 610 °C the deposition rate of YSZ became independent of the deposition temperature. In addition, they observed that the rate was limited by the mass transport of reactants to the surface of the substrate. The maximum deposition rate obtained was approximately 1 μm/hour. Pulver et al.[38] claim that this relatively slow rate of deposition was due to the low concentration of precursors in the gas phase (molar fraction $\approx 10^{-4}$).

Pulver et al.[38] determined that the ratio of the deposition rates of yttria to zirconia was proportional to the ratio of the evaporation rates of the precursors [$Zr(tmhd)_4$ to $Y(tmhd)_3$]. They also observed that the composition of the deposited YSZ layer was temperature-dependent at temperatures below 600 °C as a result of the differences in temperature dependence of the deposition of yttria and zirconia.

Pulver et al.[38] used a computer program (FLUENT, version 3.03, creare.x inc., 1991) to model the evaporation behavior and the deposition in their stagnation flow reactor. The program used a finite difference numerical procedure to solve the basic equations which govern flow, namely the Navier-Stokes equations. The diffusion coefficients were calculated using FLUENT coupled with the kinetic theory according to equation 21.[38, 39]

$$D_{ij} = 0.002628 \times \frac{\sqrt{T^3 \frac{(M_i + M_j)}{2M_iM_j}}}{p\sigma_{ij}^2 \Omega_{ij}^{(1.1)*\frac{\varepsilon_{ij}}{k}}} \qquad (21)$$

D_{ij} =Diffusion coefficient $\left[\frac{cm^2}{s}\right]$
p = Total pressure in atmospheres
T = Temperature in K
M_i, M_j = Molar masses $\left[\frac{g}{mole}\right]$
σ_{ij}= Lennard Jones Length [Å] = 10.7 Å
$\frac{\varepsilon_{ij}}{k}$ = Lennard Jones energy = 600 K
Ω_{ij} = Reduced collision integrals

In order to perform these calculations, Pulver et al.[38] had to make the assumption that the equilibrium pressure p_0 existed immediately above the surface of the precursor. The resulting values were within ± 20% of actual values, which Pulver et al.[38] considered to be reasonable assuming the above assumption.

In addition, Pulver et al.[38] compared their results of the vapor pressure of $Zr(tmhd)_4$ with the values obtained by Iikawa et al.[40] Iikawa et al.[40] used the Clausius-Clapeyron equation to arrive at the following equation for the vapor pressure of $Zr(tmhd)_4$:

$$\log P[\text{Torr}] = \frac{-3687}{T[\text{K}]} + 7.659 \qquad (22)$$

P = Pressure
T = Temperature

Pulver et al.[38] obtained significantly lower equilibrium vapor pressures than did Iikawa et al.[40] Pulver et al.[38] attributed this to possible variations in the quality of the organometallics tested.

The final conclusion of Pulver et al.[38] was that fluid dynamic calculations are suitable for the modeling of the flow phenomena in CVD processes and for the evaporation of the precursors as well as for the deposition of films. The concentration of the precursor in the gas reached a maximum when the equilibrium vapor pressure was reached. This required that the evaporation conditions be maximized. Based on this information, Pulver et al [38] arrived at the following conclusions:

1) The diffusion boundary must be minimized in order to maximize the evaporation rate.

2) In order to provide a constant evaporation rate the

surface and level of the organometallic in the vaporizer must be held constant.

Pulver et al.[38] went on to make recommendations as to how to fulfill these demands. They suggested a powder transport system so that the vaporizer might be continuously supplied with the organometallic precursors. Another solution was to minimize the total gas flow so that the carrier gas becomes saturated.

Thermal Diffusivity and Conductivity

of Yttria-Stabilized Zirconia:

While extensive research has been conducted concerning the deposition of YSZ via CVD, it must be kept in mind that the end product is a thermal barrier coating. As a result, the thermal diffusivity as well as the thermal conductivity of any coating produced must be examined. Figure 8 shows a schematic diagram of the temperature profile through a thermal barrier. The hot environment is to the right in Figure 8. As the thermal barrier coating (TBC) is approached there is a drop off in temperature. The drop off continues through the TBC and bond coat, all though the gradient lessens as it progresses from one layer to the next. The temperature is relatively constant through the metal substrate and then drops off sharply once the cooling air is reached (modern turbine blades are hollow and have cooling air circulating within them).

Morrell and Taylor[41] as well as Youngblood et al.[42] have conducted thermal diffusivity tests on partially and fully stabilized single crystals of YSZ using laser flash methods. This technique involves subjecting one side of the sample to a short pulse of radiant energy and recording the temperature history (dimensionless) of the other side. Morrell and Taylor.[41] exposed the substrate side of the sample to a radiant pulse from a neodymium-glass laser which had a dissipation time of $6 \times 10^{-4} s$. The radiation from the ceramic side of the specimen was collected and focused onto an infrared detector. The dimensionless temperature rise $V(t)$ was calculated by Morrell and Taylor [41] using the analysis proposed by Bulmer and Taylor[43].

$$V(t) = 1 - 2\gamma_2 \Sigma_{K=1}^{\infty} \frac{\left[1 - \exp\left(\beta_K^2/\gamma_2\right)\right]\exp\left(-\beta_K^2 t/U_2\right)}{\beta_K^2 \cos(\beta_K X)\cos\beta_K - \Omega(X)\sin\left(\beta_K^2 X\right)\sin\beta_K} \qquad t > \tau_p \quad (23)$$

where β_K is the positive root of:

$$H\sin(\beta X)\cos\beta + X\cos(\beta X) = 0$$

and

$$X = \left(\frac{l_1}{l_2}\right)\left(\sqrt{\frac{\alpha_2}{\alpha_1}}\right) \qquad \gamma_2 = \frac{l_2^2}{\alpha_2 \tau_p} \qquad U_2 = v_2 \tau_p$$

$$H = (\rho_1 C_1 l_1)(\rho_2 C_2 l_2)^{-1} \qquad \Omega(X) = [X + (H/X)](H-1)^{-1}$$

where subscripts 1 and 2 refer to the front (substrate) and rear (ceramic) layers and:

α = Thermal diffusivity
C = Specific heat
ρ = Density
l = Thickness of the layer
τ_p = Heat pulse duration that can be approximated by
$F(t) = 1 - H(t - \tau_p)$

with H being equal to the Heaviside step function and is defined as:

$$H(t - \tau_p) = 0 \text{ for } 0 < t < \tau_p$$
$$H(t - \tau_p) = 1 \text{ for } t > \tau_p$$

The values of α, C, ρ and l must be known for one layer and provided C, ρ and l are known for the unknown layer, then the value of the thermal diffusivity can be calculated for that layer.

Morrell and Taylor[41] chose to treat the bond coat as part of the substrate. This was a reasonable assumption since the bond coat was only ~1% the thickness of the substrate. As a result of this assumption a two-layer analysis was performed as opposed to a three-layer analysis.

Testing partially stabilized zirconia with 6, 8, 10 and 12 wt% yttria contents, Morrell and Taylor[41] as well as Brandon et al.[44] prepared the coatings using plasma spraying. Coatings produced from spherical particles had thermal diffusivities that were 30-45% higher than those produced using angular particles. In addition, it was

determined that diffusivity values displayed no correlation with composition. The order of thermal diffusivity values for different amounts of yttria as determined by Morrell and Taylor[41], from lowest to highest, were 12, 8 and 10 wt% yttria for both coatings, with those produced from the angular particles being lower than those produced from the spherical particles. The 6 wt% yttria-stabilized zirconia produced irregular results. The work of Brandon et al.[44] showed that the ranking of thermal diffusivity values for different amounts of yttria, from lowest to highest, were 12, 10, 6 and 8 wt% yttria. For all wt%'s of yttria-stabilized zirconia, the thermal diffusivity exhibited a minimal change if any with increasing temperature.

Morrell and Taylor[41] determined that the difference in the thermal diffusivity between the coatings produced with either the spherical or angular particles was a result of microcracks. The coatings produced from spherical particles had fairly randomly oriented microcracks that were 30-50 μm long and 0.5-2.0 μm wide. The coatings produced from the angular particles had many more cracks that were approximately 25 μm long and 1-3 μm wide. The majority of cracks in the coating produced from the angular particles were oriented with their long axis perpendicular to the heat flux (parallel to the surface of the substrate). This demonstrated the importance of crack orientation. A crack parallel to the direction of the heat flow had only a minimal effect on the thermal conductivity, as compared to a crack which was perpendicular to the heat

flow. The effective thermal conductivity (λ_{eff}) for the two orientations was determined by Hasselman[45] and is as follows:

$$\lambda_{eff} = \frac{\lambda_0}{(1 + 8Nb^3/9)} = \text{Effective thermal diffusivity for randomly oriented cracks.} \quad (24)$$

$$\lambda_{eff} = \frac{\lambda_0}{(1 + 8Nb^3/3)} = \text{Effective thermal diffusivity for perpendicular cracks.} \quad (25)$$

where λ_0 is the thermal conductivity of a crack-free coating, N is the number of cracks per unit volume and b is the radius of randomly oriented penny-shaped cracks.

Thermal diffusivity tests conducted by Youngblood et al.[42] focused on the effects of oxygen lattice defects, impurities, second phases, grain-boundary phases and phase boundaries. They, as well as Williams et al.[46] studied the means by which heat was transferred through the YSZ coatings. Gitzhofer et al.[47] determined that at lower temperatures, phonons were responsible for thermal diffusivity. As the temperature was increased, photons began to contribute to the thermal diffusivity. As the temperature was increased to roughly 400 °C, the thermal diffusivity decreased by roughly T^{-1}. Once 400 to 500 °C was exceeded, the thermal diffusivity began to increase by a value which was approximately proportional to (T^3).[47] The total diffusivity (λ) as determined by Gitzhofer et al.[47] was equal to the sum of the diffusivities that resulted from phonons or lattice vibrations and photons.

$$\lambda = \lambda_g + \lambda_p \tag{26}$$

λ_g = Diffusivity from phonons or vibrations
λ_p = Diffusivity from photons

As the temperature exceeded approximately 400 °C there was a noticeable increase in the materials thermal diffusivity. Miller et al.[48] determined that this was caused by an increasing contribution to the thermal diffusivity from radiation effects. Youngblood et al.[41] determined that this upturn in single YSZ crystals tended to occur at lower temperatures with increasing yttria content. This was related to the optical properties of the material. Crystals which were fully cubic (stabilized) were transparent and hence conducted heat efficiently. As the yttria content was decreased to approximately 7-8 wt% the crystals became milky in appearance and at 5 wt% were opaque white. This was due to the increasing size and volume fraction of precipitates that were present in the various crystals. These precipitates caused increased scattering at both visible and infrared wavelengths. The radiative wavelength decreased as the temperature increased to the point where it was roughly the size and/or spacing of the precipitate structure. This resulted in increased scattering. This behavior applied only to single crystals.

Polycrystalline YSZ materials displayed no change in the thermal diffusivity as the temperature was increased.[41, 44, 46, 47] This was the result of optical scattering from impurities. These impurities may have been due to fine grain size, oxygen vacancies or

even inclusions which might have been added to the material for the sole purpose of lowering the value of the thermal diffusivity.

Failure Mechanism of Thermal Barrier Coatings:

Thermal barrier coatings are usually duplex coatings. This means that the coating consists of a bond coat which helps to minimize the mismatch in the coefficient of thermal expansion of the substrate and the ceramic coating. The consensus is that the failure of YSZ TBC's is rooted in the oxidation of the bond coat.[48-50] Further, if oxidation of the bond coat can be suppressed then the performance of TBC's might be enhanced by the reduction of stresses which result from bond coat oxidation.

Miller and Lowell [48] subjected cylindrical René 41 superalloy test specimens (1.3 cm diameter) which were coated with 0.01 cm of a Ni-14 wt% Cr-14 wt% Al-0.1 wt% Zr bond coat and 0.04 cm of an 8 wt% Y_2O_3-stabilized ZrO_2 TBC to Mach 0.3 burner rig tests. This simulated the conditions which are present in an operating turbine engine. They found the life of the coating was strongly dependent on the cycle duration. Samples exposed to 1200 °C for 1 hour failed after an average of 13.4 cycles. Using time-lapse and high-speed motion pictures, Miller and Lowell[48] noticed that one to two cycles before the coating spalled, the region which was about to fail would heat up very rapidly. They also noticed that these locations sounded as if there were detached when they were tapped with a coin. A scanning electron microscopy (SEM) micrograph

showed that the coating delaminated just above the bond coat before spalling. Energy-dispersive X-ray analysis revealed that the bond coat had oxidized significantly and the oxide was mostly alumina with some spinel. The oxides had formed on the surface of the bond coat which was towards the TBC.

Miller and Lowell[48] conducted tests where specimens which were exposed to thermal blasts for 30 seconds showed no signs of failure for over 10,000 cycles. The thermal stresses reached a maximum at only 2 seconds of exposure. Therefore the thermal stresses alone were insufficient to cause failure. Samples which were exposed to 1250 °C temperatures for 23 and 50 hours failed while undergoing cooling. The bond coating of these samples again showed significant oxidation which further reinforced the notion that oxidation of the bond coating was the major cause of failure. Even specimens which were heated for only 5 hours at 1250 °C delaminated after being slowly cooled. Therefore, thermal shock was not the mode of failure. Finally, specimens heated to 1250 °C in an inert argon environment showed no signs of failure. The conclusion of Miller and Lowell[48] was that oxidation of the bond coat was the primary source of failure for YSZ TBC's.

Miller and Lowell[48] determined that YSZ TBC's failed in the region of the interface of the bond coat with the YSZ on cooling from high temperature exposure with air even when the cooling rate was very slow. The stresses that arose from metal-ceramic thermal mismatch (the bond coat was metallic) and not thermal shock

caused the failure. When the thermal expansion mismatch between the coating and substrate was minimized, the life of the coating was extended.

Using a balanced biaxial stress state approximation and assuming a thin coating, Miller and Lowell[48] arrived at an expression for the thermal expansion mismatch (equation 27).

$$\sigma_{\Delta T} = \Delta T \Delta\alpha \frac{E}{(1-\mu)} \tag{27}$$

ΔT = Difference between the temperature after cooling and the reference (stress free) temperature (as high as 400 °C).

$\Delta\alpha$ = Difference in coefficient of thermal expansion between the metal and the ceramic (roughly 5×10^{-6} C^{-1})

E = Elastic modulus of the ceramic 4.8×10^{4} MPa.

μ = Poisson ratio (0.25).

The significant point here is that the thermal barrier coating failed only after the bond coat had been oxidized. The durability of the TBC was directly related to the ability of the bond coat to resist oxidation. Sun et al.[49] suggested an alumina barrier between the TBC and bond coat would provide an excellent adhesive material for the

YSZ and effectively protect the bond coat from oxidation, although they had conducted no work to this effect. Others have proposed that after the bond coating, alternating layers of alumina and YSZ would provide increased life as well as potential photon scattering sites to lower thermal diffusivity while minimizing the necessity for thick (250 μm) depositions.[6,7]

CHAPTER 3

PROJECT OUTLINE

During this project zirconia alone was first deposited using metal chlorides to determine the suitability of this method to produce adequate coatings. Once appropriate parameters for this deposition were determined, an attempt was made to deposit yttria alone using an organometallic precursor. Next, zirconia was deposited using an organometallic precursor and this process was evaluated. An effort was made at meshing the two methods in order to deposit yttria stabilized zirconia. Finally, gasses and precursors were altered and pulsed to produce a coating with alternating layers of zirconia and alumina.

To facilitate this research, other methods of depositing zirconia, yttria and yttria-stabilized zirconia (YSZ) were first examined (refer to Chapter 2). The deposition of alumina was studied as part of a separate project.

This research was concerned with the chemical vapor deposition of zirconia based coatings in an attempt to determine optimum deposition rates as well as the feasibility of producing thermal barrier and layered coatings using chemical vapor deposition. Characterization of the microstructure and composition of the coating were also investigated. The research proceeded according to the following outline:

I Preparation of YSZ by CVD

A) Role of precursors.
   1) Deposition of ZrO_2 - $ZrCl_4$ vs. $Zr(tmhd)_4$ (2,2,6,6-tetramethyl-3,5-heptadionate)
   2) Deposition of Y_2O_3 - $Y(tmhd)_3$ (2,2,6,6-tetramethyl-3,5-heptadionate)
   3) Oxygen source [(CO_2 + H_2) vs. O_2 vs. N_2O]

B) Parameter effects on deposition: Reaction kinetics and microstructure.
   1) Temperature
   2) Pressure
   3) Reagent Concentration

C) Design and construction of a new, state-of-the-art CVD reactor with computer interface via LabVIEW™.

D) Investigate feasibility of producing layered coatings (alternating layers of zirconia and alumina).

II Microstructure Characterization

A) Analysis of coatings using scanning electron microscopy (SEM), energy dispersive spectroscopy (EDS), X-ray diffraction (XRD) and Auger electron spectroscopy (AES).

B) Range of microstructure variation
   1) Nano-phase to near-amorphous structure (low temperatures coupled with supersaturation of reactant.)[51, 52]
   2) Columnar (preferred orientation)[3,5]
   3) Whiskerish (high temperature coupled with lower concentrations of reactants.)[51]
   4) Creation of photon scattering sites

While the overall kinetics of the chemical reactions invlolved were far too complex to determine, an attempt was made to optimize the overall reaction. This was

done by systematically varying the parameters which were deemed to be most influential on the rate at which the deposit was formed.

The precursors played an important role in determining the rate of reaction and hence the rate of deposition. An yttria organometallic [yttria 2,2,6,6-tetramethyl-3,5-heptadionate or $Y(tmhd)_3$] was chosen because of its relatively high vapor pressure and low dissociation temperature. The choice was not as clear with the zirconium precursor. Coatings were made using $ZrCl_4$ as well as a zirconium organometallic, $Zr(tmhd)_4$. A comparison was made concerning the effect of changing zirconium precursors. The zirconium precursor which produced the best initial results was the one which was pursued.

There were also several choices concerning the introduction of oxygen into the system. One method was to supply pure oxygen to the reaction chamber. Another option was the use of nitrous oxide (N_2O) as an oxygen source. Yet another option was the reaction between CO_2 and H_2 (equation 28):

$$CO_2 + H_2 \rightarrow H_2O + CO \qquad (28)$$

These sources of oxygen were examined to determine which was most suitable to the deposition of these zirconia based coatings. As with the zirconium precursors, the oxygen source which produced the best initial results was the one which was pursued.

Not only were the precursors varied, but so were the reaction's parameters. Deposits were made at varying temperatures, pressures and reagent concentrations. Duret and Pichoir[14] characterized CVD coatings according to Figure 1.

Variation of the major parameters (temperature, pressure and concentration) affected not only the rate of deposition but also the microstructure. The preferred microstructure for YSZ TBC's is columnar (several μm in diameter) and oriented roughly perpendicular to the surface of the coated part (refer to Figure 2). It was felt, however, that a nanophase structure would be better for multi-layered coatings.

CHAPTER 4

EXPERIMENTAL APPARATUS

During this research, four different CVD reactors were used. This was an unavoidable development as reactor time was a premium commodity. It was felt initially, however, that the region in which deposition occurred was similar enough to cause little if any variation in coatings which were directly attributable to the reactors' geometry. It was later seen that reactor geometry, even when varied slightly, caused observed results to vary.

Reactor 1:

A schematic diagram of the reactor which was first used to deposit zirconia appears in Figure 9 (a photograph appears in Figure 10). The design was that of a cold-wall CVD reactor. The horizontal reaction chamber was constructed from a 5.50 cm inside diameter (ID) quartz tube. Stainless steel flanges with compression O-ring fittings were used to seal the reactor assembly. Radio frequency (RF) coils were used to heat nickel substrates (99.994%, ALFA, Danvers, MA)[†] to be coated while not directly heating the walls of the reactor. The samples being coated, however, were small enough

---

[†] Sources of chemicals and equipment will be mentioned only once. Any further reference to a given chemical or device without specific reference to a manufacturer indicates that it was obtained from the source which was previoiusly mentioned.

to prevent effective heating. As a result, a 3.72 cm ID inconel tube was placed within the quartz tube to act as a susceptor. This effectively changed the reactor from a cold-wall type to a hot-wall type reactor. Zirconium tetrachloride ($ZrCl_4$) was used as a precursor. The $ZrCl_4$ was obtained by packing zirconium sponge (99.999%, Alfa Products, Danvers, MA) into a 2.20 cm ID inconel pipe (8 cm in length) and passing Cl_2 through the sponge via a 0.43 cm ID inconel pipe. Argon was introduced through a separate 0.43 cm ID inconel pipe as a carrier gas in order to transport the $ZrCl_4$ to the substrates. A tube furnace was used to heat the pipe containing zirconium to approximately 850 °C to facilitate chlorination. The temperature was adjusted using a variac and measured by means of an optical pyrometer. The flow rates of Ar, Cl_2, CO_2 and H_2 (99.995%, Alphagaz, Morrisville, PA) were controlled using flow meters (1259B, MKS, Andover, MA) coupled with a four channel flow controller (RS247-B, MKS, Andover, MA). The chlorination of zirconium was relatively constant at about 70%. This was based on the amount of zirconium consumed during a run (based on weight loss). The incomplete chlorination was probably due to the limited surface area of zirconium which was exposed to chlorine. It was felt that a chlorinator with an increased surface area of Zr would have resulted in 100% chlorination (this was later confirmed).

Before any runs were performed, a temperature profile of the reactor was

developed. This temperature profile of the CVD reactor appears in Figure 11. As an interpretation aid, a sketch of the reactor appears above the temperature profile plot (gas flows from left to right). The reactant gasses were introduced from the left. The far right of the sketch was the exhaust end of the reactor. A type K thermocouple (chromel alumel, ARi Industries Inc., Addison, IL) was inserted through a modified gas feed line (left of the reactor as it appears in Figure 11) and extended past the RF coils (far right of the reactor as it appears in Figure 11). The RF generator was set to produce a temperature of 1100 °C using an optical pyrometer. The tube furnace was set at approximately 850 °C by adjusting a variac accordingly while using an optical pyrometer to measure its temperature. It was assumed that the temperature profile would be roughly the same for other temperature settings. Argon was allowed to flow through the reactor at a rate which was approximately the same as that which would be provided from the total flow rate during an actual run. After the reactor's temperature had stabilized a temperature reading was taken and the thermocouple was slid out in 1 cm increments. The thermocouple's readout was allowed to stabilize and another temperature reading was obtained. This procedure was repeated until the thermocouple was completely removed from the reactor. Temperatures beyond the RF coils were of no great concern since this area consisted of exhaust gas. The only concern in this region was that the temperature be sufficiently high so as to prevent condensation of the exhaust gas which might clog the reactor.

The temperature profile shows that the tube furnace provided a relatively uniform temperature for the chlorination of zirconium. The RF generator, however, demonstrated a sharp drop off at its end (the right end of the RF coils as presented in Figure 11). Since the RF coils generated the temperature necessary for the oxidation of zirconium tetrachloride, the substrates for all subsequent reactions were placed at the leading (left) end of the RF coils where the temperature was relatively uniform.

Initially, depositions of zirconia were made using this reactor. This provided information concerning the feasibility of producing zirconia using a metal chloride precursor. The abilities of this reactor, however, were limited. It had been in almost constant use for nearly ten years. The reactor itself was far from leak proof and the temperature was difficult to control using the optical pyrometer. It was used mainly as an instructional device as well as a means to investigate the deposition of zirconia from metal chlorides. Once this reactor had served its purpose, it was dismantled and a new reactor was designed and constructed (Figure 12).

Reactor 2:

A schematic diagram of the second reactor used appears in Figure 12 (a photograph appears in Figure 13). As with the first reactor, this reactor was a hot-wall type but used a graphite susceptor which was encased in a sealed, double walled quartz tube and held under a vacuum. A Honeywell temperature control (Honeywell Industrial

Automation and Control, Fort Washington, PA) and type K thermal couple were used to set, control and maintain the RF furnace's temperature. This was a great improvement over the previous reactor whose temperature was measured using an optical pyrometer while the RF power was set using a substantial amount of guess work. This new reactor was designed to be interfaced with an Apple Quadra through the computer program LabVIEW™ (National Instruments, Austin, TX) so that extended runs might be conducted. This setup allowed gas flow, temperature and pressure to be changed during a run. This reactor was designed with the goal of producing nickel aluminide and aluminum oxide functionally graded materials (FGM's) as a bond coat with the thermal barrier coating (TBC) layer deposited on top in a single run. In addition, this new reactor lent itself to the formation of layered coatings, namely alternating layers of YSZ and alumina. Other features of the new reactor included a new Leybold Trivac D40BCS rotary vane pump (Leybold, East Syracuse, NY) with a pumping speed of 70 cubic feet per minute and an ultimate partial pressure of 3×10^{-2} Torr. In addition, a specimen exchange chamber (Multi-Motion Feedthrough, linear travel 14 inches, Huntington Laboratories, Mountain View, CA) was incorporated into the overall design such that samples could be inserted and removed without having to loose vacuum pressure or turn off the RF furnace. This allowed the system to be kept intact with constant pressure and temperature maintained at all times. This reduced downtime and problems resulting from leaks which occurred during reassembly of the old reactor after samples had been

exchanged. As a result, a more stable environment could be maintained to allow for greater repeatability between runs.

An alumina tube with an ID of 4.45 cm was used for the horizontal reaction chamber on this reactor. This was done to eliminate silicon contamination in the coatings produced. Contamination occurred when the quartz tube reacted with the chlorine and/or hydrogen to produce silicon tetrachloride ($SiCl_4$) or silane (H_4Si). This did not appear to be a tremendous problem during the deposition of zirconia and yttria from organometallics, but it did prove detrimental to the deposition of zirconia and alumina in chloride processes. Stainless steel flanges with compression O-ring fittings were used to seal the reactor assembly. Gasses flowed into the reactor via 0.43 cm ID inconel piping as with the first reactor. Gas flow was controlled using flow meters coupled with a mass flow controller (RS272-C, MKS, Andover, MA). While the flow meters were the same as those used on the first reactor, the RS272-C flow controller was chosen because it was more easily coupled to the Apple Quadra using LabVIEW™ than the RS272-B.

Once the new reactor had been constructed, an extensive amount of time was spent searching for leaks using an ULVAC portable leak detector (DLMS-531 Turbo Mass Spectrometer Type). Weldments were examined and repaired where necessary. Vacuum coupling Radlad (VCR) fittings were checked and either tightened or replaced as the case warranted. Once the reactor was deemed suitably leak-proof, a temperature

profile was obtained in a manner similar to that used for the first reactor. The only area of concern was the RF region of the reactor and the results appear in Figure 14. It was immediately evident that the temperature in the RF furnace was much more constant in the new reactor than in the old one. This meant that all substrates would be exposed to the same temperature during the coating process, thereby producing improved results. Yeckel and Middleman[31] stressed that an isothermal zone was essential for uniform deposition.

Organometallics [$Zr(tmhd)_4$ and $Y(tmhd)_3$] were used as precursors in the second reactor. These were placed in vaporizers (225 cc, Morton, Danvers, MA) with the aid of a disposable glove box to prevent contamination. An additional vaporizer (450 cc, Morton, Danvers, MA) contained aluminum pellets which were to be chlorinated and used for the deposition of alumina (Al_2O_3) in work separate to this. Heating jackets were designed and constructed to fit the three vaporizers. These consisted of copper or stainless steel pipes which had an inner diameter equal to the outer diameter of the vaporizers. The pipes were wrapped with heating tape (Thermolyne BriskHeat, Dubuque, IA) which were covered with an insulating fabric. Type K surface mounting thermocouples (OMEGA Engineering, Inc., Stamford, CT) were attached to the side of each vaporizer and controlled using either OMEGA CN9000 (OMEGA Engineering, Inc., Stamford, CT) or an EUROTHERM 91e (EUROTHERM Corporation, Reston, VA) temperature controls. Work had been conducted with an identical vaporizer which

had been modified to allow the insertion of a type K thermocouple so that it came into direct contact with the precursor. The difference between temperature readings obtained from within the vaporizer and from the outer wall of the vaporizer differed by ≈2 °C, with the outer wall producing the higher of the two readings. This difference was minimal enough to allow for readings to be obtained from outside of the vaporizer which were considered accurate and used in the determination of precursor vapor pressures.

The next step was to wrap all the lines which were downstream of the vaporizers with heating tape so as to prevent condensation of the vaporized precursors within the lines. Once wrapped with heating tape, the lines were covered with aluminum foil (Reynolds Wrap, Heavy Duty) for insulation. Again, type K surface mounting thermocouples were mounted directly to the lines in order to monitor and control the temperature. The lines were kept between 20-80 °C hotter than the vaporizers at all times to assure no condensation would form within them.

Reactor 3:

A schematic diagram of the third reactor used appears in Figure 15 (a photograph appears in Figure 16). It was a hot-wall type similar to the second reactor but without the sophisticated controls. The horizontal reaction chamber consisted of a quartz tube with a 5.5 cm ID. Stainless steel flanges with compression O-ring fittings were used to seal the reactor assembly. The temperature profile for the third reactor appears in Figure

17. As with the second reactor, only the RF region was examined since it was the only region of concern. The temperature profile revealed an area located in the center portion of the RF region where the temperature was relatively constant. The samples were placed in this region.

A vaporizer filled with $ZrCl_4$ and was used as the source for the deposition of zirconia. As with the second reactor, the vaporizer was placed in a heating jacket. The lines (0.43 cm ID) were wrapped with heating tape, insulated and kept at a temperature higher than that of the vaporizer to prevent condensation of the precursor. Line and vaporizer temperatures were monitored and controlled using type K surface mounting thermocouples and OMEGA CN9000 temperature controls. Equipment similar to that used in the second reactor was employed to control the flow of gasses. Inconel pipes with an inner diameter of 0.43 cm were used to introduce the gasses into the reactor.

Reactor 4:

A schematic diagram of the fourth reactor appears in Figure 18. The third reactor was simply modified by the addition of a tube furnace (similar to the arrangement used for the first reactor, Figures 9 and 10). The injector from the first reactor was improved upon to result in 100% chlorination of the zirconium and thus provide a better supply of precursor. The inconel injector filled with Zr sponge was replaced with a quartz tube (0.7696 cm ID) packed with 1.0 mm diameter Zr wire (99.5%, Johnson

Matthey Catalog Company, Ward Hill, MA). A vaporizer filled with $AlCl_3$ (99.997%, Johnson Matthey, Ward Hill, MA) and heated to 100 °C in an oil bath was used as an aluminum source for the production of alumina in layered coatings. The temperature profile of this reactor appears in Figure 19 and includes the tube furnace region. Samples were placed more towards the exhaust end of the RF region (roughly between 48-53 cm on the temperature profile) where the temperature was relatively constant.

CHAPTER 5

PROCEDURES

Reactor 1:

The first reactor (Figures 9 and 10) was used primarily to determine reasonable flow rates for the various gaseous reactants as well as suitable deposition temperatures and pressures required to produce zirconia. Figure 20 shows how the growth rate of a CVD coating may be affected by the total flow rate of gas. Theoretically, zero flow rate would lead to a finite deposit at the point at which the gaseous reactants reside. An infinite flow rate would theoretically lead to an infinitely thin, albeit even, coating. The ideal situation lies somewhere between these extremes.

Work done by Sipp et al.[12] as well as Brennfleck et al.[13] was used as a guide in setting the temperatures (refer to Figure 11) and pressure. The temperature of the tube furnace which was used to promote the chlorination of zirconium was set at 850 °C. Flow rates were adjusted until a mixture was found which consistently produced the desired results, namely ZrO_2 deposition. Once acceptable flow rates were determined, the deposition temperature was systematically varied at a low system pressure (5 Torr) and at a high system pressure (45 Torr). Growth rates and morphologies for the varying conditions were compared and contrasted.

A typical run began by first weighing the empty injector. The injector was then packed with zirconium sponge and weighed again to determine the amount of zirconium present in the injector. The injector was put in place and the necessary gas lines were connected.

The nickel substrates that were to be used were measured and weighed. The substrates were then placed on an alumina support and carefully slid into place using a metal rod. The reactor was sealed and pumped down to the desired pressure. Argon was allowed to flow into the reactor. The variac powering the tube furnace was activated and the tube furnace was allowed to reach ≈850 °C. The temperature was monitored using an optical pyrometer.

Once the tube furnace had reached the desired temperature, the RF generator was turned on and allowed to stabilize at the desired temperature. Again, an optical pyrometer was used to determine the temperature of the nickel substrates as they rested on the alumina support. Generally, the heat from the RF generator would cause the temperature in the tube furnace region to increase. This, however, was not considered to be a problem.

After both the tube and RF furnaces had stabilized, CO_2, H_2 and Cl_2 were allowed to flow into the reaction chamber. A digital timer was used to measure the duration of the run. Towards the end of each run, the control valve on the chlorine tank was turned off and the chlorine was evacuated from the line. This step prevented undue corrosion

of this line. Once the chlorine had been evacuated from the line the timer was stopped. The CO_2 and H_2 flows were then ceased. Both the RF generator and tube furnace were turned off and the reactor was allowed to cool. Argon continued to flow until the reactor had reached room temperature and was opened (≈2 hours). The substrates were removed and weighed again in order to determine if any deposit had formed. The injector was then removed and weighed to determine how much zirconium had been consumed during the run. This information was used to calculate the chlorination efficiency.

Reactor 2:

The second reactor (Figures 12 and 13) was specifically designed and constructed to examine the production of various coatings for turbine applications using CVD. These coatings included zirconia, yttria-stabilized zirconia, alumina, nickel aluminide, functionally graded materials (FGM's) and layered coatings. This reactor was constructed as part of the Advanced Turbine Systems (ATS) program and invlolved a number of projects being conducted by several researchers.

On this reactor, metalorganics [$Zr(tmhd)_4$ and $Y(tmhd)_3$] were used as precursors for the deposition of zirconia, yttria and yttria-stabilized zirconia. Separate vaporizers were loaded with 25 mg of the metalorganic. Work conducted by Akiyama et al.[37], Pulver et al.[38] and Balog et al.[53] was used as guidance in setting the parameters. The

vaporizer containing the $Zr(tmhd)_4$ was covered with a heating jacket and heated to between 150-230 °C. The $Zr(tmhd)_4$ was stable to 240 °C and decomposed at 300 °C. The vapor pressure of $Zr(tmhd)_4$ was determined using the equation developed by Pulver et al.[38] (refer to equation 20) and ranged from 0.0883-2.1437 Torr. The argon carrier gas flow rate was varied from 15-200 cc/min. The flow rate of $Zr(tmhd)_4$ being delivered to the reactor was then calculated using equation 29.

$$\upsilon_{precursor} = \frac{P_{precursor}}{P_{system} - P_{precursor}} \times \upsilon_{carrier} \tag{29}$$

where:

$\upsilon_{precursor}$ = Precursor flow rate in $\left[\frac{cm^3}{\text{min}}\right]$
$P_{precursor}$ = Vapor pressure of the precursor [Torr]
P_{system} = Overall pressure of the reactor [Torr]
$\upsilon_{carrier}$ = Flow rate of carrier gas (argon) $\left[\frac{cm^3}{\text{min}}\right]$

Equation 29 provides only an estimate of flow rates, however, this was all that was requred since no modeling of the reaction was being conducted. The flow rate of $Zr(tmhd)_4$ delivered to the substrate was varied from 0.1336-14.2053 cc/min.

The $Y(tmhd)_3$ was heated to 120 °C. It was not heated to any higher temperatures since this would have caused it to degrade. At 120 °C the vapor pressure

of $Y(tmhd)_3$ was ≈1 Torr and the flow rate of $Y(tmhd)_3$ was 4.6209 cc/min with an argon carrier gas flow rate of ≈200 cc/min.

The flow rate of all the gaseous reactants concerned, along with vaporization and deposition temperatures, was varied in an effort to establish effective deposition parameters.

The overall operation of this reactor was similar to the first reactor with some modifications. Thermocouples and temperature controls were used to set, control and monitor all temperatures. The main difference was the care which had to be taken in using the vaporizers. If operated improperly the vaporized precursor would condense within the lines before reaching the reactor or, even worse, be drawn backwards into the mass flow meters. Also, flow rates had to be monitored continuously. A drop in the flow rate usually signaled condensation of the vaporized precursor at a cold spot within the lines. If not corrected, this formed a complete blockage and the lines had to be removed and cleared (a time consuming process).

Each vaporizer was provided with a bypass valve which allowed gas to flow while the vaporizer was closed. This bypass valve would first be closed prior to opening the valves of the vaporizer. Next, the exhaust valve of the vaporizer would be slowly opened all the way. Reactor pressure would be monitored as it usually jumped at this point. Once the pressure had stabilized, the inlet valve of the vaporizer would be slowly opened, allowing the argon carrier gas to pass through the vaporizer and into reactor.

The inlet valve was only partially opened. This allowed for the appropriate flow, as set, but provided a back pressure to prevent precursor from flowing backwards in the lines. Once the precursors were flowing, oxygen would be allowed to flow into the reactor to react with the organometallics.

Once the reaction was complete, the vaporizers were closed off. The inlet valve was first shut, followed by the exhaust valve. The bypass valve was then opened to allow for argon to flow, flushing the lines of the organometallics. CO_2 and H_2 were allowed to continuing flowing, reacting with any remaining metalorganic. The RF generator was then turned off and the reactor was allowed to cool. Once cool, all gas flows were ceased.

Reactor 3:

The third reactor (Figures 15 and 16) used a vaporizer filled with $ZrCl_4$ as a precursor for the deposition of zirconia. The vaporizer was heated to 200 °C with a heating jacket which was monitored and controlled with a type K thermocouple and OMEGA CN9000 temperature control. This resulted in a vapor pressure of ≈ 1 Torr. Argon was used as the carrier gas to transport the vaporized $ZrCl_4$ to the substrate through lines wrapped with heating tape. Hydrogen and carbon dioxide in varying mixtures were used as an oxygen source. In general, the operation of this reactor was the same as the second reactor.

Reactor 4:

The fourth reactor (Figure 18) was simply a modified version of the third reactor which resulted in an arrangement similar to that of the first reactor. Chlorine was passed through zirconium wire and reacted with CO_2 and H_2 to form a zirconia deposit. The flow rates chosen were based on the work conducted with the first reactor. After a set amount of time, the flow of chlorine was ceased. This removed the supply of $ZrCl_4$ and effectively ended the deposition of zirconia.

Next, a vaporizer filled with $AlCl_3$ (heated to 100 °C with a vapor pressure of $\approx$1 Torr) was opened in the same manner as the other vaporizers. Argon was allowed to flow through the $AlCl_3$ filled vaporizer into the reactor. There it was reacted with CO_2 and H_2 to form an alumina deposit. After a set amount of time, the vaporizer was closed (as before) ending the deposition of alumina.

By alternating the above two procedures (deposition of ZrO_2 and Al_2O_3) layered coatings were produced on the substrates.

CHAPTER 6

RESULTS & DISCUSSION

Reactor 1:

Work with the deposition of zirconium oxide via chemical vapor deposition was conducted first using the reactor which appears in Figures 9 and 10. It was felt that a thorough understanding of the deposition of zirconia was required in order to facilitate the deposition of yttria stabilized zirconia (YSZ) and layered, ZrO_2/Al_2O_3. The system which was studied most extensively at first involved the chlorination of metallic zirconium. The $ZrCl_4$ was then oxidized using the reaction of H_2 with CO_2. The reactions which were pertinent to this process appear in equations (1), (2) and (3).

Three substrates were placed on an alumina support at 2, 3 and 4 cm from the end of the RF coils (an uniform temperature region as it appears in Figure 11). The first reactions were run at a pressure of 5 Torr. The temperature was varied from 800 to 1100 °C. The deposition rate on the area of the substrate exposed to the reaction (refer to Figure 18) in microns per hour was roughly calculated based on the change in the mass of the substrates according to the following equation:

$$\frac{\left(\Delta W \times \frac{1}{\rho} \times \frac{1}{lw + 2ld + 2dw})\right)}{t} \qquad (30)$$

where

ΔW = weight gain due to deposition [g]
ρ = density of zirconia $\left| \frac{g}{cm^3} \right|$
l = length of substrate [cm]
w = width of substrate [cm]
d = depth of substrate [cm]
t = duration of run [hours]

This calculation assumed the coating occurred uniformly on only the exposed surface of the substrate (Figure 21). In addition, this calculation assumed a coating which had zero porosity and no impurities. This assumption, however, was eventually proven false so deposition rates were calculated in $\frac{(mg/cm^2)}{hour}$.

Coupling knowledge gained from the available literature along with some trial and error, flow rates which appeared to produce favorable results were determined. They were as follows:

$$\upsilon_{Ar} = 40\frac{cm^3}{\text{min}}$$
$$\upsilon_{Cl_2} = 6\frac{cm^3}{\text{min}}$$
$$\upsilon_{CO_2} = 60\frac{cm^3}{\text{min}}$$
$$\upsilon_{H_2} = 60\frac{cm^3}{\text{min}}$$

Deposits were made at 5 Torr while the deposition temperature was varied from 800 to 1100 °C. A plot of the deposition rate versus temperature appears in Figure 22. Coatings which were made at a deposition temperature in excess of 950 °C displayed a highly crystalline, whiskerish structure which was believed to be monoclinic. These coatings were porous and demonstrated poor adhesion to the substrate. The porosity in these coatings caused a breakdown of equation (30). Calculations made with equation (30) predicted a coating which was less than 7 μm thick. Cursory inspection, however, revealed a coating which was several mm's thick. Although this coating was thick, it displayed poor adherence. In addition, it was extremely fragile and crumbled easily when lightly touched with a fine pair of tweezers.

The highest deposition rate of an adherent ZrO_2 coating was observed at 950 °C when the pressure was 5 Torr. This appeared to be the optimum deposition temperature at this pressure with the aforementioned flow rates.

The deposition of zirconia at 5 Torr followed an Arrhenius law [equation (31)]. The Arrhenius plot for these runs appears in Figure 23. The apparent activation energy was calculated to be $E_a = 44.79\ \frac{kcal}{mole}$ ($182.66\ \frac{kJ}{mole}$) using equation (31).

$$\ln k = \ln k_0 - \left(\frac{E_a}{R}\right)\frac{1}{T} \qquad (31)$$

where:

k = reaction rate
k_0 = rate constant (T = ∞)
E_a = activation energy

R = gas constant
T = temperature

The activation energy, as calculated, is referred to as apparent since the value is dependent upon reactor geometry. A different reactor geometry would yield a different activation energy. The activation energy as calculated by Sipp et al.[12] $\left(40\frac{kJ}{mole}\right)$ differs from the value that was obtained here. Both data, however, demonstrated that the reaction obeys Arrhenius laws.

The ZrO_2 coatings produced at 5 Torr were examined using XRD, SEM and EDS. Figures 24 and 25 show SEM micrographs of the surface of a typical ZrO_2 deposit made at a pressure (P) of 5 Torr and a deposition temperature ($T_{Deposition}$) of 950 °C. The zirconia coating appeared to form in clusters (Figure 24). Higher magnification revealed that these clusters were a collection of fine grains ranging in size from ≈0.2-0.7 μm across (Figure 25). An X-ray diffraction pattern of these deposits appears in Figure 26. The diffraction pattern showed the coating to be zirconium oxide of the baddeleyite (monoclinic) form. The strong peak near 42 corresponds to the nickel substrate.

Several of the samples made under the above conditions (P = 5 Torr, $T_{Deposition}$ = 950 °C) were sectioned, mounted in epoxy, and polished. Figure 27 shows a schematical map of a sectioned sample with edges which are on the leading edge, top surface and trailing edge of the sample. Figures 28, 29 and 30 show SEM micrographs of these three surfaces. The leading edge of the sample appears in Figure 28. The leading edge had the reactant gasses impinged directly upon it and, as a result, exhibits the thickest

zirconia coating (≈10 μm at the thickest point). Figure 29 shows the top surface and a ZrO_2 deposit which is substantially thinner (≈2 μm). Finally, the trailing edge along with the thinnest film appear in Figure 30 (<1 μm). A more evenly deposited coating was expected. This indicates that CVD of zirconia may not be a ubiquitous as previously thought.

Figure 31 shows another cross-sectional view of a ZrO_2 coating made at P = 5 Torr, T = 950 °C. The numbers which appear on this micrograph (1-8) refer to where spot EDS scans were performed. These scans were pinpointed to an area which was roughly 10 square pixels. As a result, the number marking the point which was scanned is substantially larger than the area which was actually examined. These EDS scans provided a map of the coating. The first scan (Figure 32) was made squarely over the nickel substrate. This resulted in strong nickel peaks. Also present was some silicon contamination from the quartz tube and a gold peak resulting from the coating used to prevent the sample from charging while in the SEM. The scan also detected small amounts of oxygen and carbon. The oxygen was believed to have been present in the form of nickel oxide (NiO) which resulted from the samples general exposure to the air. The carbon was possibly a result of dust or smearing of the epoxy resin in which the sample had been mounted. The second, third fourth scans (Figures 33-35) were similar to Figure 32, displaying strong nickel peaks with lesser peaks of silicon (contamination) and gold (coating). The fifth scan (Figure 36) was located within the coating. This

produced a strong zirconium peak as well as an increase in the magnitude of the oxygen peak. This was taken as evidence of the presence of zirconia. The silicon peak was also increased. It was believed that silicon was higher here since the contamination would have incorporated itself into the ZrO_2 coating. The presence of Si within the nickel substrate (Figures 32-35) possibly resulted from Si contaminants being pulled free during polishing or was possibly a contaminant within the nickel substrate itself. Zirconium and oxygen were detected in the sixth and seventh scan (Figures 37 and 38, respectively) but was substantially diminished in the eighth scan (Figure 39). The eighth scan also displays a prominent carbon peak. This resulted from the epoxy resin which the sample had been mounted in. Other, smaller carbon peaks which appeared in the other scans are thought to have been caused by dust contaminants or epoxy resin which was smeared during polishing.

Figure 40 shows a coating which was made at P = 5 Torr, T = 1100 °C along with its XRD pattern. This deposit was highly crystalline and appeared to be monoclinic, though this was not determined. The strong, clean peaks present in the XRD pattern reaffirm the highly crystalline nature of this deposit. A match to this pattern was not found, although many patterns were examined. An EDS scan of this coating appears in Figure 41. A strong zirconium peak coupled with a smaller oxygen peak was taken as indications of the presence of a form of zirconia. No nickel peak appeared, indicating that this coating was thicker than the others examined.

Overall, the following pertinent observations were made concerning deposits of zirconia from $ZrCl_4$ at 5 Torr:

1) There was an exponential increase in the rate of deposition with increasing temperature and it followed an Arrhenius equation.

2) The closer the substrate was to the $ZrCl_4$ source, the slower the deposition rate (for T < 1000 °C).

3) Adherent coatings were produced at low temperatures. Porous, non-adherent coatings were produced at temperatures greater than 950 °C.

4) Relatively low deposition rates ($0.796 \frac{(mg/cm^2)}{hour}$ at 950 °C).

Next, using the same flow rates as before, the pressure was increased to 45 Torr and runs were made at temperatures varying from 800 to 1050 °C (the reaction was not run at temperatures as high as 1100 °C because it was felt this would again yield unsatisfactory coatings). Substrates were placed on an alumina support at 1, 2 and 3 cm away from the zirconia tetrachloride source. It was hoped that the closer placement would lead to improved deposition rates. The results of these runs in terms of deposition rate $\left[\frac{(mg/cm^2)}{hour}\right]$ versus temperature appear in Figure 42. This reaction was not observed to obey any Arrhenius laws. Arrhenius plots are linear and this was not observed here (Figure 43). These results agreed with those of Sipp et al.[12], who also failed to observe any Arrhenius behavior at higher pressures.

The ZrO_2 coatings produced at 45 Torr were examined using XRD, SEM and EDS. Figures 44 and 45 show SEM micrographs of the surface of a typical ZrO_2 deposition made at P = 45 Torr, T = 950 °C. While the zirconia deposition appears to have formed predominantly in clusters of small crystals ≈0.6 μm across (as at 5 Torr). There were some larger, well defined crystals present as well (≈1.4 X 4 μm). It would have been preferable to have obtained crystals which were of a more uniform size. This would have indicated a process which was more constant and predictable. Figure 46 shows an XRD pattern of the sample which appears in Figures 44 and 45. The deposit was determined to be zirconia of the baddeleyite (monoclinic) form (as at 5 Torr).

Several samples which had been made under the above conditions (P = 45 Torr, $T_{Deposition}$ = 950 °C) were sectioned, mounted in epoxy, and polished. Figure 47 shows a schematical map of a sectioned sample along with the leading edge, top surface and trailing edge of the sample. Figures 48, 49 and 50 show SEM micrographs of these three surfaces. The leading edge of the sample appears in Figure 48. As was the case at P = 5 Torr, the leading edge exhibited the thickest zirconia coating. Here, however, it is substantially thicker (≈30 μm) and more porous than was observed with the sample prepared at P = 5 Torr. Figure 49 shows the top surface which was of a thickness comparable to that found on the leading edge (≈30 μm) but displayed much less porosity. Finally, the trailing edge appears in Figure 50. The deposit here was substantially thinner (≈10 μm) and not as uniform as the deposits seen on the leading

edge and top surface. The porosity which appeared at 45 Torr was not expected. As at P = 5 Torr, this suggested a process which was less predictable than first suspected.

Figure 51 shows a cross section of a sample prepared at P = 5 Torr, T = 950 °C coupled with spot EDS scans numbered 1-8 as before. These EDS scans appear in Figures 52-59. The first and second scans (Figures 52 and 53) were made well within the nickel substrate and were nearly identical. Large nickel peaks were observed along with much smaller peaks of silicon (contamination from the quartz tube), calcium (origin unknown) and gold (coating to prevent charging in SEM environment). The third scan (Figure 54) was made at the interface of the substrate and the deposit. A strong zirconium peak appeared and dominated along with an oxygen peak while the nickel peaks were greatly diminished. The silicon and calcium (contaminants) peaks were also strengthened substantially, suggesting that the contaminants had been incorporated into the coating. The fourth scan (Figure 55) continued to show a strong zirconium peak, but silicon and nickel peaks were dominant. Scans 5 and 6 (Figures 56 and 57) show a continuing diminishment of zirconium while nickel and silicon remained strong. The seventh scan (Figure 58) displayed an increased zirconium peak. Nickel and silicon remained strong while calcium rebounded to dominate the scan. Finally, the eighth scan (Figure 59) which was made squarely on the mounting showed no nickel or zirconium. The calcium peak, however, increased in size. This suggests that the calcium

contamination was not part of the deposit. Rather, it may have been present within the epoxy mounting or was introduced during polishing.

Figure 60 shows a coating which was made at P = 45 Torr, T = 1050 °C along with its X-ray diffraction pattern. As was observed at higher temperatures at 5 Torr, the deposit formed here was highly crystalline. The crystals, however, were much finer. The EDS scan of this coating appears in Figure 61. The XRD pattern and EDS scan hint that except for crystal size, this was the same as the deposit that was observed at 5 Torr.

The following observances were made from this series of coatings:

1) The rate of deposition did not obey an Arrhenius law.

2) The substrates' distance from the source played less of a role in the rate of deposition than at 5 Torr.

3) Adherent coatings were produced at low temperatures. Porous, non-adherent coatings were produced at temperatures greater than 950 °C.

4) No deposit was formed at 800 °C (unlike deposits at at 5 Torr) but increased deposition rates were observed at higher temperatures that were below 1000 °C. These rates, however, were still relatively slow (2.56 $\frac{(mg/cm^2)}{hour}$ at 950 °C).

Figure 62 shows a comparison of between deposition rates at P = 5 and 45 Torr. For 800 < T < 1000 °C, deposition rates were higher at 45 Torr. Once the temperature

exceeded 1000°C, deposition rates were higher at 5 Torr. The deposits which were formed at T > 1000 °C, however, were undesirable.

The rates of deposition which were observed with this method were considered too be relatively slow. The rate-dominating reaction was suspected to be the formation of H_2O from H_2 and CO_2 (equation 1).[12,13] In an effort to test this theory, an attempt was made at the deposition of metallic zirconium. Carbon dioxide was removed from the admixture of gasses but H_2 remained in order to bind with the chlorine. The deposition rates were observed to increase by as much as a factor of two. This suggested that an alternate source of oxygen might improve deposition rates. Reactions using pure oxygen without hydrogen produced no coatings. The presence of hydrogen may be required for the binding of chlorine. A mixture of oxygen and hydrogen may have produced the desired results. This was not deemed prudent here, however, given the equipment and high temperatures.

Nitrous oxide was next used as an oxygen source with zirconium tetrachloride. This produced mixed results. While the reactivity of N_2O was much greater than that of CO_2 and H_2, the reaction was uncontrollable. At temperatures as low as 350 °C, a reaction occurred at the exhaust end of the chlorinator (before the reactants ever reached the substrates). The deposit formed was an extremely fine powder formed by gas phase nucleation. This may be the oxygen source of choice for industrial purposes, however, it was thought to be too reactive to control with the given equipment.

The efficiency of the chlorination of zirconium was examined throughout the deposition of zirconia. Efficiency ranged from approximately 65% to as high as 92%. There appeared to be no consistency to the efficiency of the chlorination of zirconium. Once the chlorinator was packed with zirconium sponge, as many as a dozen runs might be performed before the existing zirconium sponge was replaced. While the highest efficiency was always obtained from fresh, unreacted zirconium, results became muddled after that. Under virtually identical conditions, one run would produce, say, 75% chlorination efficiency, while the next run might produce 90%. The unpredictable chlorination of zirconium was most likely due to the small size of the chlorinator, which could hold only a little over 100 g of zirconium sponge, coupled with the possible formation of a protective zirconia coating on the surface of the Zr sponge. A larger chlorinator (possibly a fluidized bed reactor) coupled with a longer dwell time of chlorine should result in 100% chlorination of zirconium. This, however, might be a $50,000 answer to a $50 problem. Therefore, the decision was made to examine the zirconium metalorganic as a precursor. It was felt that a more consistent supply of reactable zirconium could be obtained from an organometallic.

Next, a vaporizer was filled with an yttrium metalorganic [$Y(tmhd)_3$] and several attempts were made to deposit yttria using the first reactor. Control of flow rates and leaks in the system proved to be problematic and the attempt to form coatings from

organometallics using this reactor were abandoned. This reactor was disassembled and construction of the new reactor was begun.

Reactor 2:

Zirconium and yttrium metalorganics [$Zr(tmhd)_4$ and $Y(tmhd)_3$, respectively] were used as the precursors in the second reactor (refer to Figures 12 and 13). These were heated in vaporizers, as was described earlier. Attempts were made first at depositing $Zr(tmhd)_4$ before attempting to introduced the stabilizing yttria. Depositing zirconia from the metalorganics, however, was much more difficult than had been expected. Often, the result was oxidation of the nickel substrate with no deposit at all.

The zirconium precursor was heated to between 150-230 °C. This resulted in a vapor pressure of 0.0883-2.1437 Torr (refer to equation 22). Oxygen was used as an O_2 source since the formation of H_2O from H_2 and O_2 was suspected to be the rate limiting reaction (refer to equation 28). Also, the presence of H_2 was not required to bind Cl_2. Flow rates were adjusted as well as the deposition temperature. It was believed that the higher reactivity of the organometallic would allow for lower deposition temperatures. The deposition temperature was varied between 500-1050 °C. Deposits were produced under the following conditions:

$T_{vaporizer} = 180$ °C
$T_{Line} = 200$ °C
$T_{Deposition} = 750$ °C

$$P_{System} = 5 \text{ Torr}$$
$$P_{Zr(tmhd)4} = 0.3331 \text{ Torr (refer to equation 22)}$$
$$\upsilon_{Ar} = 70 \frac{cm^3}{\text{min}}$$
$$\upsilon_{Zr(tmhd)4} = 5 \frac{cm^3}{\text{min}} \text{ (refer to equation 29)}$$
$$\upsilon_{O2} = 50 \frac{cm^3}{\text{min}}$$

The deposit which was formed, however, appeared quite soft and were easily damaged with a pair of sharp tweezers.

The above conditions resulted in a deposition rate of 0.2074 $\frac{(mg/cm^2)}{hour}$. Samples were examined using a SEM and a typical deposit appears in Figure 63. The sample was examined using X-ray diffraction and EDS. Despite careful examination, only nickel and nickel oxide were detected. The sample was next examined using Auger electron spectroscopy (AES), which has much higher sensitivity than either XRD or EDS. Figure 64 shows the sample and the area which was examined using AES. The results of the AES scan (spectrum and atomic concentrations) appear in Figure 65. Oxygen (57.26 At%) and zirconium (21.80 At%) were detected in roughly a 2:1 ratio. This was taken to be ZrO_2. Nickel (20.94 At%) was also detected. The nickel was believed to have reacted with the oxygen to have formed nickel oxide (detected using XRD).

Cursory inspection of Figure 64 reveals that the deposit appears to have formed in clumps, leaving large areas with no deposit at all. AES was performed on one of the clumps as well a an uncoated area. Figure 66 shows the areas which were examined with numbers (1) to denote the clump examined and (2) the uncoated area. The

spectrum and atomic concentrations appear in Figures 67 and 68, respectively. Zirconium (9.61 At%), oxygen (38.14 At%) and nickel (23.48 At%) were detected (ZrO_2 and NiO) within the deposited clump. In addition, chlorine (2.83 At%) was detected although chlorine was not used in this process. The reactor, however, had been used to form alumina (Al_2O_3) using aluminum trichloride ($AlCl_3$) as a precursor. This was believed to have been the source of the contamination. More disturbing was the detection of a substantial amount of carbon (25.93 At %). This could only have resulted from the organometallic precursor used. Figure 68 shows the AES spectrum and atomic concentration of the bare spot from Figure 66. The majority of this area was nickel (42.32 At%) and oxygen (36.26 At%). This was believed to be nickel oxide. Chlorine was also detected (6.69 At%) as well as a substantial amount of carbon (14.73 At%).

The low deposition rate [$\approx 0.2074 \frac{(mg/cm^2)}{hour}$] coupled with poor morphology and carbon contamination forced a change in the deposition conditions. The system pressure was increased from 5 to 45 Torr. Higher pressures had led to increased deposition rates under certain conditions in Reactor 1, and it was hoped that it would help here. Increased pressures, however, resulted in less precursor reaching the substrate (refer to equation 29). To help counter this, the argon flow was increased. In addition, the temperature was increased substantially. It was hoped that this would have the affect of increasing the deposition rate and eliminating the carbon contamination by promoting the formation of CO_2. A summary of these conditions follows.

$T_{vaporizer} = 180\ °C$
$T_{Line} = 200\ °C$
$T_{Deposition} = 1050\ °C$
$P_{System} = 45$ Torr
$P_{Zr(tmhd)4} = 0.3331$ Torr (refer to equation 22)
$\upsilon_{Ar} = 199\ \frac{cm^3}{min}$
$\upsilon_{Zr(tmhd)4} = 1.5\ \frac{cm^3}{min}$ (refer to equation 29)
$\upsilon_{O2} = 50\ \frac{cm^3}{min}$

Again, the coatings formed were soft and easily scratched.

The above conditions resulted in a deposition rate of $1.2900\ \frac{(mg/cm^2)}{hour}$. The deposit, however, was still undetectable with EDS and XRD. Analysis with AES was again conducted. The results from the AES scan appear in Figure 69. Again, zirconium was detected (14.03 At%) along with nickel (32.92 At%), oxygen (42.87 At%) and carbon (10.18 At%). The chlorine contamination was not present because it had been purged from the reactor over numerous runs. Carbon, unfortunately, was still a problem, even at the elevated deposition temperature.

With the deposition of zirconia from the metalorganics progressing so slowly, a decision was made to proceed to the deposition of yttria from an organometallic [$Y(tmhd)_3$]. Since yttria was to be deposited with zirconia eventually, the system pressure, deposition temperature and oxygen flow rate chosen were identical to those being used to deposit zirconia from $Zr(tmhd)_4$ and appear below:

$T_{vaporizer} = 120\ °C$

$T_{Line} = 140\ °C$
$T_{Deposition} = 1050\ °C$
$P_{System} = 45$ Torr
$P_{Y(tmhd)3} = 1.0212$ Torr[38]
$\upsilon_{Ar} = 199$ sccm
$\upsilon_{Y(tmhd)3} = 4.62 \frac{cm^3}{min}$ (refer to equation 29)
$\upsilon_{O2} = 50\ \frac{cm^3}{min}$

This, however, proved no more successful than depositions using the $Zr(tmhd)_4$. The depositions formed were easily removed from the substrate by scratching with a pair of sharp tweezers.

Deposition rates of 1.5 $\frac{(mg/cm^2)}{hour}$ were measured, but once again the samples proved difficult to analyze. X-ray diffraction and EDS produced little results so AES was again used. The results of the scan along with the atomic concentrations appear in Figure 70. Yttrium was present (14.35 At%) along with oxygen (48.35 At%) and nickel (25.78 At%). Contaminants detected included chlorine (3.20 At%), silicon (8.33 At%). The chlorine was again suspected to have been a remnant from other reactions made within the reactor. The silicon, however, was a bit of a mystery. Other silicon contamination was attributed to the quartz tube which was used for the deposition region. This reactor, however, utilized an alumina tube. The only source of silicon known to be present was in the vacuum grease used to lubricate the O-rings and facilitate sealing.

With mounting frustration, it was decided to attempt depositing YSZ using $Zr(tmhd)_4$ and $Y(tmhd)_3$ as precursors. It was hoped that perhaps co-deposition would lead to improved morphology and adherence. This was not to be the case. Many conditions were tried and led only to the formation of nickel oxide on the surface of the substrate. Eventually, some success was observed under the following conditions:

$T_{vaporizer}$ $[Y(tmhd)_3] = 120$ °C
T_{Line} $[Y(tmhd)_3] = 150$ °C
$P_{Y(tmhd)3} = 1.0212$ Torr[38]
υ_{Ar} $[Y(tmhd)_3] = 199 \frac{cm^3}{min}$
$\upsilon_{Y(tmhd)3} = 51.08 \frac{cm^3}{min}$ (refer to equation 29)

$T_{vaporizer}$ $[Zr(tmhd)_4] = 200$ °C
T_{Line} $[Zr(tmhd)_4] = 230$ °C
$P_{Zr(tmhd)4} = 0.7354$ Torr (refer to equation 22)
υ_{Ar} $[Zr(tmhd)_4] = 500 \frac{cm^3}{min}$
$\upsilon_{Zr(tmhd)4} = 86.23 \frac{cm^3}{min}$ (refer to equation 29)

$T_{Deposition} = 900$ °C
$P_{System} = 5$ Torr
$\upsilon_{O2} = 500 \frac{cm^3}{min}$

As with deposits formed using $Zr(tmhd)_4$ and $Y(tmhd)_3$ alone as precursors, the coatings which resulted from the above conditions was soft and easily scratched with the aid of a sharp instrument.

A deposition rate of 0.42 $\frac{(mg/cm^2)}{hour}$ was observed under the above conditions. Examination was conducted using XRD, SEM and EDS. It was decided that the coatings were of such poor quality, however, that AES would be too costly and reveal little useful information.

An XRD pattern appears in Figure 71. Small peaks representing monoclinic zirconia were hit upon, but no yttria was espied. An EDS scan, however, revealed a strong zirconium peak with a small cleft which may have been the result of yttrium (Figure 72). The strong zirconium peak, coupled with the close proximity of the yttrium peak, would account for this.

An SEM micrograph of a coating obtained from $Zr(tmhd)_4$ and $Y(tmhd)_3$ appears in Figure 73. The coating was not uniform. Clearly visible were what appeared to be microcracks along with grain boundaries. As mentioned earlier, the coating appeared to be rather soft. Figure 74 is an SEM micrograph showing where a scratch had been made on the deposit using a pair of tweezers.

The majority of the coatings obtained using $Zr(tmhd)_4$ and $Y(tmhd)_3$ as precursors consisted of small clusters ≈ 1 μm across. Not uncommon, however, was the formation of larger clumps ($\approx 15 \times 20$ μm). Figure 75 shows an SEM micrograph of such a clump along with a spot EDS scan of it. The nickel peaks were substantially smaller, indicating that the deposition was thicker here than in other areas. It was hypothesized that perhaps once a critical size was reached, deposition occurred at an

increased rate. There was not enough evidence, however, to state this with any certainty.

After much work, the following generalizations were drawn from the chemical vapor deposition of zirconia, yttria and yttria-stabilized zirconia from the metalorganics $Zr(tmhd)_4$ and $Y(tmhd)_3$.

1) Relatively low deposition rates. A summary follows is as follows:
$0.2074 \frac{(mg/cm^2)}{hour}$ obtained from $Zr(tmhd)_4$ at 750 °C.
$1.2 \frac{(mg/cm^2)}{hour}$ obtained from $Zr(tmhd)_4$ at 1050 °C.
$1.5 \frac{(mg/cm^2)}{hour}$ obtained from $Y(tmhd)_3$ at 1050 °C.
$0.42 \frac{(mg/cm^2)}{hour}$ obtained from $Zr(tmhd)_4$ and $Y(tmhd)_3$ at 750 °C.

2) All deposits appeared to be soft, being scratched easily.

3) Carbon contamination seemed to be a nagging problem, even at elevated temperatures (1050 °C).

With the above observations, it was decided that more success was had using $ZrCl_4$ as a precursor. The decision was made to scrap the metalorganics and use $ZrCl_4$ as the precursor. Rather than chlorinating zirconium, however, $ZrCl_4$ was directly vaporized.

Reactor 3:

Zirconium tetrachloride ($ZrCl_4$) was used as a precursor in the third reactor (refer to Figures 15 and 16). It was thought that vaporizing $ZrCl_4$ would yield a higher, more consistent supply of zirconium to the reactor. The concept was to obtain zirconia from $ZrCl_4$ and the stabilizing yttria from $Y(tmhd)_3$.

The $ZrCl_4$ was placed in a vaporizer and heated to 200 °C. The lines were heated to as high as 280 °C, approaching the limit of the heating tapes with which they were wrapped. Unfortunately, the vapor pressure of $ZrCl_4$ was still very low. The precursor repeatedly condensed within the lines, thus clogging them. This occurred even when the lines were kept 80 °C hotter than the vaporizing temperature. Despite the condensation of the $ZrCl_4$ within the lines, the nickel substrate was repeatedly etched. This was presumed to have been done by chlorine which dissociated from the $ZrCl_4$. This resulted in a weight loss for the nickel substrate of ≈0.2 mg. This method was rapidly abandoned.

Reactor 4:

Having met with prodigious failure using $Zr(tmhd)_4$, $Y(tmhd)_3$ and $ZrCl_4$, it was decided that the most promising results had been achieved by using the first method; namely chlorinating metallic zirconium and reacting it with carbon dioxide and hydrogen. Therefore this method was returned to. Reactor 3 was modified to resemble Reactor 1

with some modifications. The injector containing the metallic zirconium was altered to provide a larger surface area of zirconium for chlorination. In addition, the injector was packed with fresh zirconium before each run. This resulted in virtually 100% chlorination on every run. Also, the flow meters used had an increased capacity. This allowed flow rates of argon, carbon dioxide and hydrogen to be doubled. It was felt that increasing the amount of reactant delivered to the substrate would increase the deposition rate and perhaps improve the morphology. Zirconia alone was first deposited under the following conditions:

$$P_{System} = 5 \text{ Torr}$$
$$T_{Chlorination} \approx 600\ ^{\circ}C$$
$$T_{Deposition} = 950\ ^{\circ}C$$
$$\upsilon_{Ar} = 80\ \frac{cm^3}{\text{min}}$$
$$\upsilon_{Cl2} = 12\ \frac{cm^3}{\text{min}}$$
$$\upsilon_{H2} = 120\ \frac{cm^3}{\text{min}}$$
$$\upsilon_{CO2} = 120\ \frac{cm^3}{\text{min}}$$

The increased flow rates appeared to cause a dramatic increase in the deposition rates. Deposition rates of up to 3.23 $\frac{(mg/cm^2)}{hour}$ was observed. This was a substantial improvement over the typical 0.796 $\frac{(mg/cm^2)}{hour}$ which was observed at 5 Torr, T = 950 °C in the first reactor. The SEM micrographs of the coating produced appears at various magnifications in Figures 76-78. The deposit appeared to be a relatively uniform

mixture of small crystals (≈0.4 μm across) and large, blade-like platelets, tapering from ≈1.5 μm to ≈0.4 μm over their length of >3.5 μm. Figure 78 includes an EDS scan along with the SEM micrograph. A large zirconium peak along with an oxygen peak was detected. This was taken to be ZrO_2. The nickel peaks were relatively small indicating a substantial coating. The silicon peak which appears is a contaminant resulting from the quartz tube. These results were looked upon favorably so no further analysis of the samples produced under the above conditions was not performed.

All gasses entering the deposition region in Reactor 4 passed through a tube furnace (used to promote chlorination of zirconium) heated to ≈600 °C. The $Y(tmhd)_3$ would have decomposed well below this temperature so it could not be used as a precursor for the production of yttria. Yttrium trichloride possesses a vapor pressure even lower than zirconium tetrachloride (<1 Torr at 1000 °C). As a result, no attempt was made to add the stabilizing yttria to coatings which were made using Reactor 4. Instead, attempts were made to form a coating which consisted of alternating layers of ZrO_2 and Al_2O_3 (Figure 79). There was some thought that thin layers of zirconia might be stabilized by the surrounding layers of alumina. In addition, while zirconia and yttria-stabilized zirconia are transparent to oxygen, alumina is not. It was felt that a layered coating of zirconia and alumina might lead to an effective thermal barrier coating with enhanced corrosion resistance.

Initially, only one layer of zirconia was deposited, followed by a layer of alumina. The conditions for zirconia were the same as previously discussed for Reactor 4. The precursor chosen for alumina was aluminum trichloride ($AlCl_3$). This had a sufficient vapor pressure at 100 °C (1 Torr†) to provide a good supply of precursor to the deposition region of the reactor. The conditions determined for the deposition of alumina were as follows:

$$P_{System} = 100 \text{ Torr}$$
$$T_{Vaporizer} = 100\ ^\circ C$$
$$T_{Deposition} = 1000\ ^\circ C$$
$$\upsilon_{Ar} = 300\ \frac{cm^3}{min}$$
$$\upsilon_{H2} = 300\ \frac{cm^3}{min}$$
$$\upsilon_{CO2} = 10\ \frac{cm^3}{min}$$

An SEM micrograph of the top layer (Al_2O_3) appears in Figure 80. Immediately evident is the appearance of a relatively smooth deposit with larger nuggets deposited on top. Figure 81 is an SEM micrograph and EDS scan of one of the nuggets which appear in Figure 80. The nugget was made up of very small clumps of deposit that were ≈2.5 μm across. The EDS scan detected a large aluminum peak along with a fair sized peak representing oxygen. This was believed to represent Al_2O_3. The small nickel peak indicated the deposit was rather substantial. A thin coating would have displayed larger

† From "CRC Handbook of Chemistry and Physics, 72ND Edition, 1991-1992" David R. Lide, Editor-in-Chief, CRC Press, copyrigh 1991.

nickel peaks. The gold peak was due to the gold coating placed on the sample to help prevent it from charging within the SEM. Figure 82 shows an SEM micrograph and EDS scan of the relatively flat region which appeared in Figure 80. The coating consisted of fine clusters (≈1.5 μm across), some of which appear to be forming together into larger groups (possibly "infant" nuggets). Again, the EDS scan revealed strong aluminum and oxygen peaks (assumed to be alumina). There also appears to be a zirconium peak. This could be due to a thin area of alumina, resulting in the detection of the zirconia layer below. It could also be a mislabeled gold peak. It should be noted that the $L_{\alpha 1}$ peak of zirconium corresponds very closely to the M_{α} peak of gold. Since all samples were coated with gold, a small gold peak should always be observed, unless it has been obscured by a larger zirconium peak. Figure 83 shows an XRD pattern of a sample which was only 1 cm away from the sample which appeared in Figures 80-82. No alumina (or aluminum) was detected. The monoclinic (baddeleyite) form of zirconia was detected, however. It was suspected that the EDS did not penetrate the surface deeply and measured only aluminum while the XRD penetrated the surface layer of alumina and detected the underlying zirconia.

Emboldened by these results, the decision was made to try and form a true multi-layered coating. Eight layers (four zirconia, four alumina) were to be deposited in eight runs (each lasting two hours) with zirconia being the base layer and alumina being the top. Figure 83 shows an SEM micrograph and EDS scan of the alumina surface

layer. Large aluminum and oxygen peaks were taken to be alumina. The zirconium peak was assumed to have been due to the underlying zirconia deposition. No nickel peaks were observed, suggesting that the coating was dense enough to prevent the nickel substrate from being detected.

Immediately visible in Figure 84 was the surface along with a ghost-like image resting top. Individual SEM micrographs and EDS scans of these two areas appear in Figures 85 and 86, respectively. As with other deposits, the surface (Figure 85) consisted of small clumps (≈1.25 μm across). The EDS scan of the surface was virtually identical to that observed in Figure 84. The ghost-like image (Figure 86) was made up of extremely fine threads. The EDS scan detected only aluminum and oxygen (along with the gold coating applied to prevent charging). This suggested that this portion of the deposition was pure alumina. It was hypothesized that the powder formation so prevalent in the formation of Al_2O_3 via CVD resulted in these sorts of fine, thread-like structures and that this powder formation was occurring in addition to the deposit which was being formed on the substrate. This, however, is only a suggestion as to what may actually be occurring.

One of the samples with the multi-layered coating was sectioned, mounted and polished. The cross section of the coating was studied to determine if, indeed, a multi-layered coating had been formed. SEM micrographs of the sectioned sample appear in Figures 87-92. Clearly visible in Figures 87 and 88 were what appeared to be a

true multi-layered coating. The coating appears to be dense and relatively uniform. Somewhat troubling was what appeared to be only six layers (three zirconia, three alumina). Figure 89, however, offers a possible explanation to the two missing layers. The entire coating was approximately 5 μm thick. A thicker coating would have been expected if only zirconia had been deposited. It is believed that surface layers were in the process of being stripped as a new layer was initially being deposited. Once the new layer became established, the preceding layer was protected and further degradation inhibited Figure 89 shows what appears to be a discontinuous first layer of alumina (second layer, overall). Where this layer has been stripped, the first and second layers of zirconia (first and third layers, overall) appear as one layer, resulting in what seems to be six layers. The far right of Figure 89 shows a thin, dark layer. This is believed to be the missing layer of alumina. When this is counted, the eight expected layers emerge. Further support for the concept of reactive layers appears in Figure 90. The far left of the micrograph shows what appears to be only a portion of the first alumina layer (second overall layer). Also visible in Figure 90 is a square step on the surface of the substrate. The deposit filled in this imperfection, neatly following its outline. The clean definition between the layers, however, became somewhat blurred within this notch. Figure 91 shows another example of the uniformity of the coating, despite surface imperfections.

Figure 92 shows a particularly uniform region of the multi-layered coating. Spot EDS scans were performed, as indicated in Figure 92, traversing from the nickel substrate into the epoxy mounting (numbered 1-10). These scans appear in Figures 93-102. The first three scans (Figures 93-95) were made on the nickel substrate and, as expected, show strong nickel peaks. The gold peaks were again due to the coating applied to the sample to prevent charging within the SEM. The zirconium and aluminum peaks which appear in the second scan are believed to be the result of smearing during polishing. The first layer deposited should have been zirconia. This fact was supported by the fourth scan (Figure 96), which was made squarely on the first layer. Strong zirconium and oxygen peaks were taken to be evidence of the expected zirconia layer. The next layer should be alumina. The fifth scan (Figure 97) was made on the second layer and detected a strong aluminum peak along with a large jump in oxygen, taken to be evidence of alumina. Zirconium was also detected. It was believed that the thinness of the alumina layer led to an overlap during the EDS scan, thus resulting in the zirconium peak. Also important is what did not appear in the fifth scan. The nickel peak had completely disappeared as the scan moved away from the substrate. Further EDS scans revealed a consistent pattern. Figure 98, made on the second zirconia layer, shows strong zirconium and oxygen peaks along with a greatly diminished aluminum peak. Figure 99 (second alumina layer) shows a rebound in the aluminum peak. Figure 100 (third zirconia layer) shows strong zirconium and oxygen peaks with no aluminum peak.

The final layer was alumina and the corresponding EDS scan (Figure 101) reveals robust aluminum and oxygen peaks with a diminished zirconium peak. Finally, the tenth EDS scan was made on the epoxy mounting and appear in Figure 102. Peaks indicating aluminum, zirconium and nickel were all absent. Only carbon, oxygen and gold were detected.

All of the EDS scans made of this multi-layered coating (Figures 93-101) showed some evidence of the presence of carbon. It was believed that this was due to smearing of the epoxy mounting. Also present were some peaks representing silicon. This was again taken to be contamination originating from the quartz tube within which the reaction had taken place.

CHAPTER 7

CONCLUSIONS

Concerning the deposition of zirconia, the chlorination of metallic zirconium appeared to provide the best precursor. This was especially true once the chlorinator had been modified to yield 100% chlorination. The $ZrCl_4$ had too much of a tendency to condense within the lines. This could be remedied by heating the lines more effectively, but the chlorination of zirconium is probably more cost effective in the long run.

The zirconium metalorganic did not seem to provide any advantages over the chloride precursor. Carbon contamination appeared to be a nagging problem even at elevated temperatures (1050 °C). Also, the $Zr(tmhd)_4$ was more expensive, difficult to work with, and resulted in coatings which were inferior to those produced from $ZrCl_4$ at a slower deposition rate.

The optimum temperature for the flow rates examined in this work appeared to be 950 °C. Higher temperatures produced poor coatings while lower temperatures yielded extremely low deposition rates.

From the limited work conducted here, the best method for increasing the rate of deposition was increasing the total flow of reactants to the substrate while maintaining the same composition. Here, that was accomplished by improving the chlorination efficiency and increasing flow rates of all the reactants involved by a factor of two. A

larger chlorinator with even higher flow rates may lead to even higher rates of deposition.

The increase in deposition rate with increased total flow of equivalent composition observed here had also seen by Sipp et al.[12] This suggests that the oxidation of $ZrCl_4$ is controlled by mass flow to some extent. It is suspected that at some increased total flow the reaction would reach a saturation point and deposition rates would cease to increase with increased total flow.

The ZrO_2 coatings that were produced by reacting chlorinated Zr with H_2 and CO_2 (P = 5 Torr, T = 950 °C) displayed a crystalline structure and good adherence. XRD revealed that the deposits were monoclinic (baddeleyite).

Deposits that consisted of alternating layers of ZrO_2 and Al_2O_3 were produced. Unfortunately, time did not permit including detailed analysis of these coatings in this thesis.

CHAPTER 8

SUGGESTED FUTURE WORK

The layered zirconia/alumina coating which was made during this work was not fully characterized. While XRD showed the ZrO_2 layers to be monoclinic, no such data was collected from the Al_2O_3 layers. These layered coatings should be examined using transmission electron microscopy (TEM) and microprobe analysis to more fully assess their makeup. In addition, thermal diffusivity tests would yield information to suggest whether the zirconia had been stabilized by the alumina and if such coatings would make suitable TBC's. Finally, thicker layered coatings should be produced using the automated capabilities of Reactor 2. Nano-indentation could then be conducted on each individual layer to determine its mechanical properties and gain some insight into bonding between layers. The layered coatings produced to date were too thin for such measurements.

While use of YCl_3 was not used in this work, it is believed that YSZ from chloride precursors would be the method of choice for CVD. If tests indicate that the layered zirconia was not stabilized, then perhaps a coating of alternating layers of YSZ and alumina could be made and examined.

LIST OF REFERENCES

LIST OF REFERENCES

1) Cover Story Ceramic Coatings American Ceramic Society Bulletin, Volume 71, No. 10, 1471-1481, October 1992

2) Herman, S., Shankar, N. R. Survivability of Thermal Barrier Coatings Materials Science and Engineering, 88, 69-74 (1987)

3) Unal, O., Mitchell, T. E., Heuer, A. H Microstructures of Y_2O_3-Stabilized ZrO_2-Electron Beam-Physical Vapor Deposition Coatings on Ni-Base Superalloys Journal of the American Ceramic Society, Vol. 77, No. 4, 984-992, April 1994

4) Miller, Robert A., Lowell, Carl. E. Failure Mechanisms of Thermal Barrier Coatings Exposed to Elevated Temperatures International Conference on Metallurgical Coatings and Process Technology (sponsored by the American Vacuum Society) San Diego, California, April 4-9, 1982

5) Lee, W. Y. Chemical Vapor Deposition of Thermal Barrier Coatings; Seed Money Proposal Oak Ridge National Laboratory, Metals and Ceramics Division, Oak Ridge, Tennessee

6) Rapp, R. A., Courtright, E. L., Martin, P. M. Advanced Coatings for Gas Turbine Blades (Pre-Proposal) Rapp: Dept. Materials Sciences & Engineering, The Ohio State University. Courtright and Martin: Advanced Materials Section, Pacific Northwest Laboratory

7) Wang, G. The Potential Advantages of PNL's Proposed Thin Multilayer Thermal Barrier Concepts Dept. Material Science & Engineering, The Ohio State University

8) Sherman, Arthur Chemical Vapor Deposition for Microelectronics: Principles, Technology, and Applications Noyes Publications, Park Ridge, New Jersey, copyright 1987

9) Goward, G. W., Cannon, C. N. Pack Cementation Coatings for Superalloys; A Review of History, Theory, and Practice Presented at the Gas Turbine Conference Exhibition, Anaheim, California, May 31 - June 4, 1967

10) Meier, Susan M., Gupta, Dinesh K., Sheffler, Keith D. Ceramic Thermal Barrier Coatings for Commercial Gas Turbine Engines JOM, 50-53, March 1991

11) Bennett, A. Rolls-Royce Experience with Thermal Barrier Coatings 1984 Rolls-Royce Ltd, 207-217

12) Sipp, Etienne, Langlais, Francis, and Naslain, Roger Kinetics of deposition of zirconia-based ceramics from $ZrCl_4$ H_2-CO_2-Ar gas mixture Journal of alloys and Compounds, 186, 65-76 (1992)

13) Brennfleck, K, Fitzer, E., Mack, G. Basic study of CVD of ZrO_2 Layers on Metal Substrates Institut für Chemische Technik, Universität, 7500 Karlsruhe, West Germany, 672-683

14) Duret, C., Pichoir, R. Protective Coatings for High Temperature Materials: Chemical Vapor Deposition and Pack Cementation Processes Office National d'Etudes et de Recherches Aérospatiales (ONERA), Chatillon, France, 33-78

15) Seshu B. Desu, Tian Shi, and Chi K. Kwok Structure, Composition, and Properties of MOCVD ZrO_2 Thin Films from *Chemical Vapor Deposition of Refractory Metals and Ceramics,* edited by T. M. Besmann and B. M. Gallois (Mat. Res. Soc. Symp. Proc. Vol. 168, 1990), 349-356

16) Cheol Seong Hwang and Hyeong Joon Kim Deposition and Characterization of ZrO_2 Thin Films on Silicon Substrate by MOCVD J. Mater. Res., Vol. 8, No. 6, June 1993, 1361-1367

17) Jie Si and Seshu B. Desu Metal-organic chemical vapor deposition of ZrO_2-films using $Zr(thd)_4$ as precursors J. Mater. Res., Vol. 9, No. 7, July 1994, 1721-1727

18) Jie Si, Chien H. Peng, and Seshu B. Desu Deposition and Characterization of Metalorganic Chemical Vapor Deposition ZrO_2 Thin Films using $Zr(thd)_4$ from *Chemical Vapor Deposition of Refractory Metals and Ceramics II,* edited by T. M. Besmann, B. M. Gallois, and J. W. Warren (Mat. Res. Soc. Symp. Proc. Vol. 250, 1992), 323-329

19) Sipp, E., Langlais, F., Naslain, R. CVD of Y_2O_3-CO_2-H_2-Ar gas mixtures: an experimental study Journal of Alloys and Compounds, 186, 77-87 (1992)

20) Dismukes, J. P., Kane, N. J. Chemical Vapor Deposition of Luminescent Films United States Patent #3,894,164, July 8, 1975

21) Varhue, W. J., Massimo, M., Carrulli, J. M., Baranauskas, V., Adams, E., Broitman, E. Deposition of Y_2O_3 by plasma enhanced organometallic chemical vapor deposition using an electron cyclotron resonance source J. Vac. Sci. Technol. A 11(4), 1870-1874, July/August 1993

22) Schoonman, J., Dekker, J. P., Broers, J. W. Electrochemical vapor deposition of stabilized zirconia and interconnection materials for solid oxide fuel cells Solid State Ionics 46, 299-308 (1991)

23) Pal, Uday B. Electrochemical vapor deposition of solid oxide films Solid State Ionics 52, 227-233 (1992)

24) Pal, U. B., Singhal, S.C. Electrochemical Vapor Deposition of Yttria-Stabiized Zirconia Films Journal of the Electrochemical Society, Vol 137, No. 9, 2937-2941, September 1990

25) Dekker, J. P., van Dieten, V. E. J., Schoonman The growth of electrochemical vapor deposited YSZ films Solid State Ionics 51, 143-145 (1992)

26) Carolan, Michael F., Michaels, James N. Growth Rates and Mechanism of Electrochemical Vapor Deposited Fims Solid State Ionics 37, 189-195 (1990)

27) McPherson, R., Houghton, M. E. Yttria-Partially Stabilized Zirconia Plasma-Sprayed Coatings Journal of the Australian Ceramic Society, Vol. 20, No. 2, 23-25 (1984)

28) Suhr, D. S., Mitchell, T. E., Keller, R. J. Microstructure and Durability of Zirconia Thermal Barrier Coatings Suhr and Mitchell: Case Western Reserve University, Department of Metallurgy and Materials Science, Cleveland, OH 44106. Keller: TRW Inc., Materials and Manufacturing Technology Center, Cleveland, OH 44117

29) Bratton, R. J., Lau, S. K., Lee, S. Y. Evaluation of Present-day Thermal Barrier Coatings for Industrial/Utility Applications Thin Solid Films, 73, 429-437 (1980)

30) Carolan, Michael F., Michaels, James N. Chemical Vapor Deposition of Yttria Stabilized Zirconia on Porous Supports Solid State Ionics 25, 207-216 (1987)

31) Yeckel, A., Middleman, S. Strategies for the Control of Deposition Uniformity in CVD - The Design of a Novel Wafer Carrier Journal of the Electrochemical Society, Vol. 137, No. 2, 207-212, January 1990

32) Yamane, H., Hirai, T. Yttria Stabilized Zirconia Transparent Films Prepared by Chemical Vapor Deposition Journal of Crystal Growth 94, 880-884 (1989)

33) Kim, E., Lee, J., Lee, S., Yoon, S. Characterization of Y_2O_3-Stabilized ZrO_2 Thin Films by Plasma-Enhanced Metallorganic Chemical Vapor Deposition Journal of The Electrochemical Society, Vol. 140, No. 9, 2625-2629, September 1993

34) Aleksandrov, V. I., Val'yano, G. E., Lukin, B. V., Osiko, V. V., Rautbort, A. E., Tatarinstev, V. M., Filatova, V. N. Structure of Single Crystals of Stabilized Zirconium Dioxide Izv. Akad. Nauk SSSR, Neorg Mater., 12 [2], 273-277 (1976)

35) Aleksandrov, V. I., Kitaeva, V. F., Osiko, V. V., Sobolev, N. N., Tartrintsev, V. M., Chistyi, I. L. Dependence of the Properties of a Single Crystal of the Solid Solution ZrO_2-Y_2O_3 on the Y_2O_3 Concentration Kratk. Soobsh. Fiz., [3], 21-27 (1975)

36) Ingel, R. P., Lewis, D. III Lattice Parameters and Density for Y_2O_3-Stabilized ZrO_2 Journal of the American Ceramic Society, 69 [4], 325-332 (1986)

37) Akiyama, Y., Sato, T., Imaishi, N., LPMOCVD of YSZ Thin Film - Experiments and Model Analysis from *Proceedings of the Twelfth International Symposium on Chemical Vapor Deposition, 1993*. Sponsored by The Electrochemical Society and edited by Klavis F. Jensen and G. W. Cullen. Proceedings Volume 93-2, 300-305

38) Pulver, M., Wahl, G., Scheytt, H., Sommer, M. Deposition of ZrO_2 and Y_2O_3-stabilized ZrO_2 from β-diketonates from *Proceedings of the Ninth European Conference on Chemical Vapour Deposition,* edited by Tapio Mäntylä, Journal De Physique IV, Colloque C3, supplément au Journal de Physique II, Volume 3, août 1993, 305-312

39) Schmaderer, F., Huber, R., Oetzmann, H., Wahl, G. CVD of High-T_c Superconductors from *Proceedings of the Seventh International Conference on Chemical Vapor Deposition, 1979.* Sponsored by the Electrochemical Society and edited by Thomas O. Sedgwick and Hans Lydtin. Proceedings Volume 79-3, 211-218.

40) Iikawa, A., Kuniya, Y. Extended Abstract of Spring Meeting of Japan Society of Applied Physics No. 3, 983 (1991)

41) Morrell, Paul & Taylor, Roy Thermal diffusivity of thermal barrier coatings of ZrO_2 stabilized with Y_2O_3. High Temperatures - High Pressures, volume 17, 79-88 (1985)

42) Youngblood, G. E., Rice, R. W., Ingel, R. P. Thermal Diffusivity of Partially and Fully Stabilized (Yttria) Zirconia Single Crystals Journal of the American Ceramic Society, 71 [4] 255-260 (1988)

43) Bulmer, R. F., Taylor, R. Measurement by the flash method of thermal diffusivity in two-layer composite samples High Temperatures - High Pressures, volume 6, 491-497 (1974)

44) Brandon, J. R., Taylor, R. Thermal Properties of Ceria and Yttria Partially Stabilized Zirconia Thermal Barrier Coatings Surface and Coatings Technology, 39/40, 143-151 (1989)

45) Hasselman, J., Composite Materials, volume 12, 403 (1978)

46) Williams, R. K., Bates, J. B., Graves, R. S., McElroy, D. L., Weaver, F. J. Comparison of Thermal Conductivity Data for Partially Stabilized Zirconia with Values Derived from Thermal Diffusivity Results Reprinted form the International Journal of Thermophysics, Vol. 9, No. 4, July 1988, 587-598

47) Gitzhofer, Francois, Pawlowski, Lech, Lombard, Didier, Martin, Christian, Kaczmarek, Ryszard, Boulos, Maher The apparent thermal diffusivity and thermal contact resistance in plasma sprayed multicoatings High Temperatures-High Pressures, volume 17, 563-573 (1985)

48) Miller, R. A., Lowell, C. E. Failure Mechanisms of Thermal Barrier Coatings Exposed to Elevated Temperatures Thin Solid Films, 95, 265-273 (1982)

49) Sun, J. H., Chang, E., Chao, C. H., Cheng, M. J. The Spalling Modes and Degradation Mechanism of ZrO_2-8 wt.% Y_2O_3/CVD-Al_2O_3/Ni-22Cr-10Al-1Y Thermal-Barrier Coatings Oxidation of Metals, Vol. 40, Nos. 5, 6, 465-481 (1993)

50) Stecura, Stephan Two-Layer Thermal Barrier Coatings I: Effects of Composition and Temperature on Oxidation Behavior and Failure Thin Solid Films, 182, 121-139, (1989)

51) Bryant, W. A. Review: The fundamentals of chemical vapor deposition Westinghouse Research and Development Center, Pittsburgh, Pennsylvania, Journal of Materials Science, 12, 1285-1306 (1977)

52) Skandan, G., Hahn, H., Kear, B. H., Roddy, M., Cannon, W. R. Processing of Nanostructured Zirconia Ceramics Materials Research Society, Symposium Proceedings, Vol. 351, 207-212 (1994)

53) Balog, M., Schieber, M., Michman, M., Patai, S. The Characteristics of Growth of Films of Zirconium and Hafnium Oxides (ZrO_2, HfO_2) by Thermal Decomposition of Zirconium and Hafnium β-Diketonate Complexes in the Presence and Absence of Oxygen Journal of the Electrochemical Society, Vol. 126, No. 5, 1203-12097 (1979)

APPENDIX

FIGURES

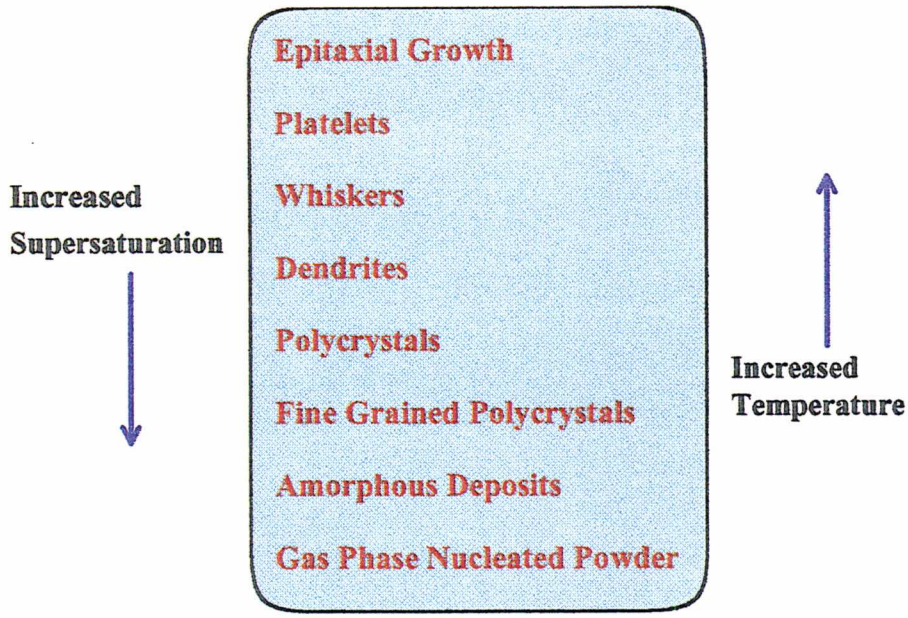

Figure 1: The effects of supersaturation and temperature on the structure formed by chemical vapor deposition. (Reproduced from "Protective Coatings for High Temperature Materials: Chemical Vapor Deposition and Pack Cementation Processes" by Duret and Pichoir[11]).

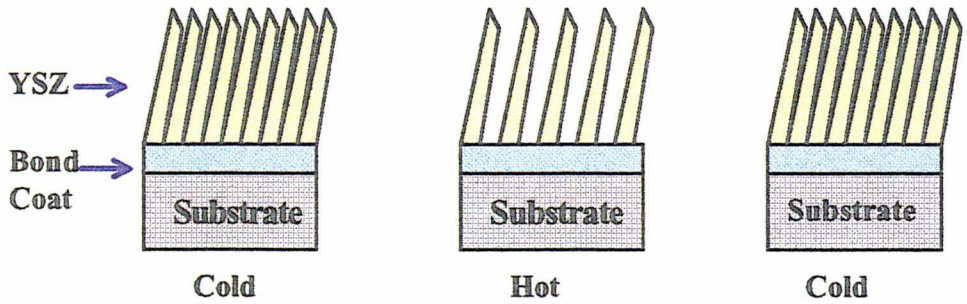

Figure 2: Schematic of column separation during thermal expansion.

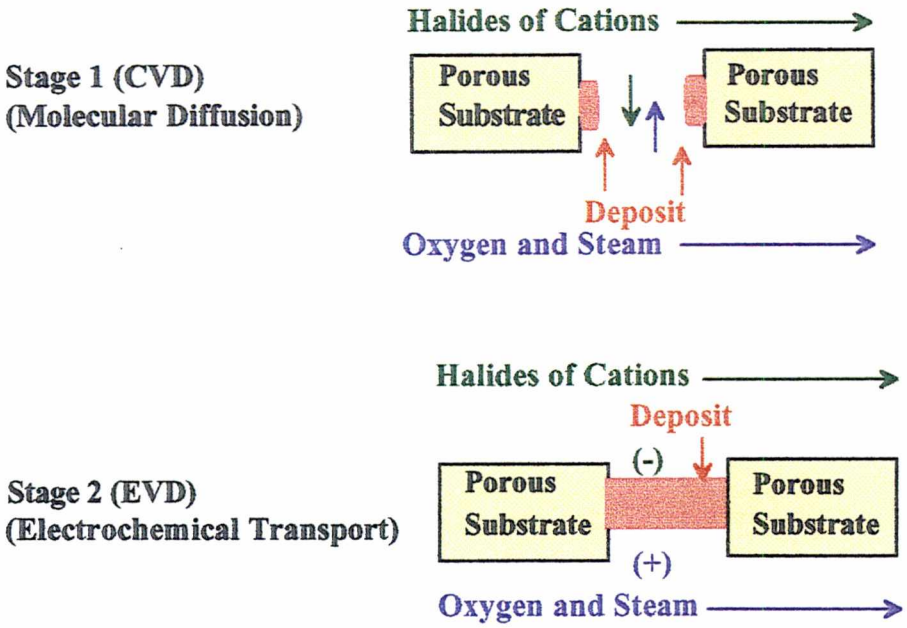

Figure 3: Schematic diagram of electrochemical vapor deposition (EVD).

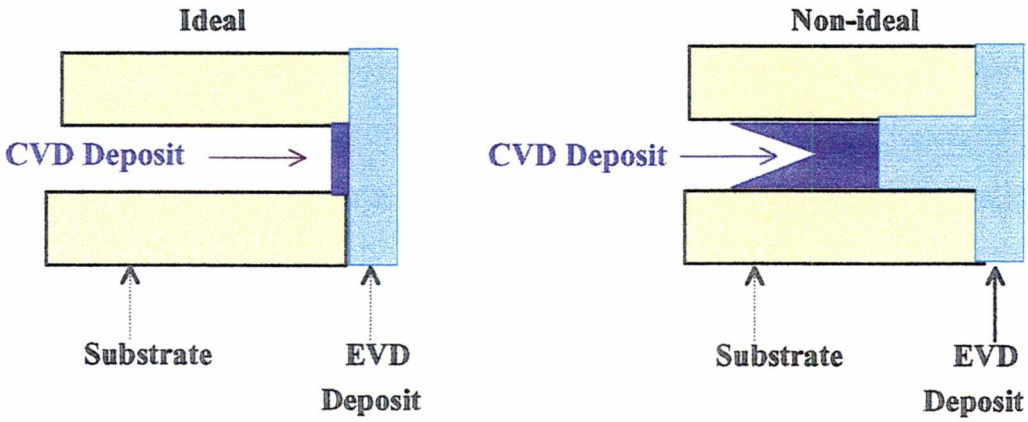

Figure 4: Comparison of ideal vs. non-ideal YSZ deposition during CVD phase of EVD process.

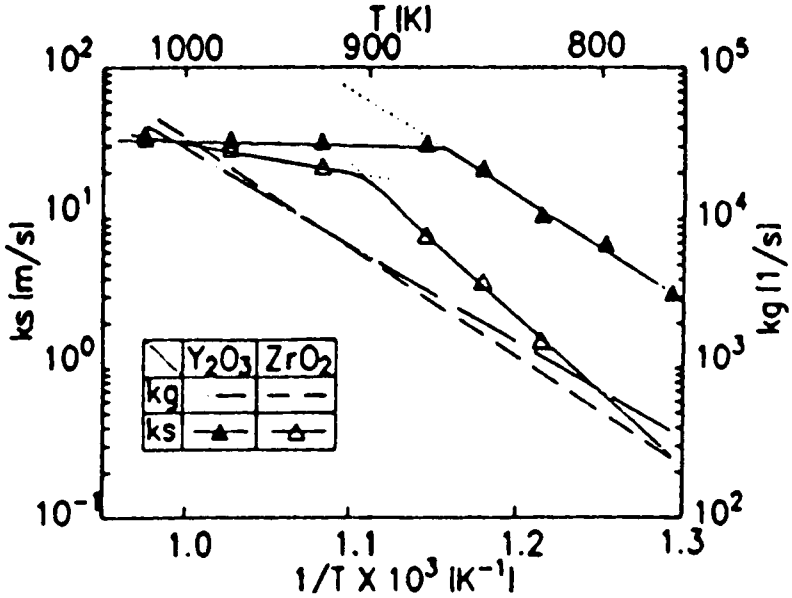

Figure 5: Arrhenius plots of gas-phase and surface reaction rate constants of ZrO_2 and Y_2O_3 (Reproduced from "LPMOCVD of YSZ Thin Film - Experiments and Model Analysis" by Akiyama et al.[29]).

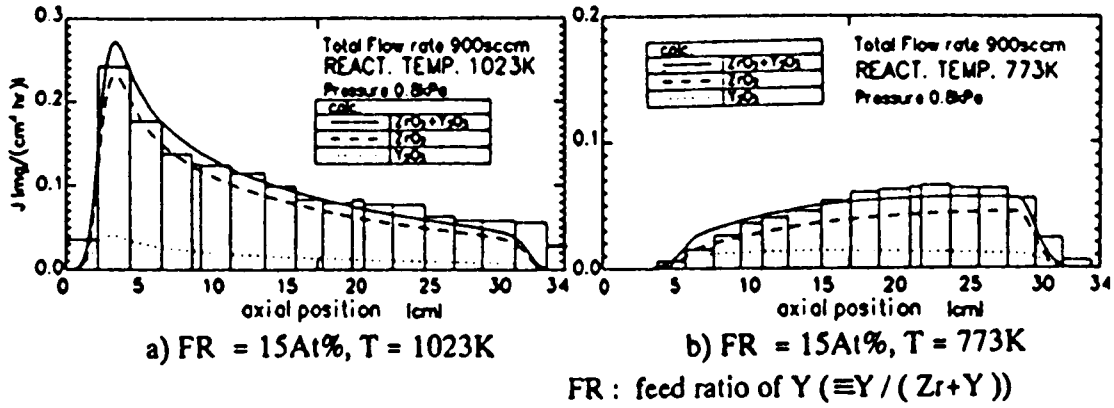

Figure 6: Growth rate distributions as determined by Akiyama et al.[29] (Reproduced from "LPMOCVD of YSZ Thin Film - Experiments and Model Analysis" by Akiyama et al.[29]).

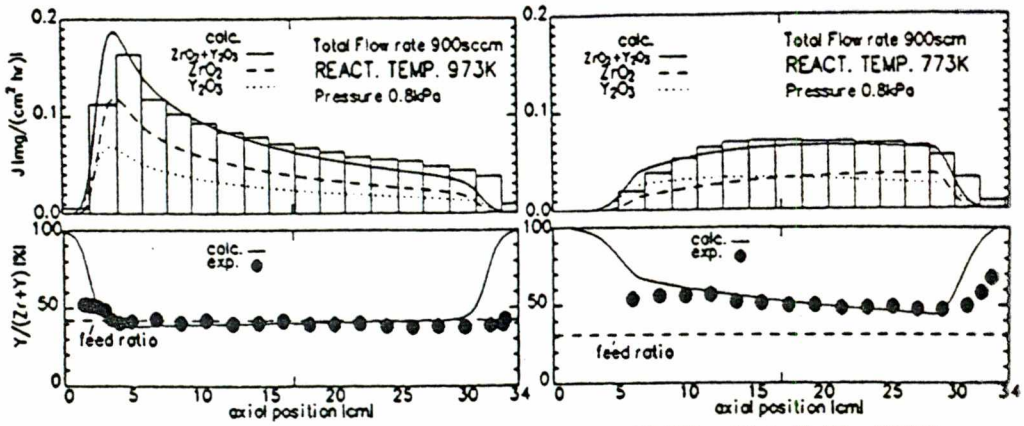

a) FR = 42At%, T = 973K b) FR = 31At%, T = 773K

Figure 7: Growth rate and yttrium composition distributions as determined by Akiyama et al.[29] (Reproduced from "LPMOCVD of YSZ Thin Film - Experiments and Model Analysis" by Akiyama et al.[29]).

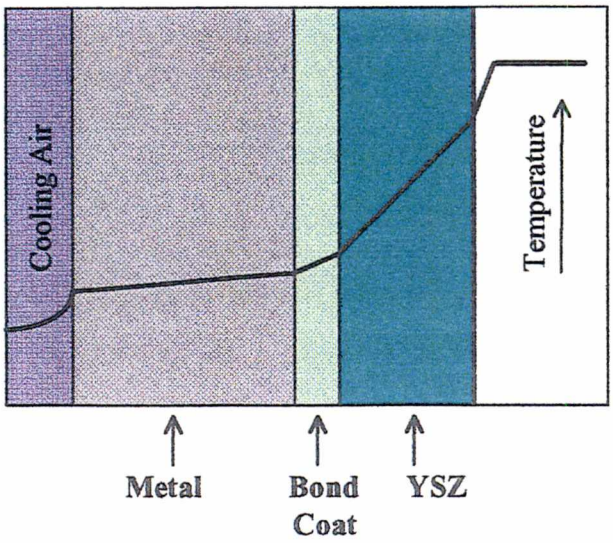

Figure 8: Schematic diagram of temperature profile of turbine blade with TBC and bond coat. (Reproduced from "Thermal diffusivity of thermal barrier coatings of ZrO_2 stabilized with Y_2O_3" by Morrell and Taylor[31]).

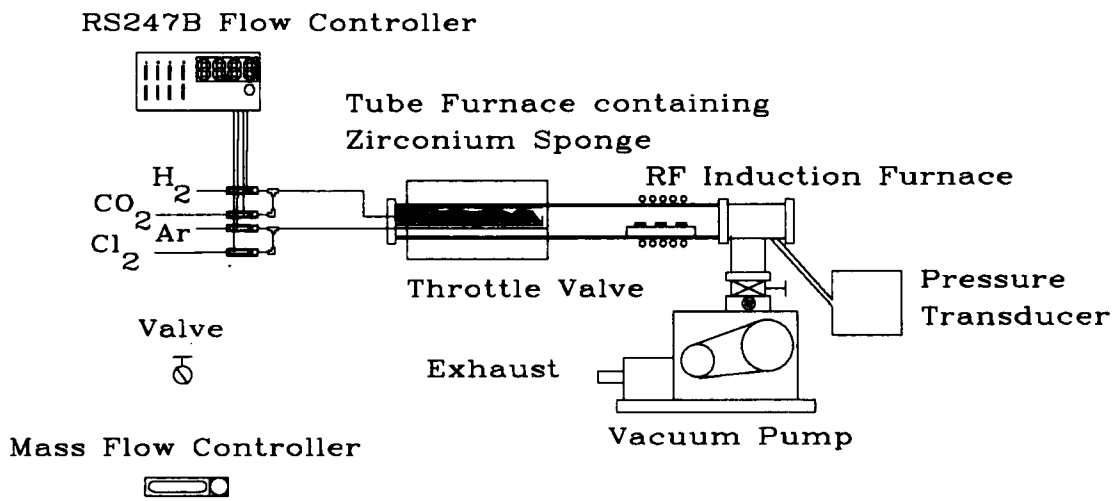

Figure 9: Schematic diagram of first CVD reactor. Zirconium sponge was chlorinated within a tube furn. Argon was used to transport the zirconium tetrachloride to the deposition region where it was reacted with carbon dioxide and hydrogen to form a zirconia deposition.

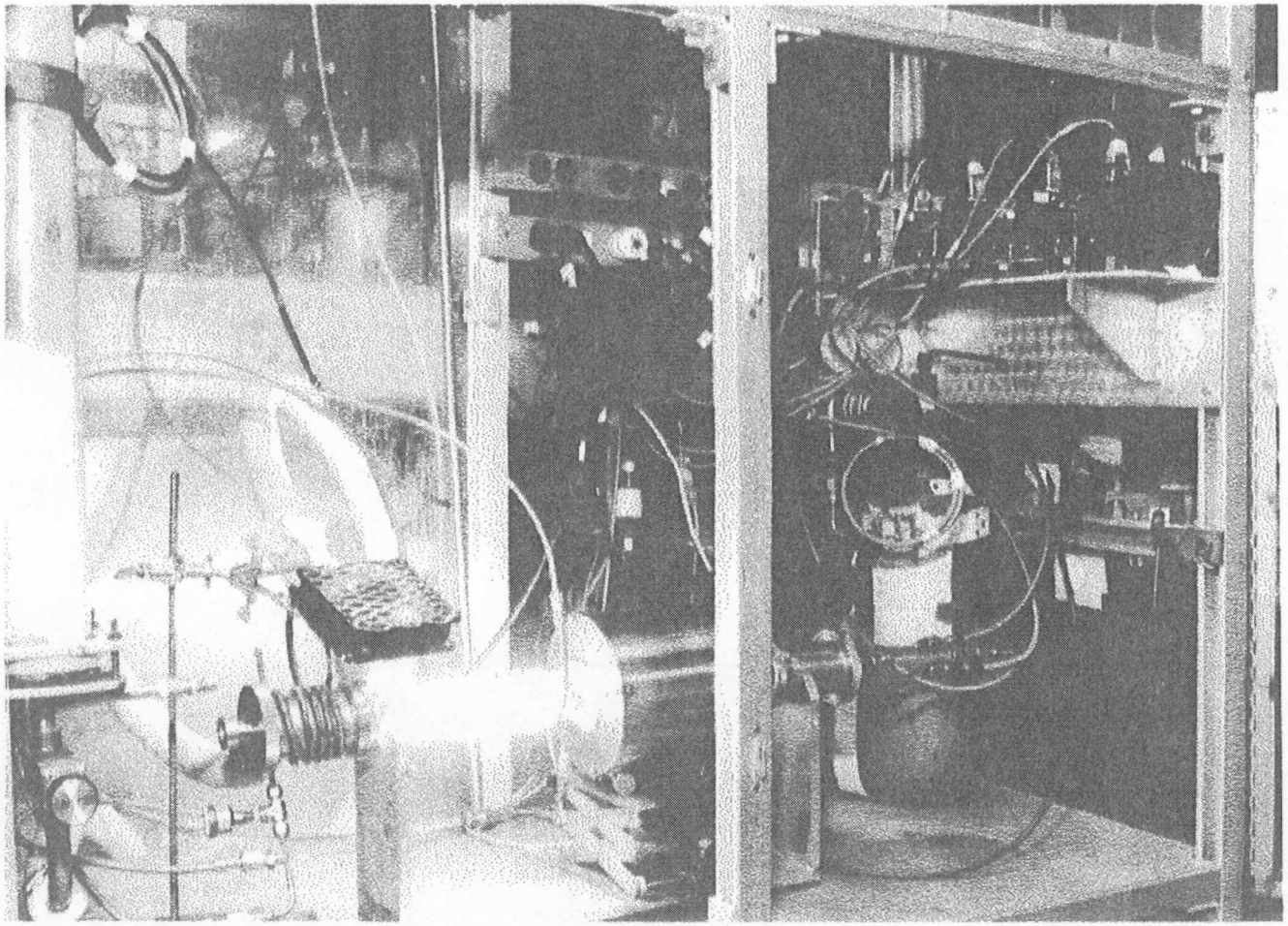

Figure 10: Photograph of first CVD reactor.

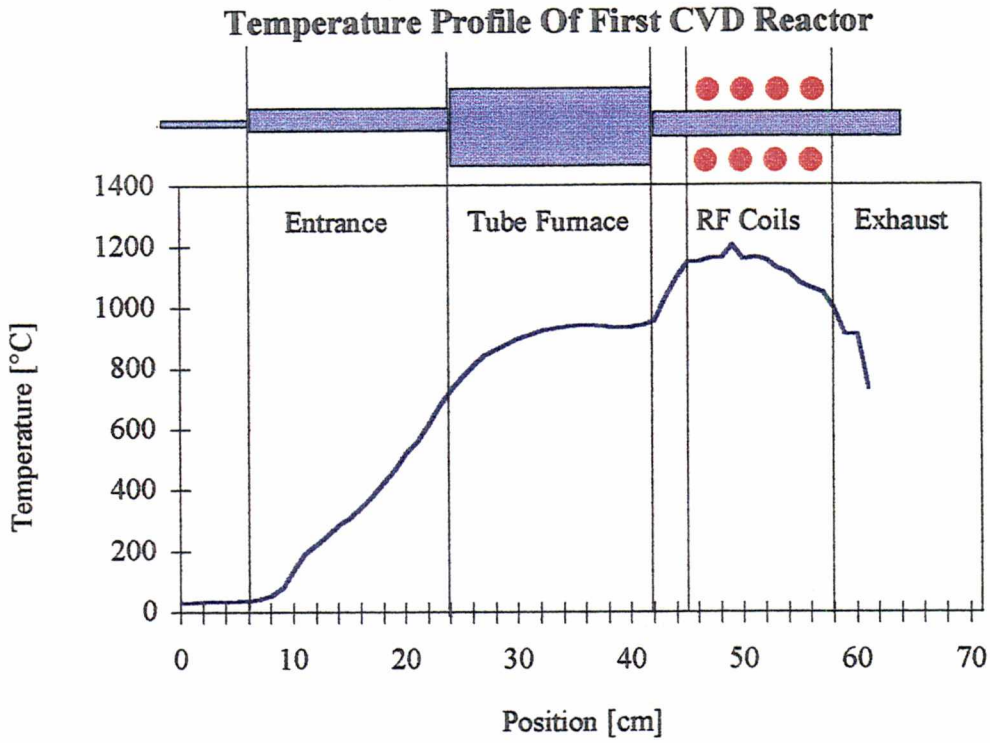

Figure 11: Temperature profile of first CVD reactor used for the deposition of zirconia from $ZrCl_4$.

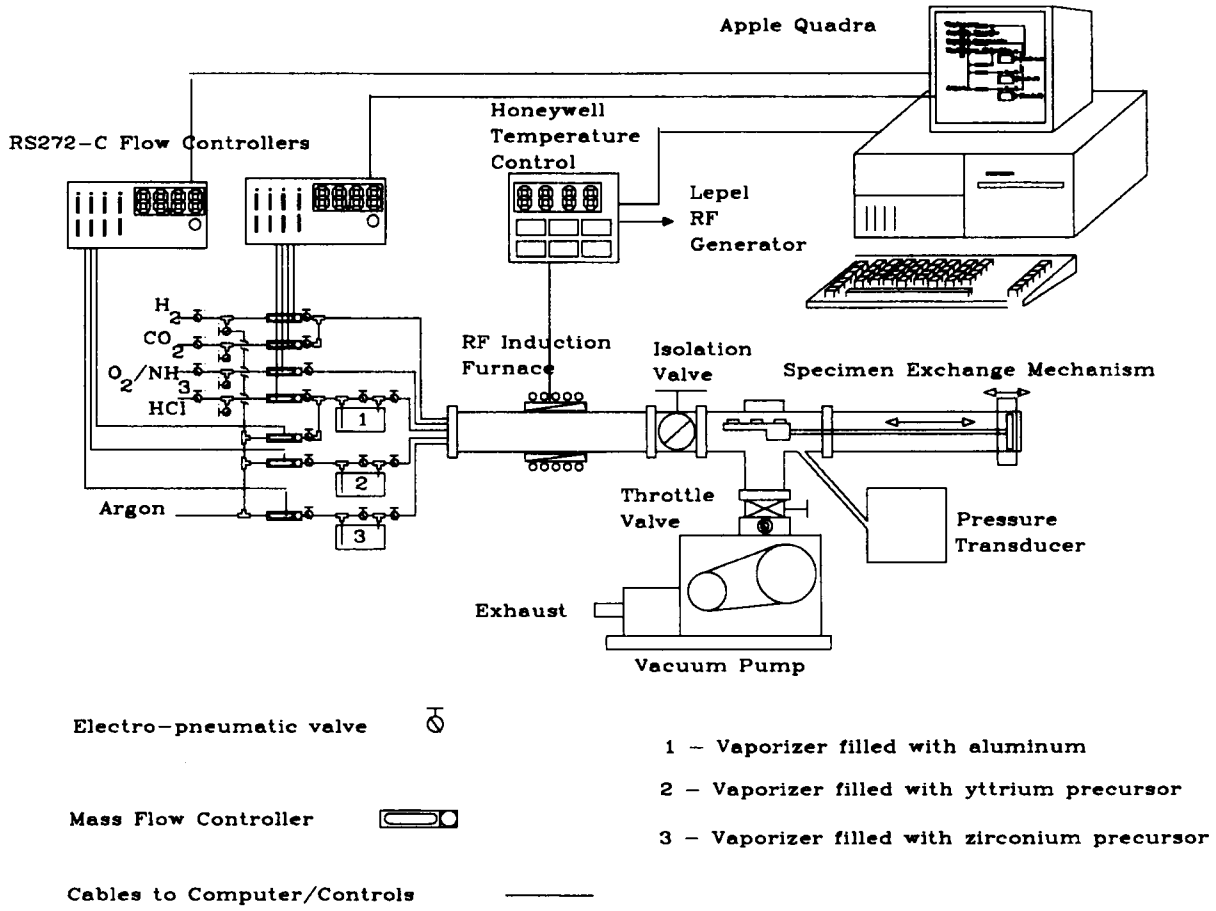

Figure 12: Schematic diagram of second CVD reactor constructed for the deposition of zirconia, yttria-stabilized zirconia, nickel aluminide and alumina.

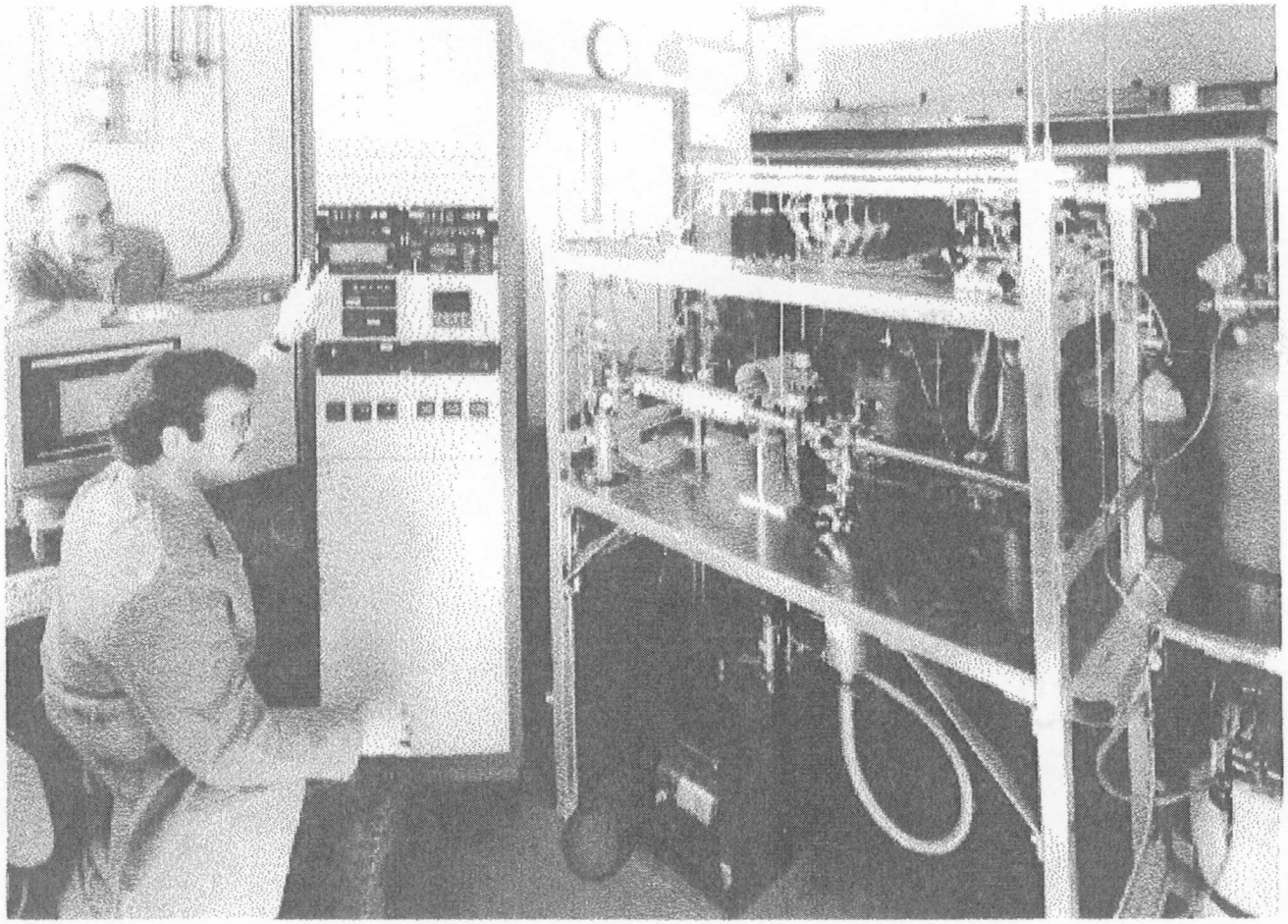

Figure 13: Photograph of second CVD reactor constructed for the deposition of zirconia, yttria-stabilized zirconia, nickel aluminide and alumina.

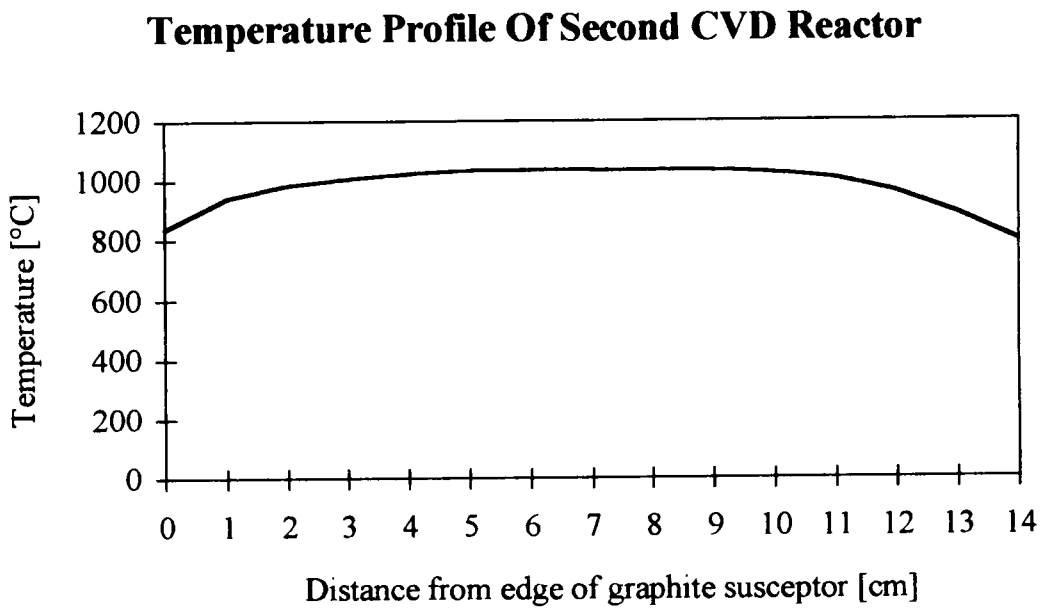

Figure 14: Temperature profile of second CVD reactor used for the deposition of zirconia, yttria and yttria-stabilized zirconia from $Zr(tmhd)_4$ and $Y(tmhd)_3$.

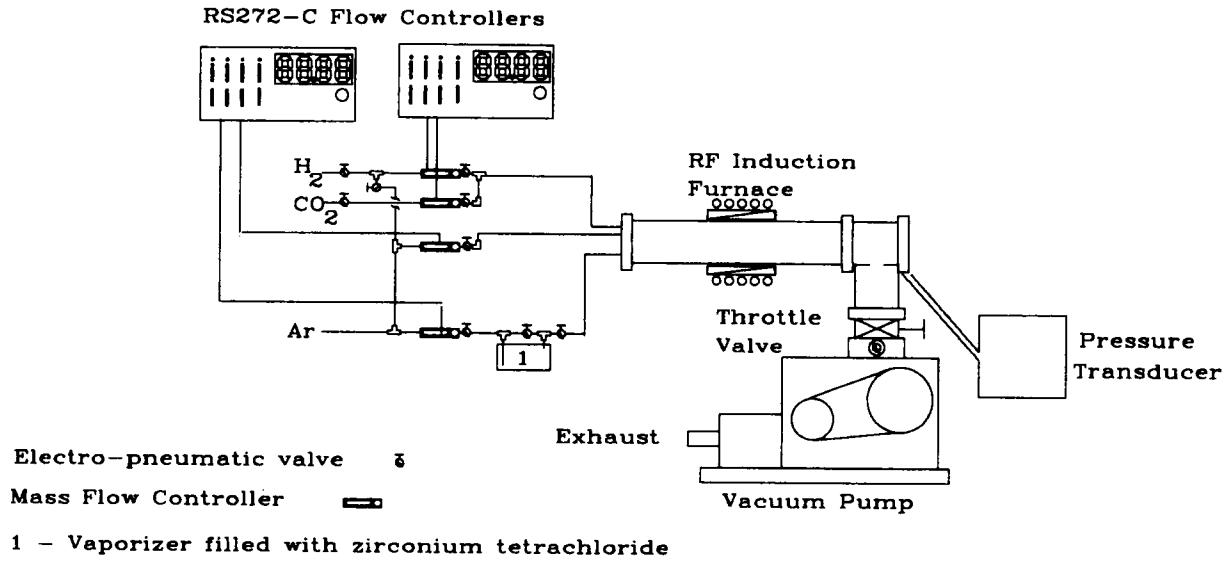

Figure 15: Schematic diagram of third CVD reactor. This was used in the deposition of zirconia from vaporized zirconium tetrachloride.

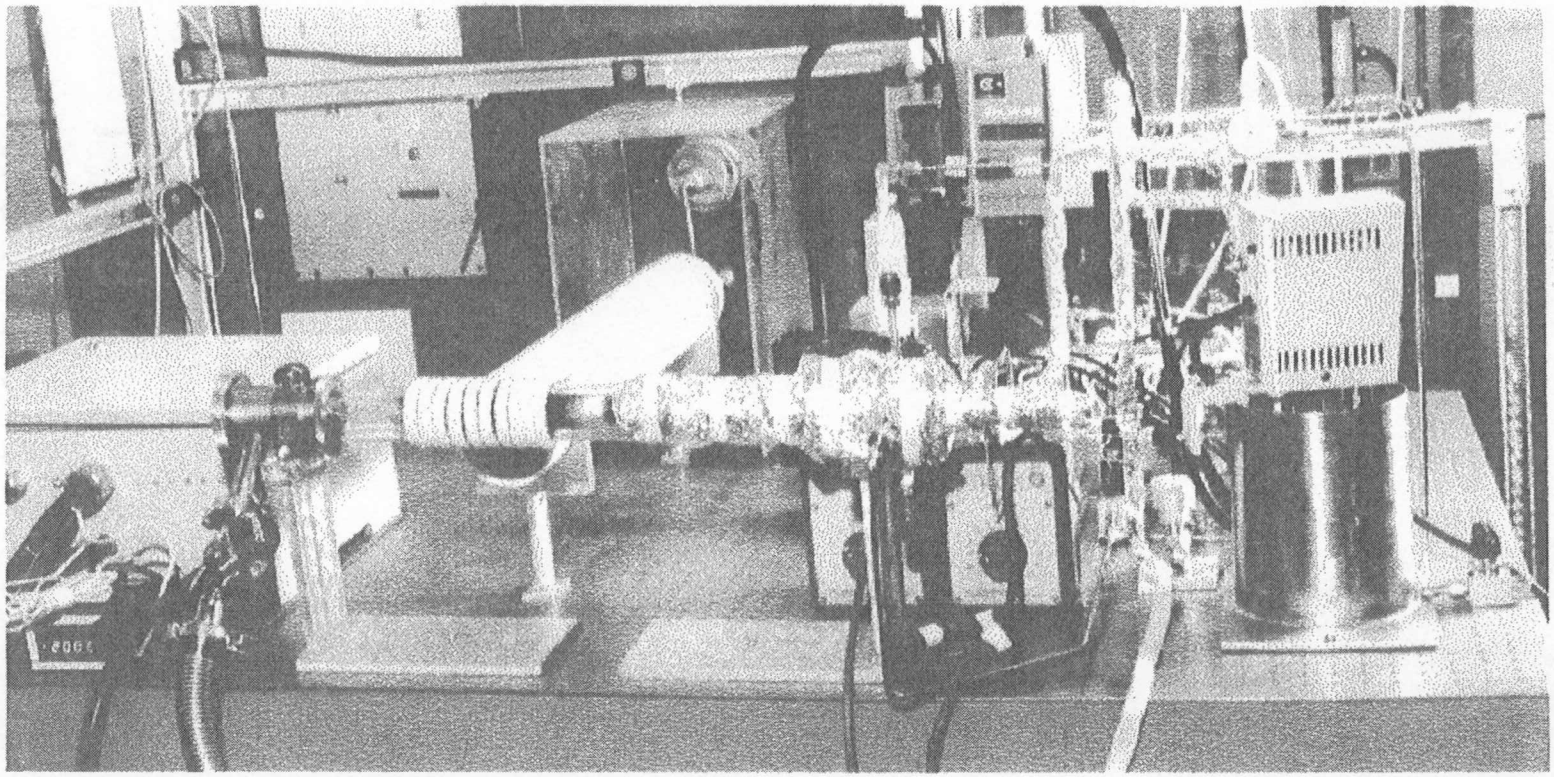

Figure 16: Photograph of third CVD reactor used for the deposition of zirconia.

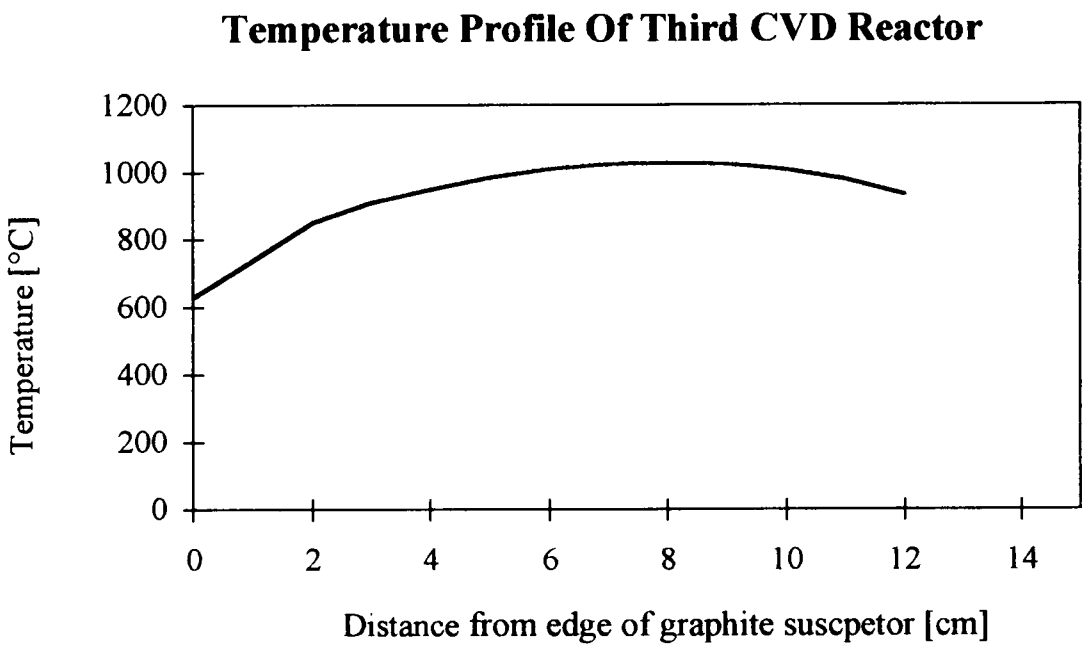

Figure 17: Temperature profile of third CVD reactor.

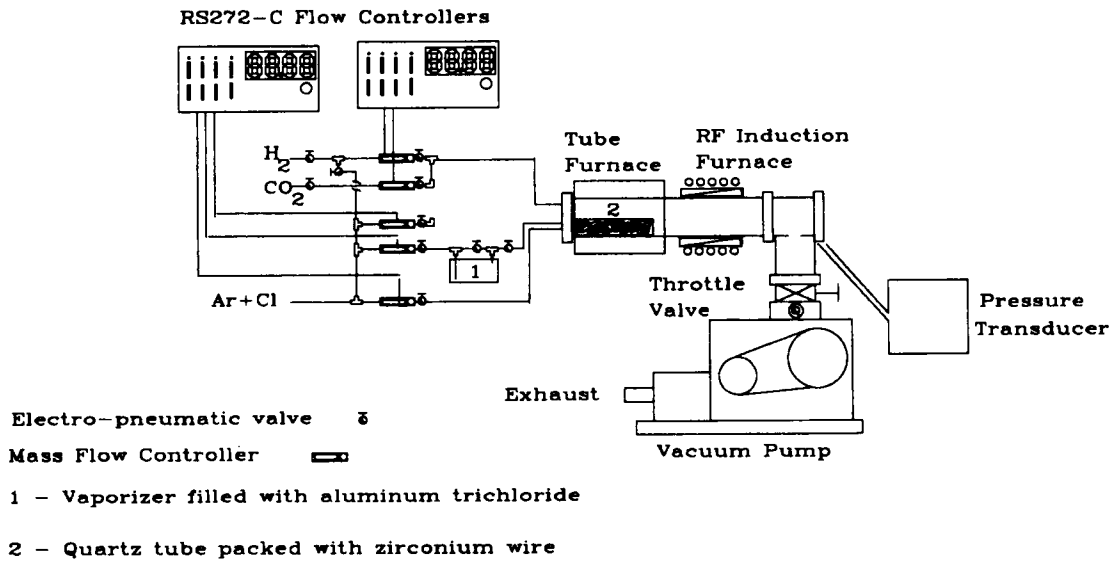

Figure 18: Schematic diagram of fourth CVD reactor. Chlorinated zirconium wire and aluminum trichloride were used as precursors in the attempt to form layered coatings.

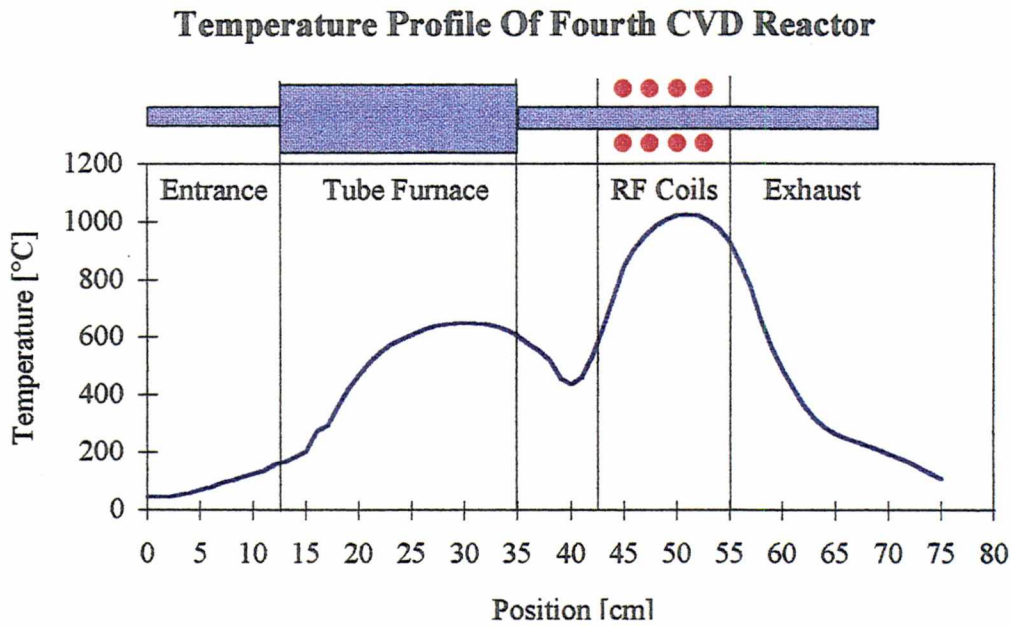

Figure 19: Temperature profile of fourth CVD reactor.

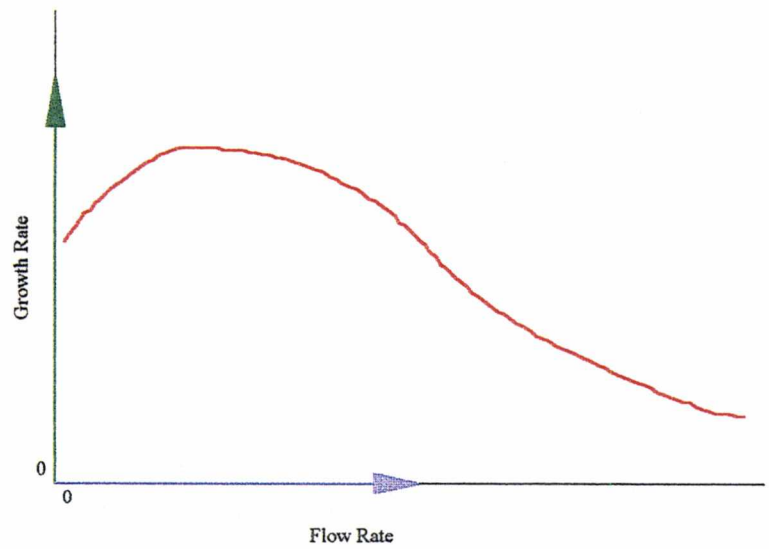

Figure 20: Theoretical depiction of relationship between growth rate and flow rate.

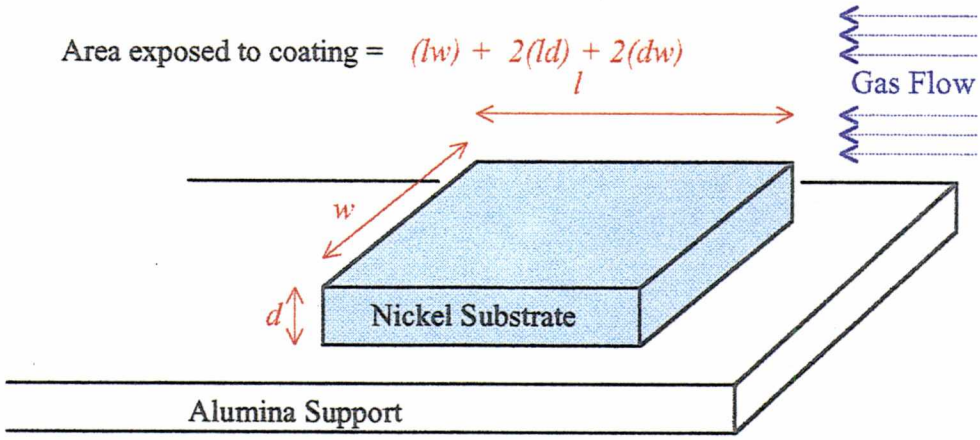

Figure 21: Schematic diagram showing possible coating surface.

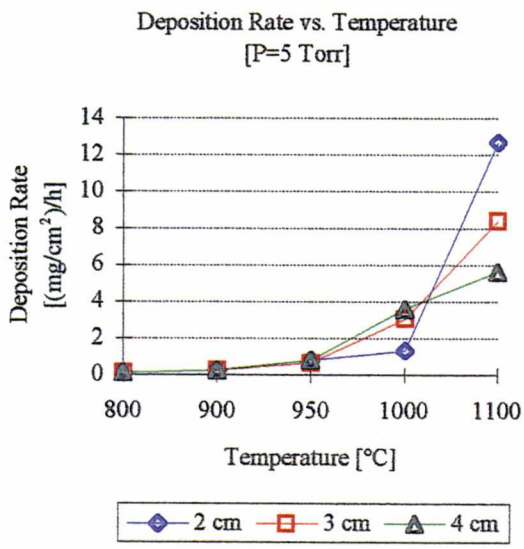

Figure 22: Rate of ZrO_2 deposition vs. temperature at P = 5 Torr.

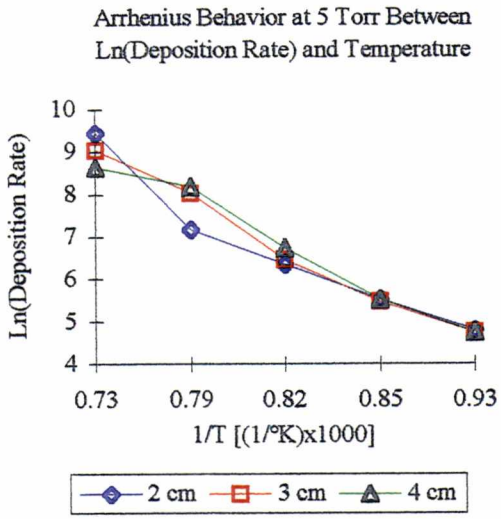

Figure 23: Arrhenius behavior between Ln(deposition rate) and temperature (P = 5 Torr).

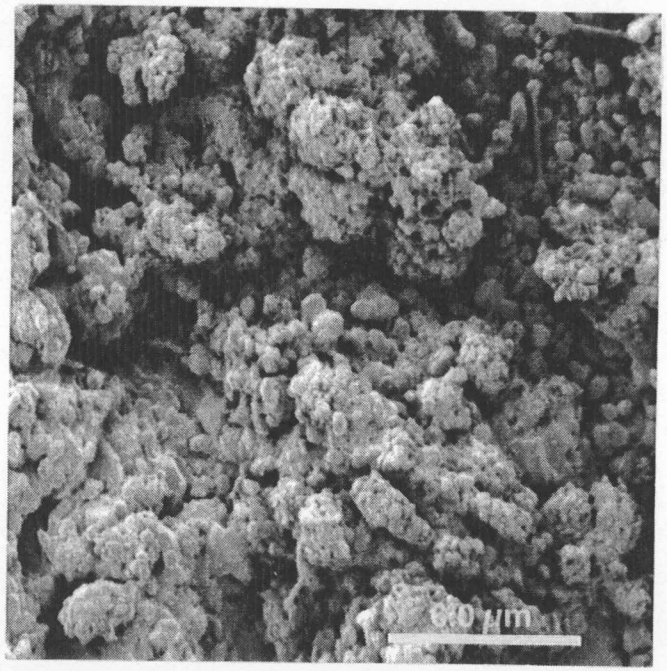

Figure 24: SEM micrograph of zirconia deposit made on nickel substrate at P = 5 Torr, T = 950 °C (5,000X). The deposition appears to have formed

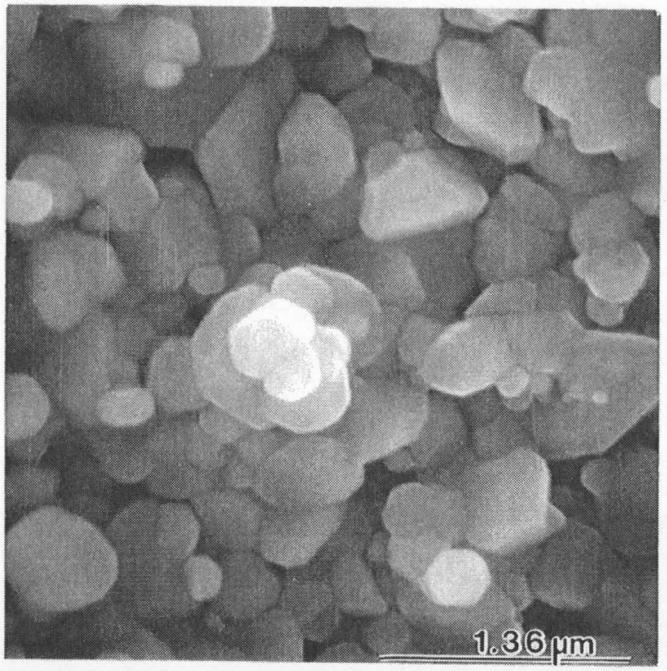

Figure 25: SEM micrograph of zirconia deposit made on nickel substrate at P = 5 Torr, T = 950 °C (22,000X). Note the fine grain structure which appears within the individual clumps.

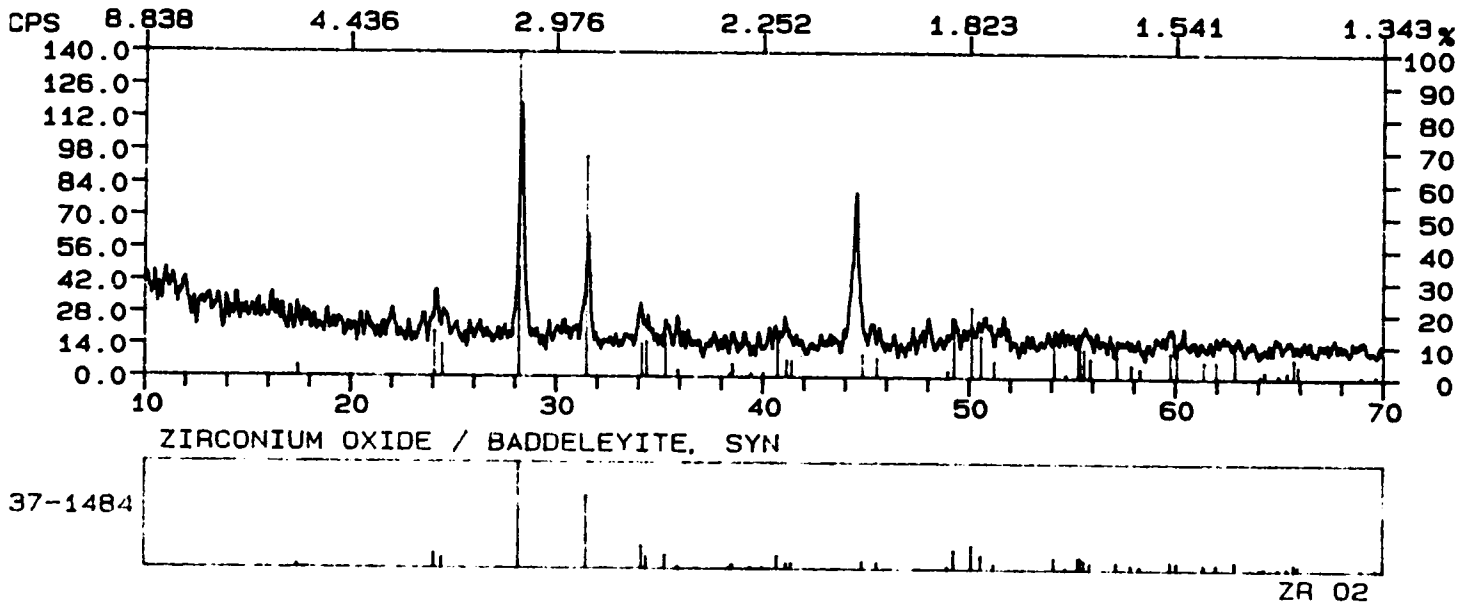

Figure 26: X-ray diffraction pattern of zirconia deposit made at a pressure of 5 Torr and a deposition temperature of 950°C. The coating was identified as baddeleyite (monoclinic) form. The strong peak just past 44 represents the

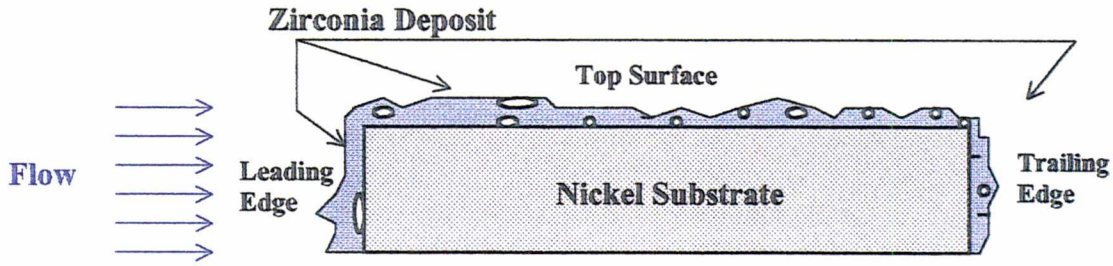

Figure 27: Schematic diagram of sectioned sample with ZrO_2 deposit made at P = 5 Torr, T = 950 °C. Micrographs of leading edge, top surface and trailing edge appear in Figures 28, 29 and 30.

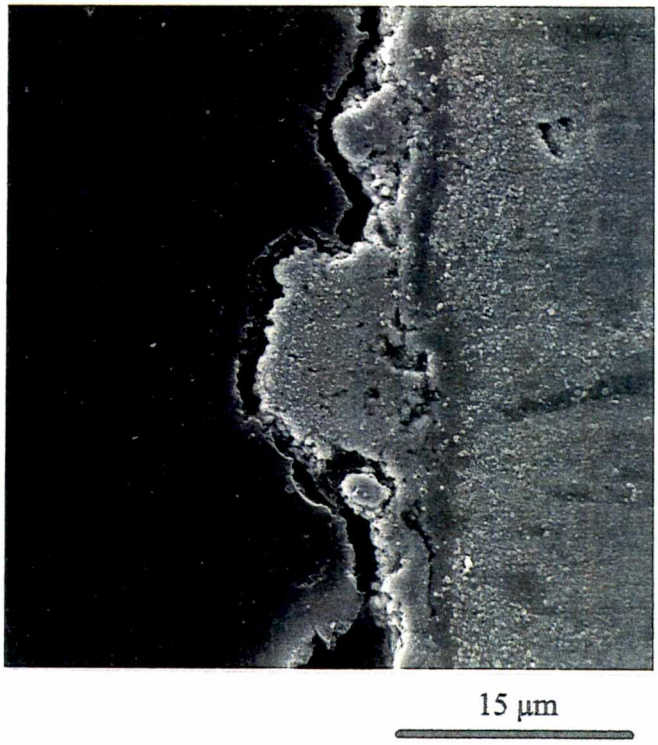

Figure 28: SEM micrograph of cross section of leading edge of ZrO_2 deposit made at P = 5 Torr, T = 950 °C (2,000X). Note unevenness of deposition layer.

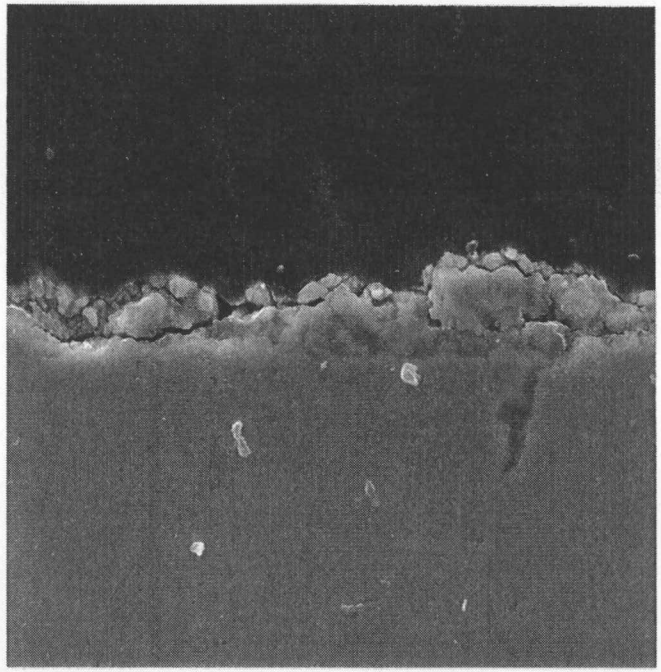

6 μm

Figure 29: SEM micrograph of top surface of zirconia deposit made at P = 5 Torr, T = 950 °C (5,000X). The coating is substantially thinner than that on the leading edge.

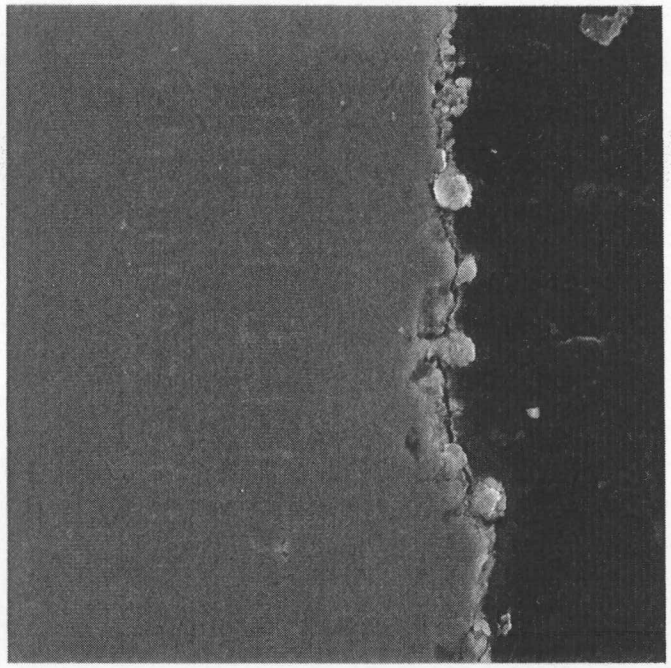

10 μm

Figure 30: SEM micrograph of trailing edge of zirconia deposit made at P = 5 Torr, T = 950 °C (3,000X). The coating is thinnest here.

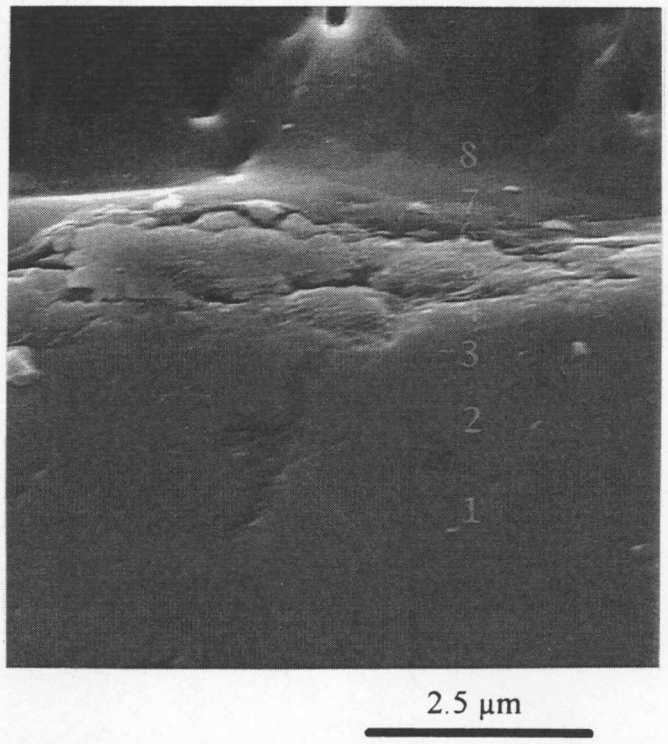

Figure 31: Cross section of top surface of zirconia deposit made at P = 5 Torr, T = 950 °C (12,000X). Spot EDS scans were made, traversing from the nickel substrate through the ZrO_2 coating and into the epoxy mold in which the sample was mounted. The numbers represent where scans were made and the corresponding results appear in Figures 32-39.

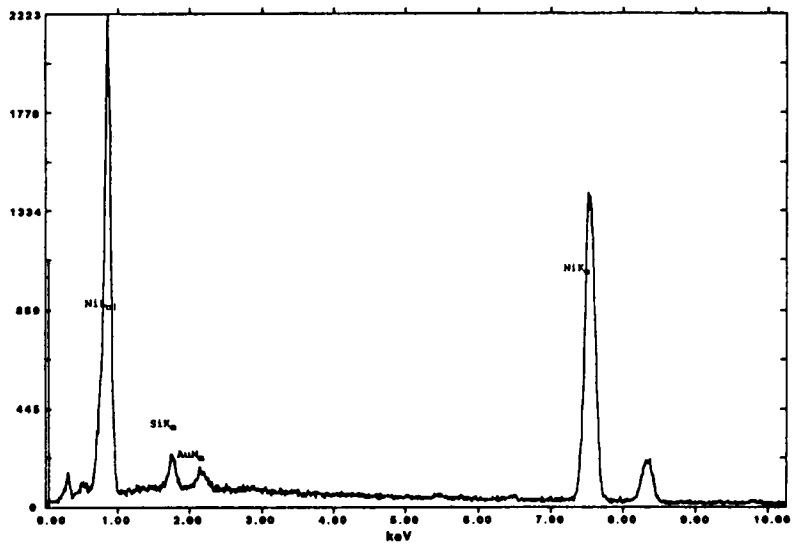

Figure 32: First EDS scan of SEM micrograph from Figure 31. Made squarely on the nickel substrate, this scan shows strong nickel peaks. The silicon peak was the result of contamination from the quartz tube. The gold peak was a result of the gold coating applied to prevent charging within the SEM.

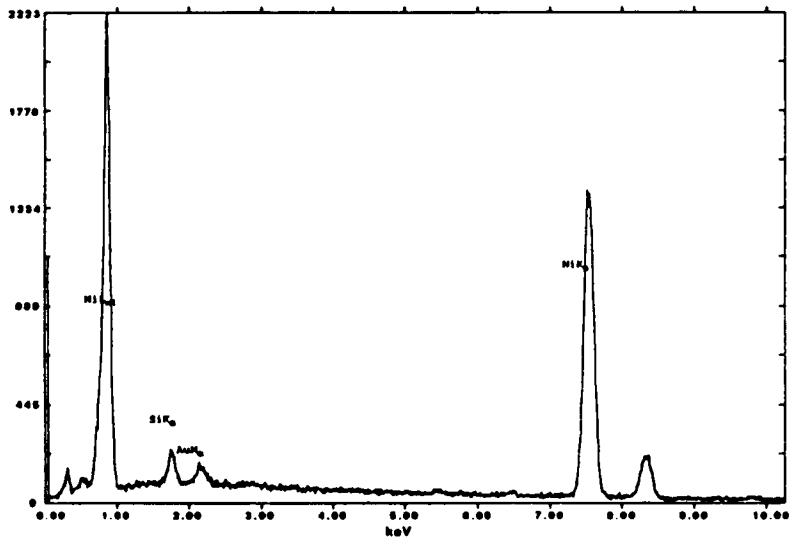

Figure 33: Second EDS scan of SEM micrograph from Figure 31. Made squarely on the nickel substrate, this scan shows strong nickel peaks. The silicon peak resulted from contamination from the quartz tube while the gold peak is a result of the gold coating applied to prevent charging within the SEM.

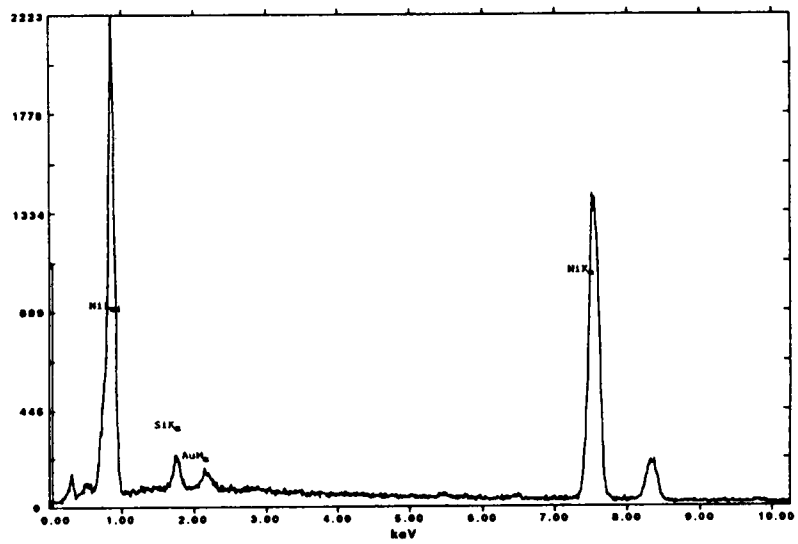

Figure 34 Third EDS scan of SEM micrograph from Figure 31. Made squarely on the nickel substrate, this scan shows strong nickel peaks. The silicon peak was the result of contamination from the quartz tube. The gold peak is a result of the gold coating applied to prevent charging within the SEM.

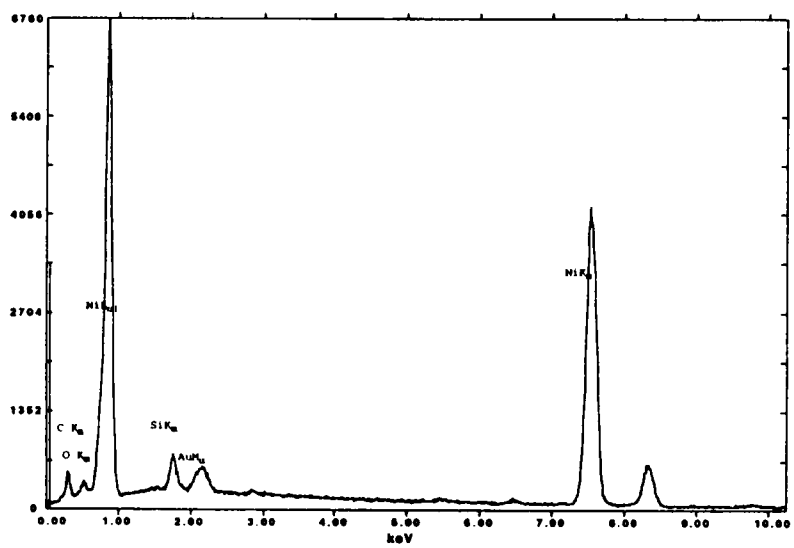

Figure 35: Fourth EDS scan of SEM micrograph from Figure 31. Made squarely on the nickel substrate, this scan shows strong nickel peaks. The silicon and gold peaks were contaminants.

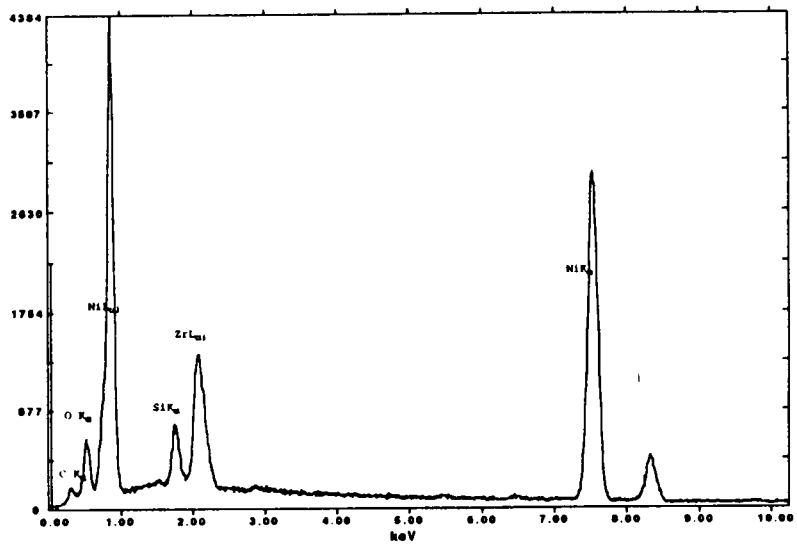

Figure 36: Fifth EDS scan of SEM micrograph from Figure 31. Made on the zirconia deposit, this scan revealed strong zirconium and oxygen peaks (taken to be ZrO_2). Nickel, silicon and carbon peaks continue to be present. The gold peak has been obscured by the zirconium peak.

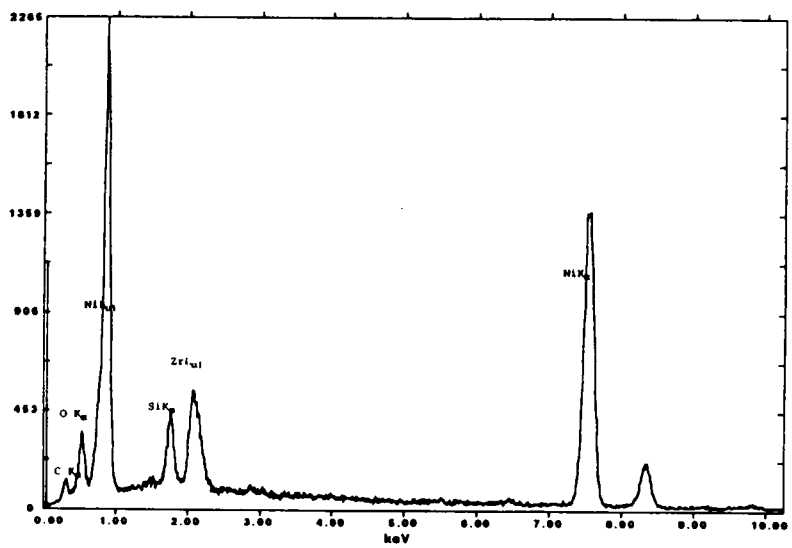

Figure 37: Sixth EDS scan of SEM micrograph from Figure 31. Made on the zirconia deposit, this scan shows strong zirconium and oxygen peaks (take to be ZrO_2). Nickel, silicon and carbon peaks continue to be present. The gold peak has been obscured by the zirconium peak.

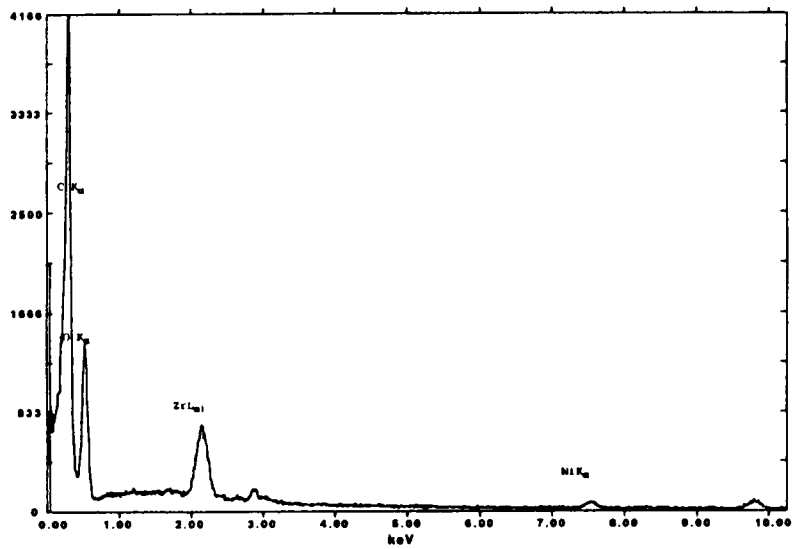

Figure 38: Seventh EDS scan of SEM micrograph from Figure 31. Made on the squarely on the zirconia deposit, this scan shows strong zirconium and oxygen peaks (taken to be ZrO_2). Nickel and silicon peaks are largely diminished. The carbon peak has increased in intensity as the epoxy mount is approached.

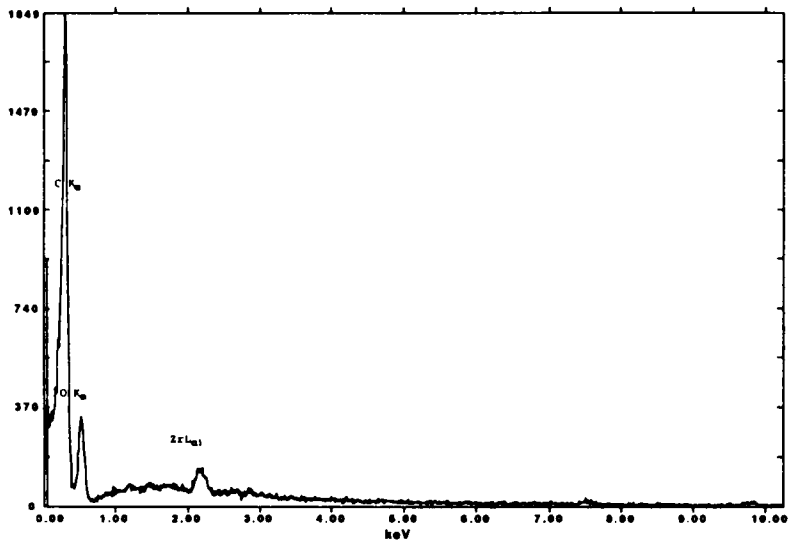

Figure 39: Eighth EDS scan of SEM micrograph from Figure 31. Made on the epoxy resin mounting, the carbon peak is predominant with lesser peaks of zirconium and oxygen. Nickel and silicon are completely absent.

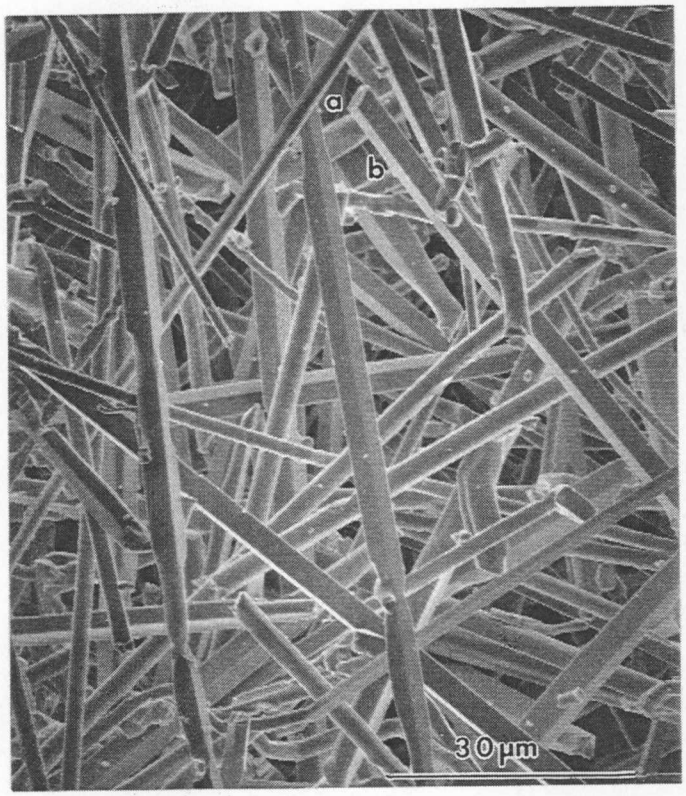

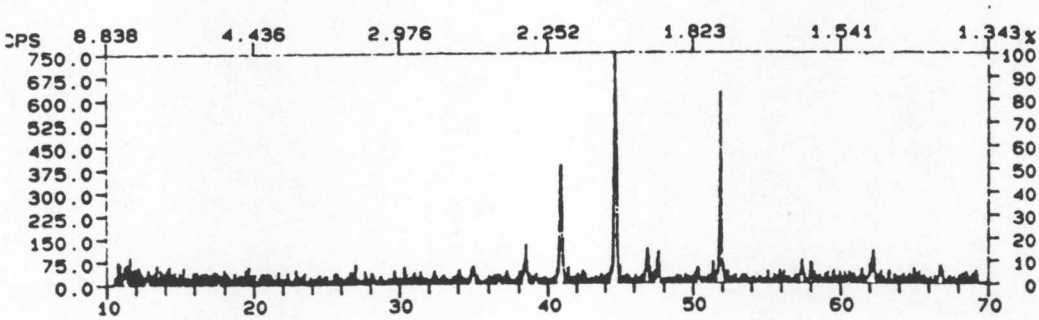

Figure 40: SEM micrograph and XRD pattern of ZrO_2 deposited at P = 5 Torr, T = 1100 °C (1,000X). Note the rectangular end (a) and the contrast which appears between the sides (b). This was a highly crystalline deposition that was believed to be monoclinic.

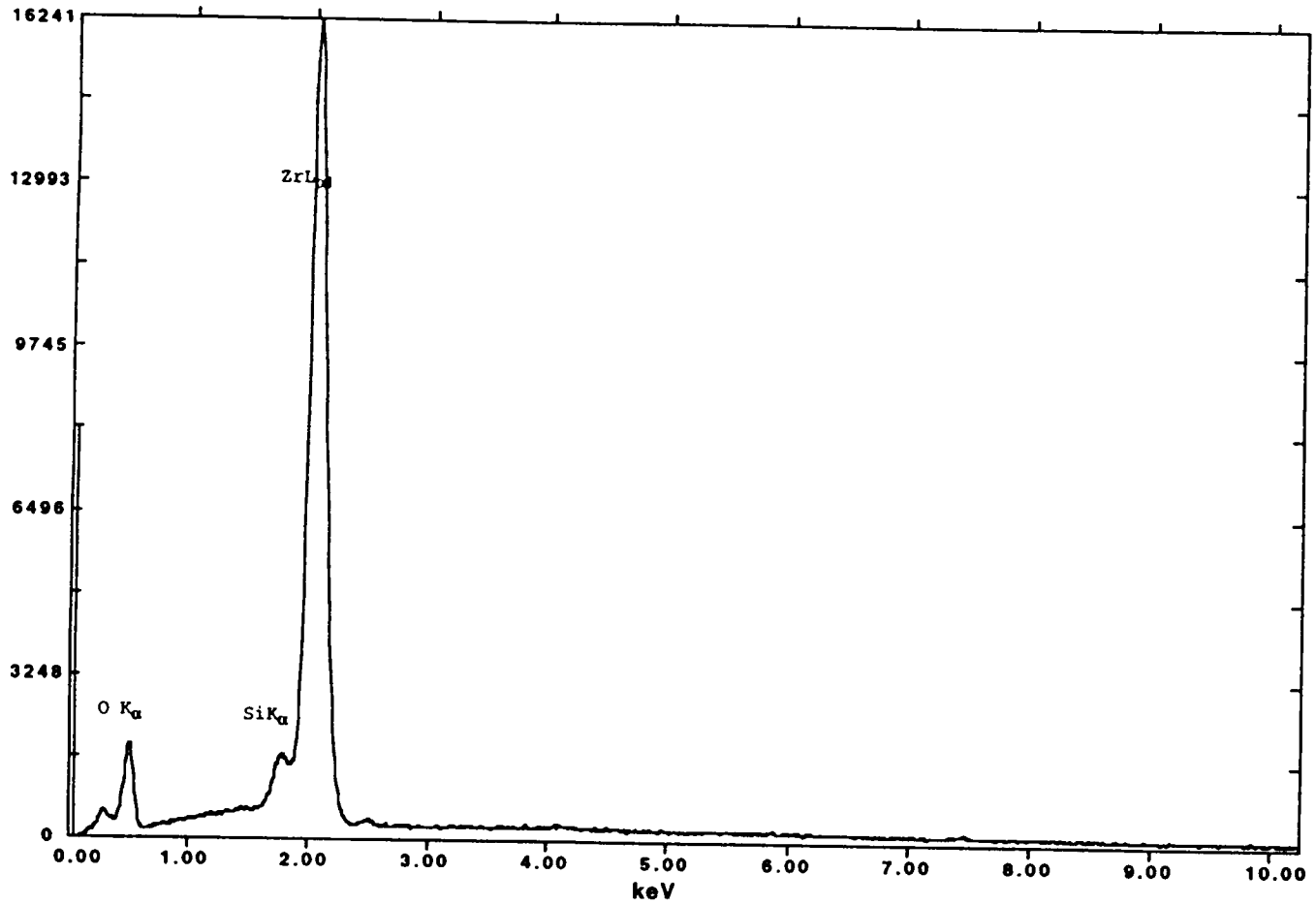

Figure 41: EDS scan of deposit made at P = 5 Torr, T = 1100 °C. While no zirconia match was found using XRD, the large zircoium peak coupled with the oxygen peak most likely indicates some form of zirconia, possibly a stoichiometric variation.

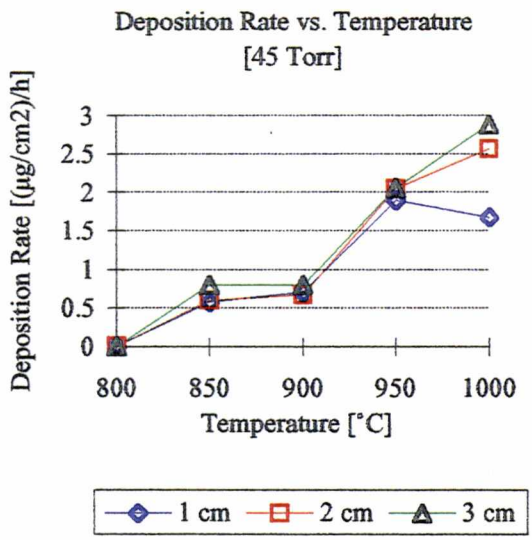

Figure 42: Rate of ZrO_2 deposition vs. temperature at P = 45 Torr

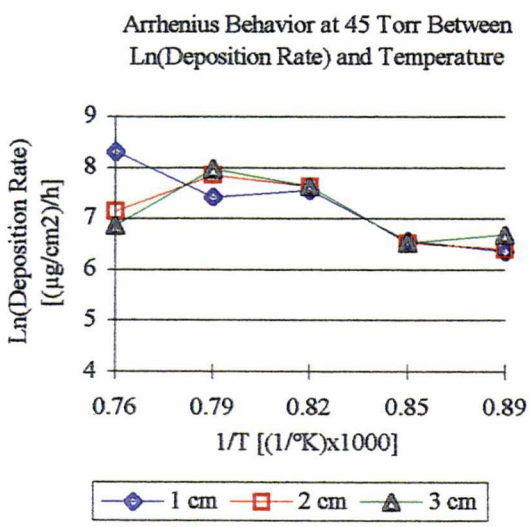

Figure 43: Non-Arrhenius behavior of deposition rate at P = 45 Torr.

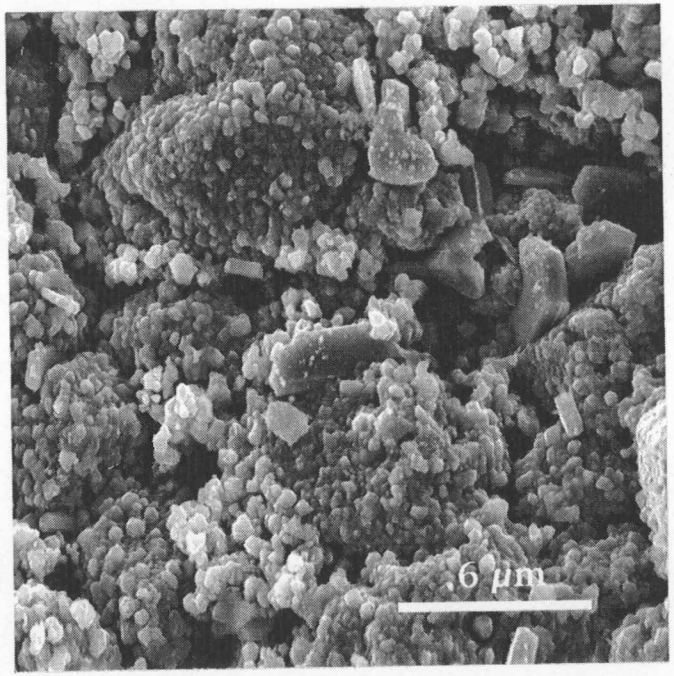

Figure 44: SEM micrograph of zirconia deposit on nickel substrate made at P = 45 Torr, T = 950 °C (5,000X). Note platelet like crystals.

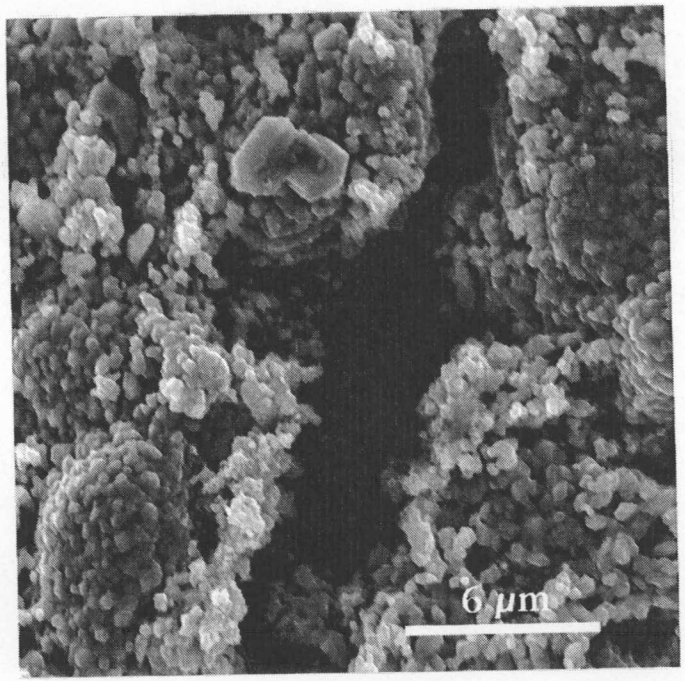

Figure 45: SEM micrograph of zirconia deposit on nickel substrate made at P = 45 Torr, T = 950 °C and what appears to be a microcrack in the coating (5,000X).

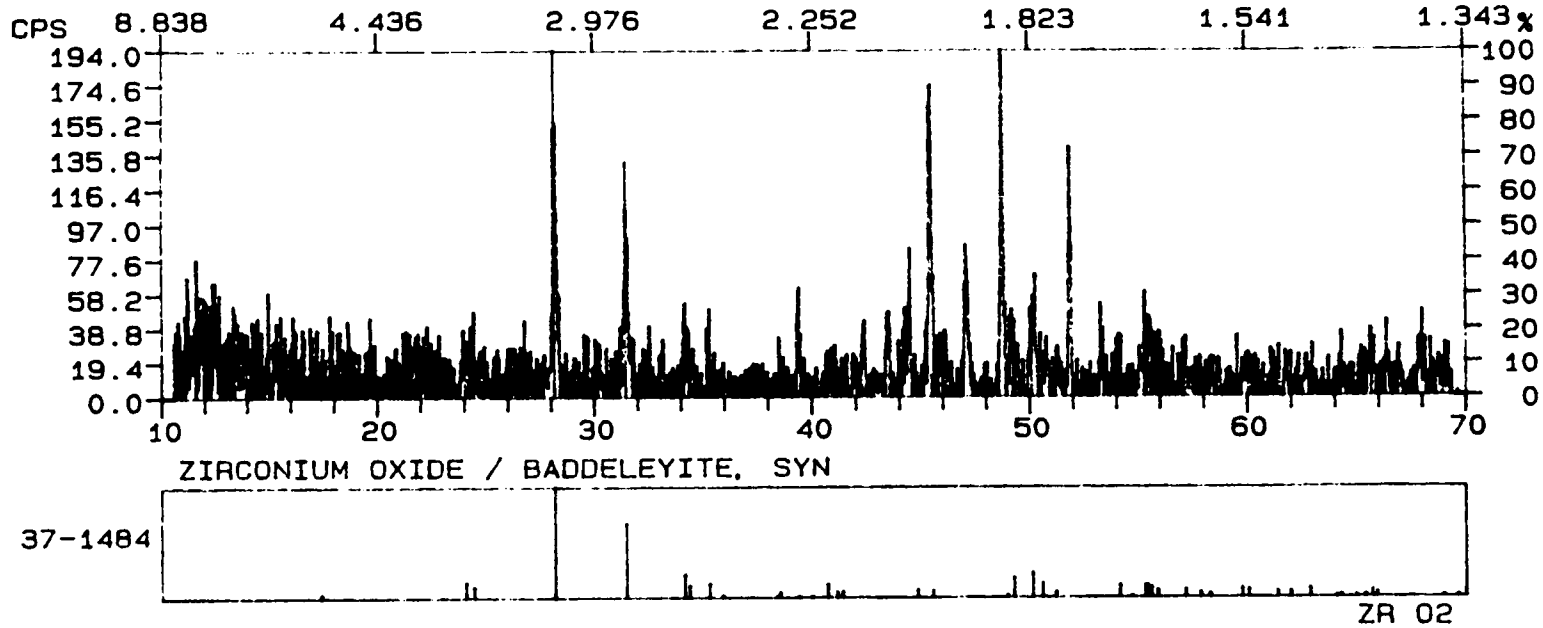

Figure 46: X-ray diffraction pattern of zirconia deposit made at a pressure of 45 Torr and a deposition temperature of 950 °C. The coating was identified as the baddeleyite (monoclinic) form. The strong peak just past 44 represents the nickel substrate.

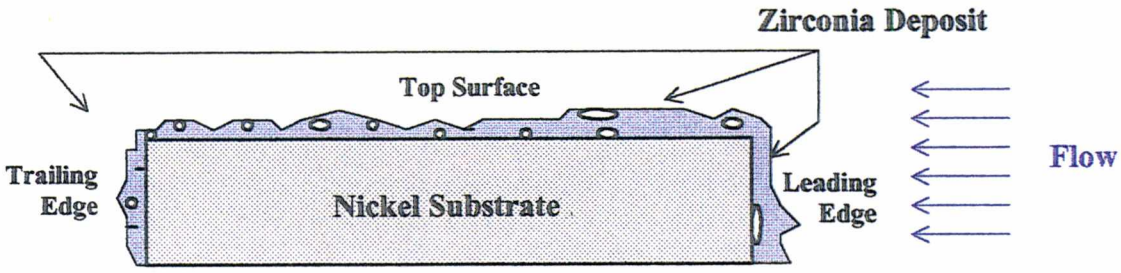

Figure 47: Schematic diagram of sectioned sample with ZrO_2 deposit made at P = 45 Torr, T = 950 °C. Micrographs of leading edge, top surface and trailing edge appear in Figures 47, 48 and 49.

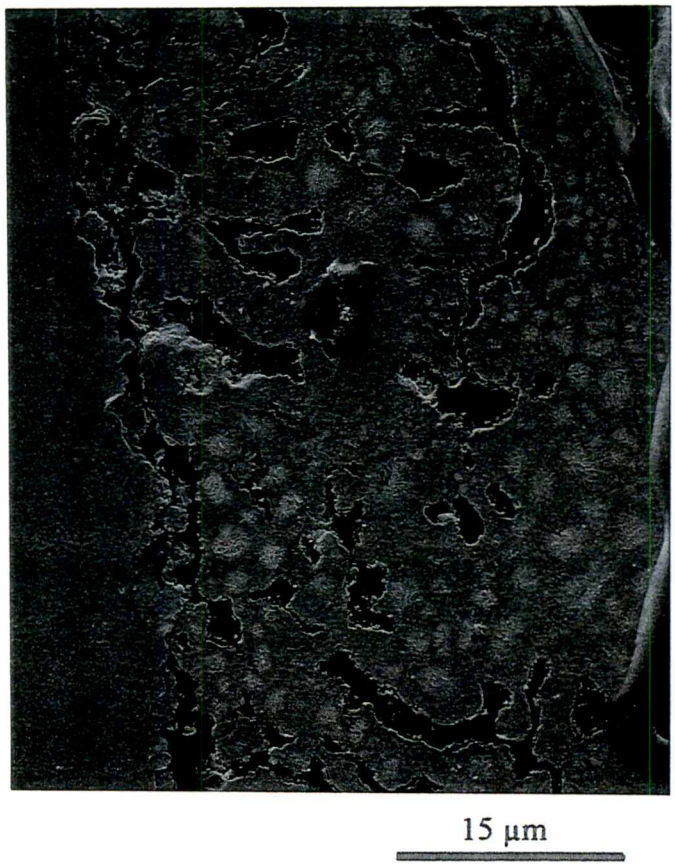

Figure 48: SEM micrograph of leading edge of ZrO_2 deposit made at P = 45 Torr, T = 950 °C (2,000X). Note the porosity.

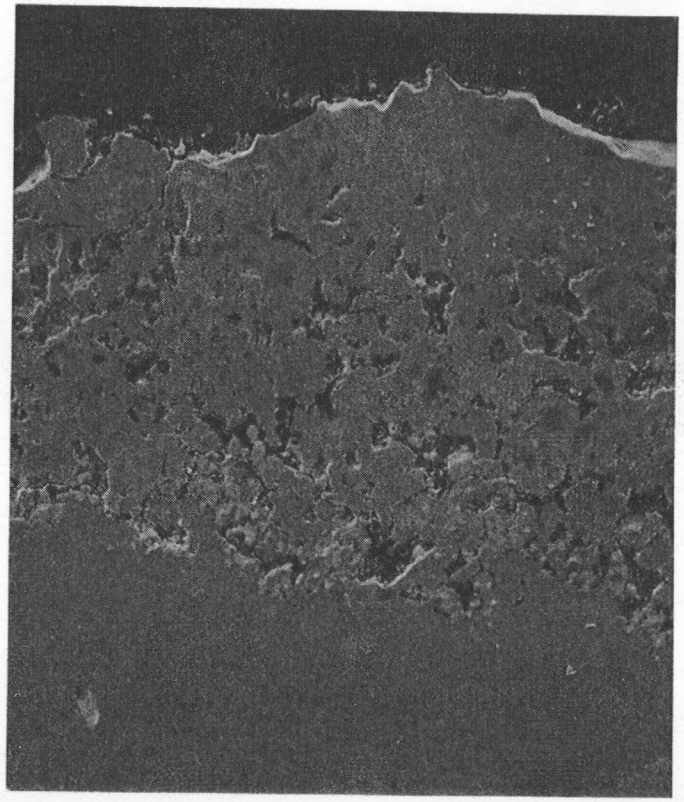

Figure 49: SEM micrograph of cross section of top surface of zirconia deposit made at P = 45 Torr, T = 950 °C (1,050X). The coating's thickness is comparable to that of the leading edge, but with less porosity.

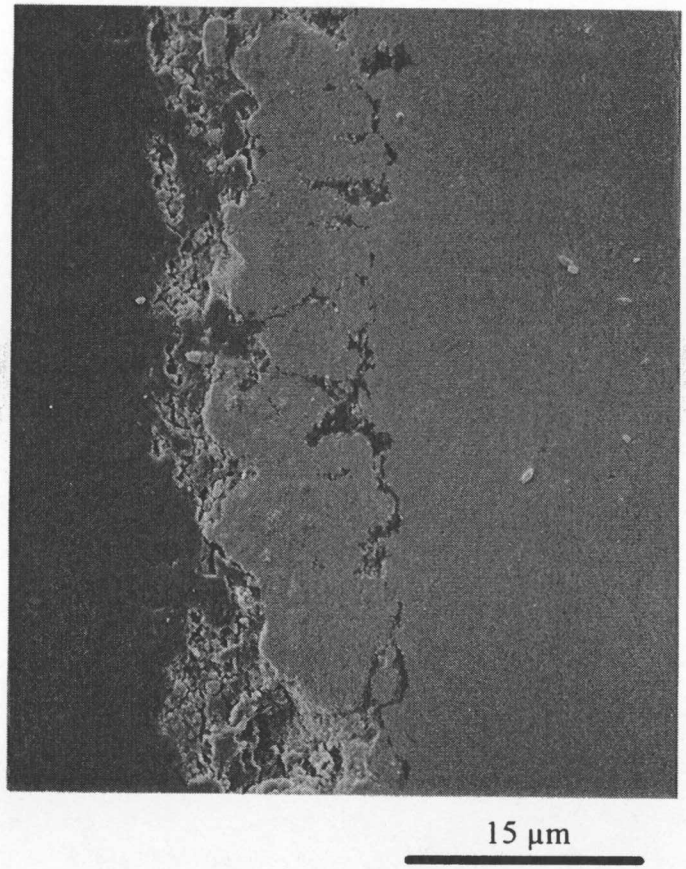

Figure 50: SEM micrograph of cross section of trailing edge of zirconia deposit made at P = 45 Torr, T = 950 °C (2,000X). The coating is substantially thinner and less uniform than on the top or leading edge.

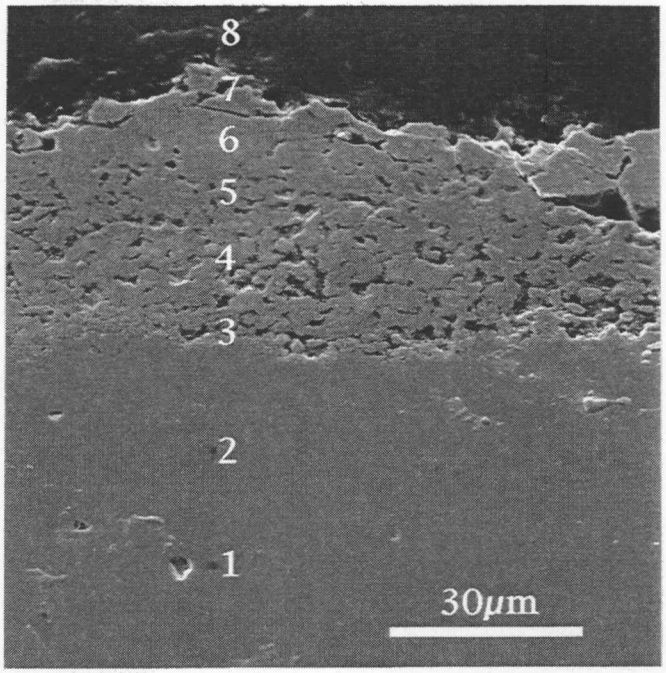

Figure 51: SEM micrograph of cross section of top surface of zirconia deposit made at P = 5 Torr, T = 950 °C (1,000X). Spot EDS scans were made, traversing from the nickel substrate through the ZrO_2 coating and into the epoxy mold in which the sample was mounted. The numbers represent where scans were made and the corresponding results appear in Figures 52-59.

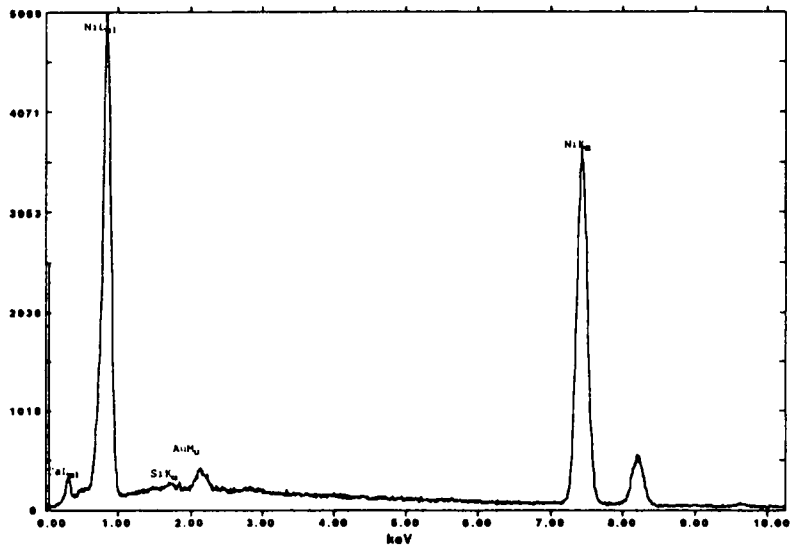

Figure 52: First EDS scan of SEM micrograph from Figure 51. Made squarely on the nickel substrate, this scan shows strong nickel peaks. The silicon peak was the result of contamination from the quartz tube. The gold peak was a result of the gold coating applied to prevent charging within the SEM. The calcium peak is of unknown origin.

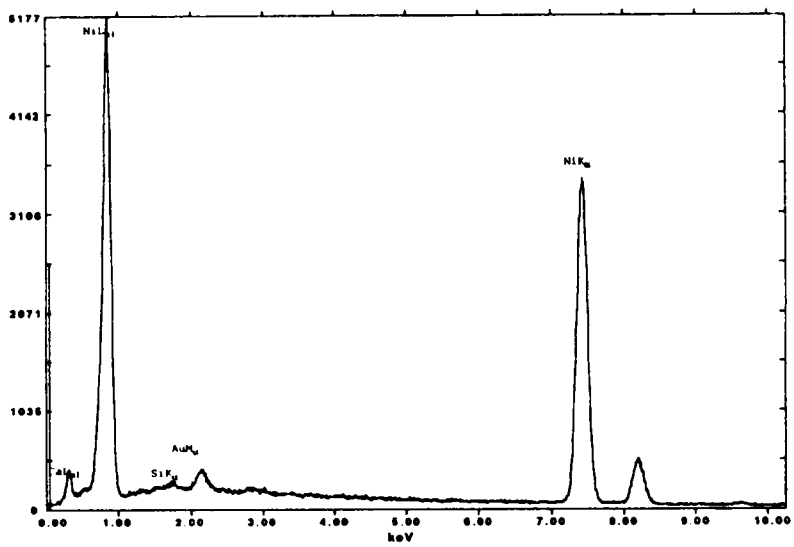

Figure 53: Second EDS scan of SEM micrograph from Figure 51. Strong nickel peaks were again evident. The silicon peak was a contaminant from the quartz tube. The gold peak was from the gold coating applied to prevent charging within the SEM. The calcium peak is of unknown origin.

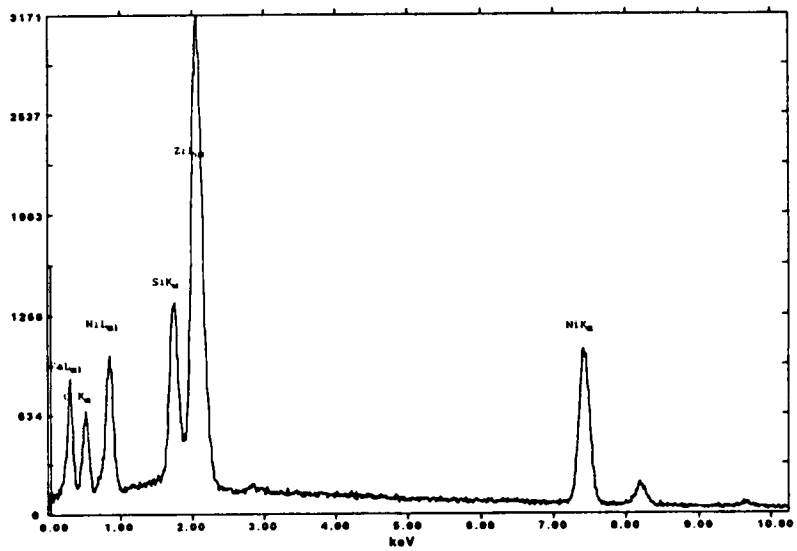

Figure 54: Third EDS scan of SEM micrograph from Figure 51. Made at the interface of the substrate and the deposit. A strong zirconium peak dominates along with the appearance of an oxygen peak (ZrO_2). The nickel peaks are greatly diminished while the silicon and calcium (contaminants) have been strengthened.

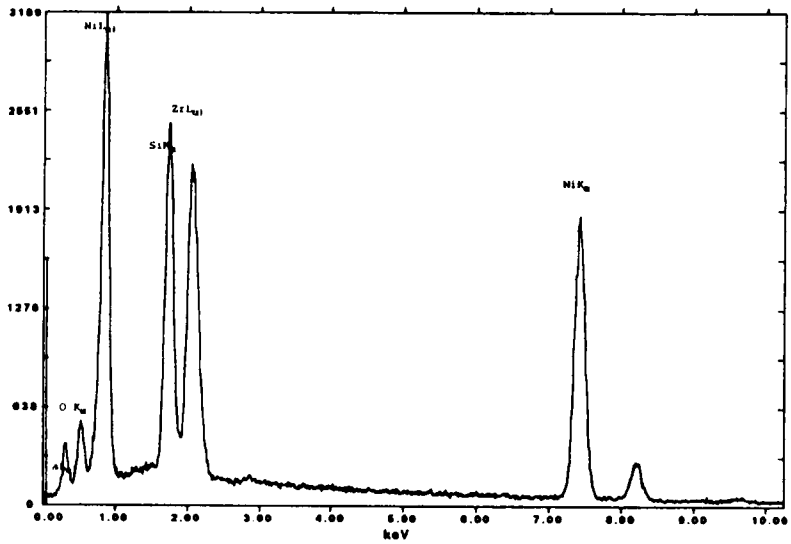

Figure 55: Fourth EDS scan of SEM micrograph from Figure 51. Made squarely on the deposit, zirconium peak is still strong, but nickel and silicon dominate.

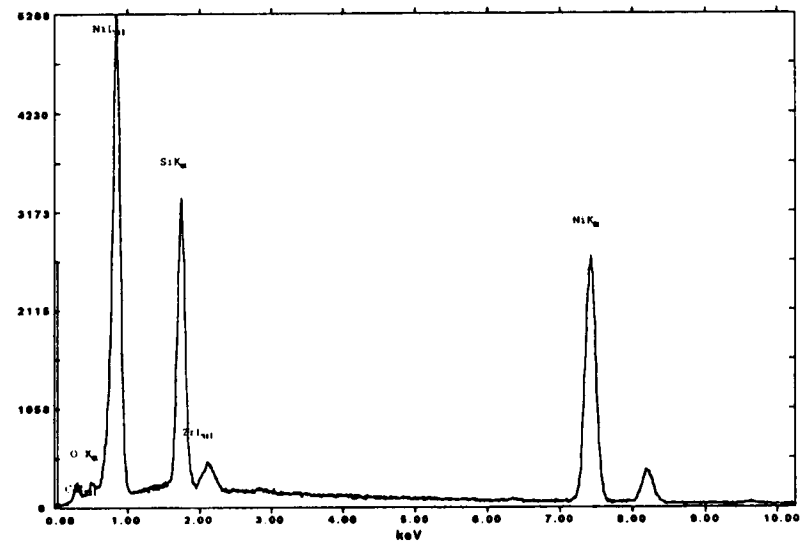

Figure 56: Fifth EDS scan of SEM micrograph from Figure 51. The zirconium continues to diminish while nickel and silicon remain strong.

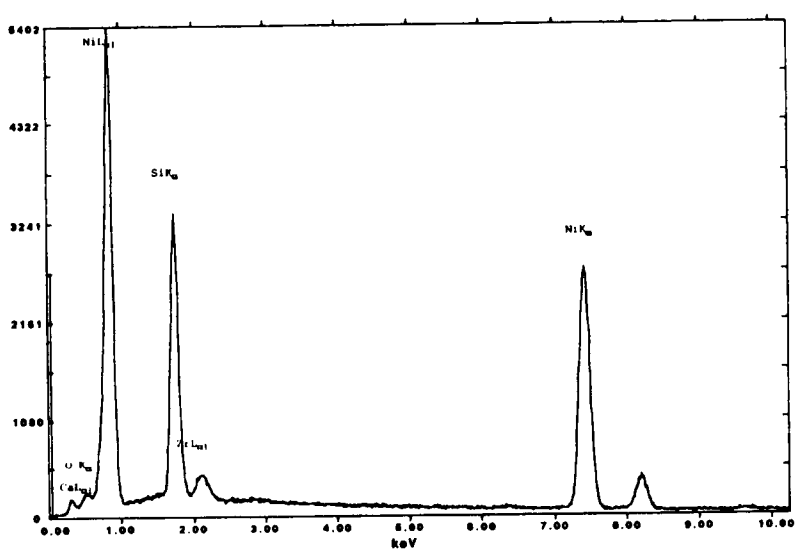

Figure 57: Sixth EDS scan of SEM micrograph from Figure 51. Nickel and silicon peaks continue to dominate

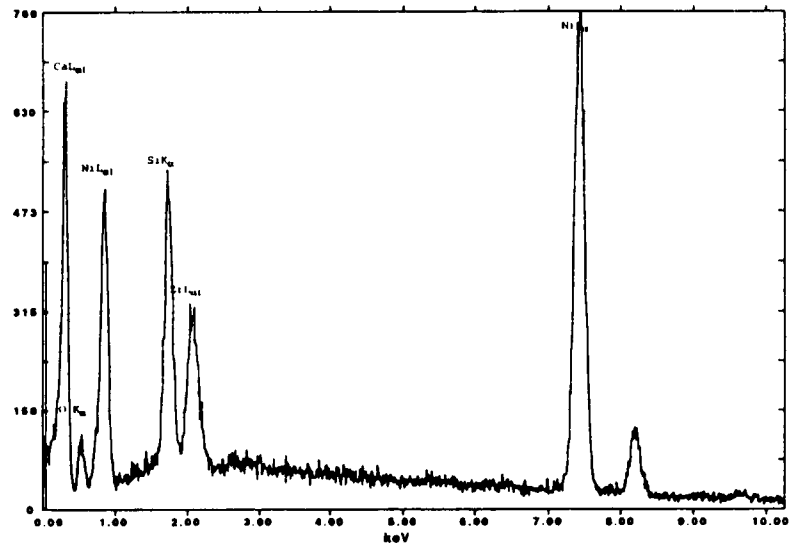

Figure 58: Seventh EDS scan of SEM micrograph from Figure 51. The zirconium peak has increased while nickel and silicon peaks remain strong. The calcium peak has rebounded to dominate the scan.

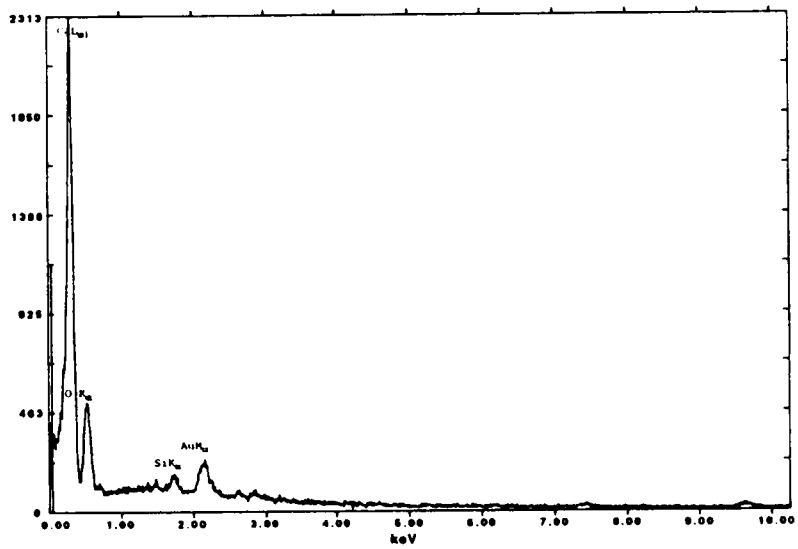

Figure 59: Eighth EDS scan of SEM micrograph from Figure 51. Made squarely on the epoxy mounting, nickel and zirconium peaks were absent while calcium dominates. This suggests that the calcium contamination resulted from either the mounting or polishing of the sample.

15 µm

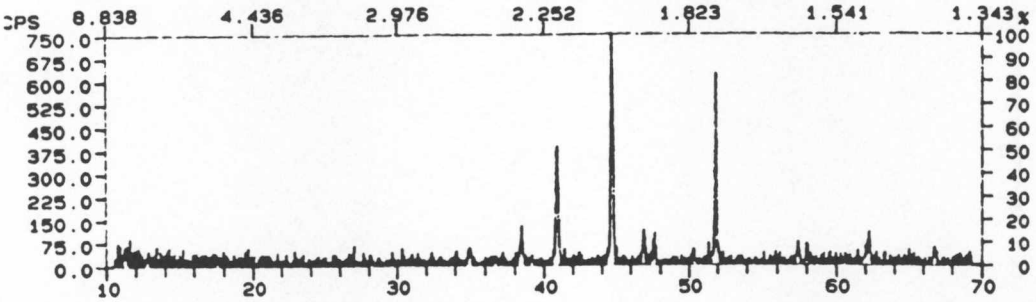

Figure 60: SEM micrograph and XRD pattern of ZrO_2 deposited at P = 45 Torr, T = 1050 °C (2,000X). Note the similarities between this coating and that which appears in Figure 40. While these crystals are much finer, they are similar in morphology and identical in composition.

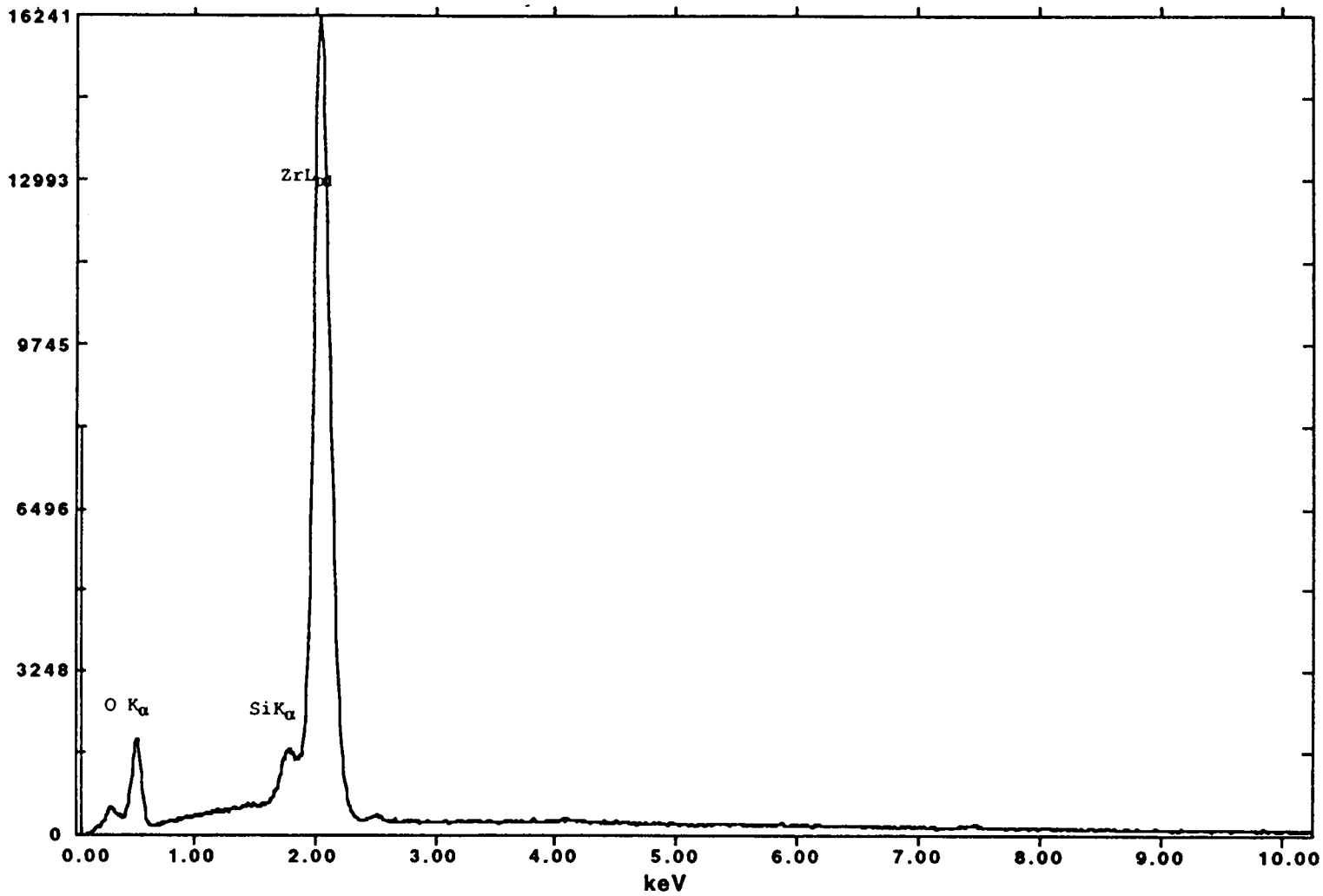

Figure 61: EDS scan of the deposit made at P = 45 Torr, T = 1050 °C. This scan is virtually identical to the one which appears in Figure 41. Again, the strong zirconium and oxygen peaks suggest a form of zirconia.

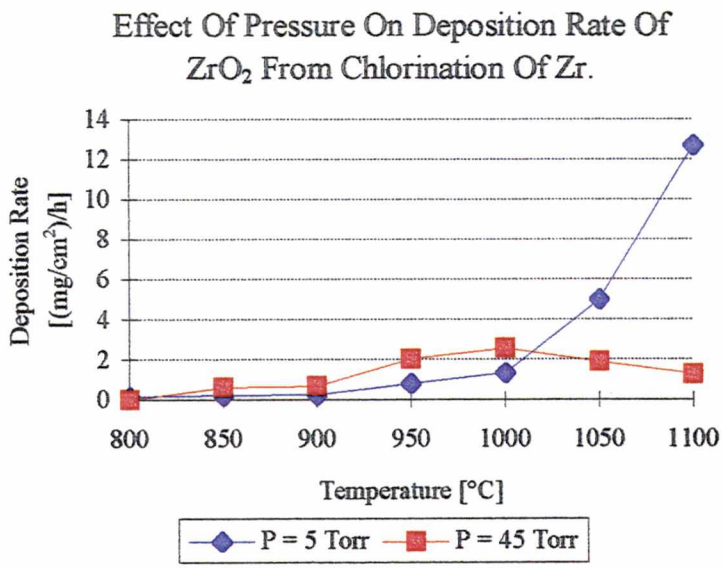

Figure 62: Effect of pressure on deposition rate of ZrO_2 at 2 cm from zirconium source. Rates are higher for P = 45 Torr up to 1000 °C. At T > 1000 °C, the rate is higher at P = 5 Torr, but the deposition formed is undesirable.

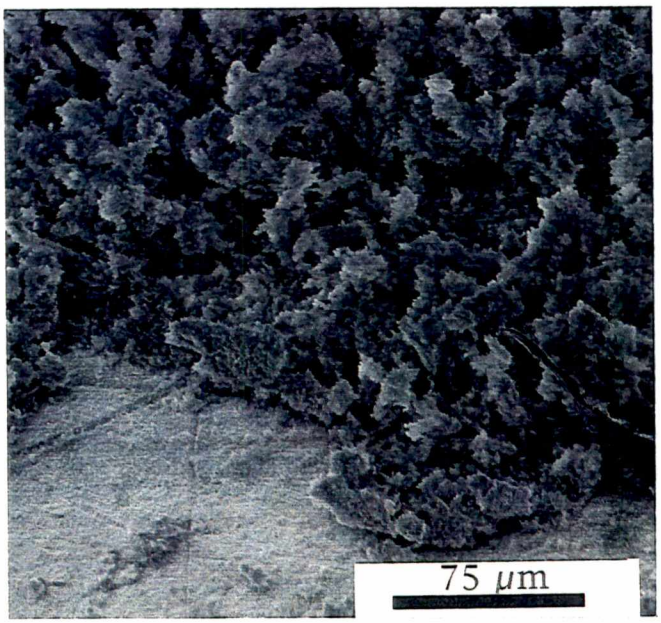

Figure 63: SEM micrograph of typical zirconia deposit produced using $Zr(tmhd)_4$ as a precursor (400X). The coating had poor morphology with low adherence to the nickel substrate. Nickel substrate is visible in the lower left of the micrograph.

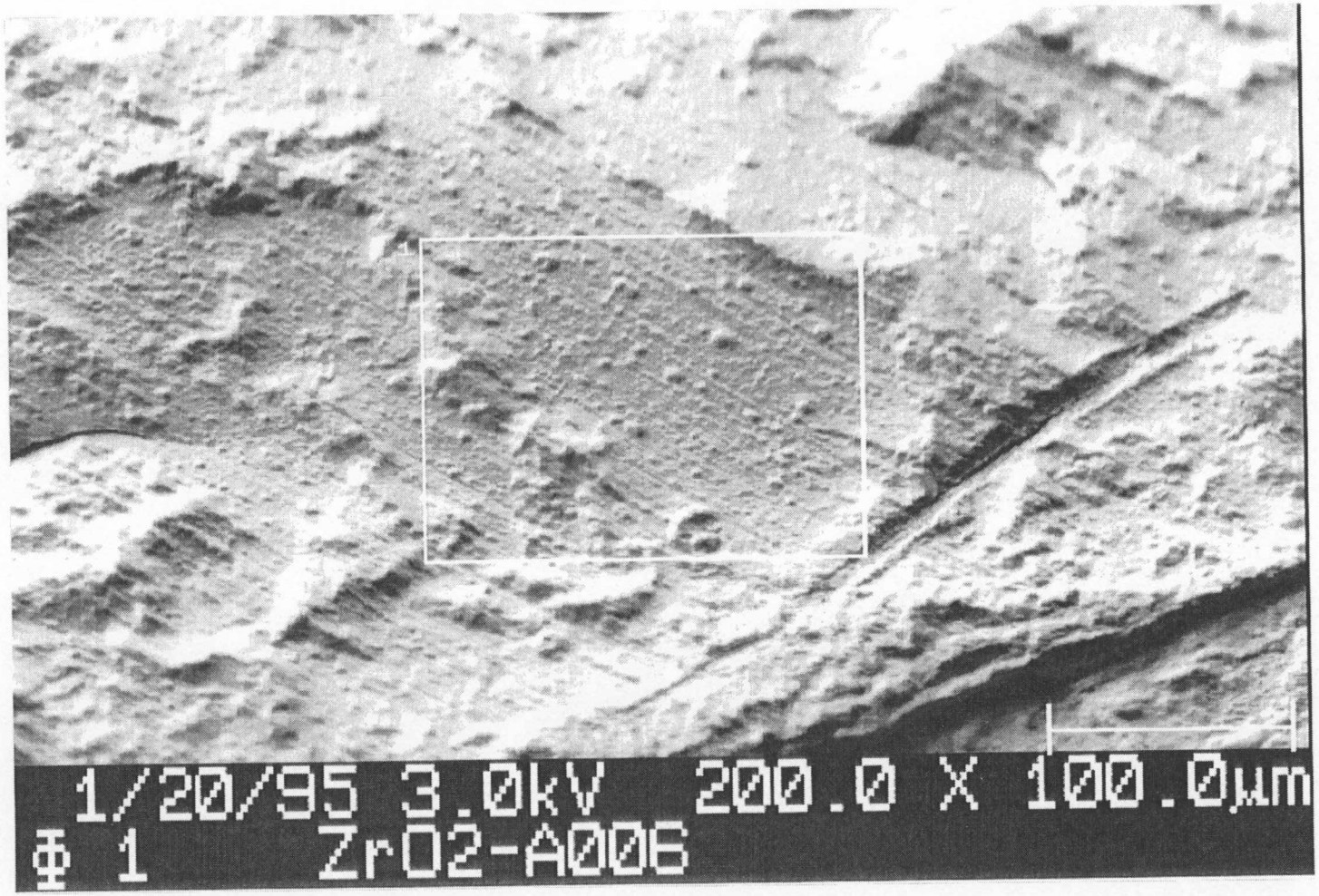

Figure 64: Magnified area of deposit made at 750 °C using zirconium metalorganic as a precursor and area scanned using AES. AES analysis was performed on the area within the outlined box.

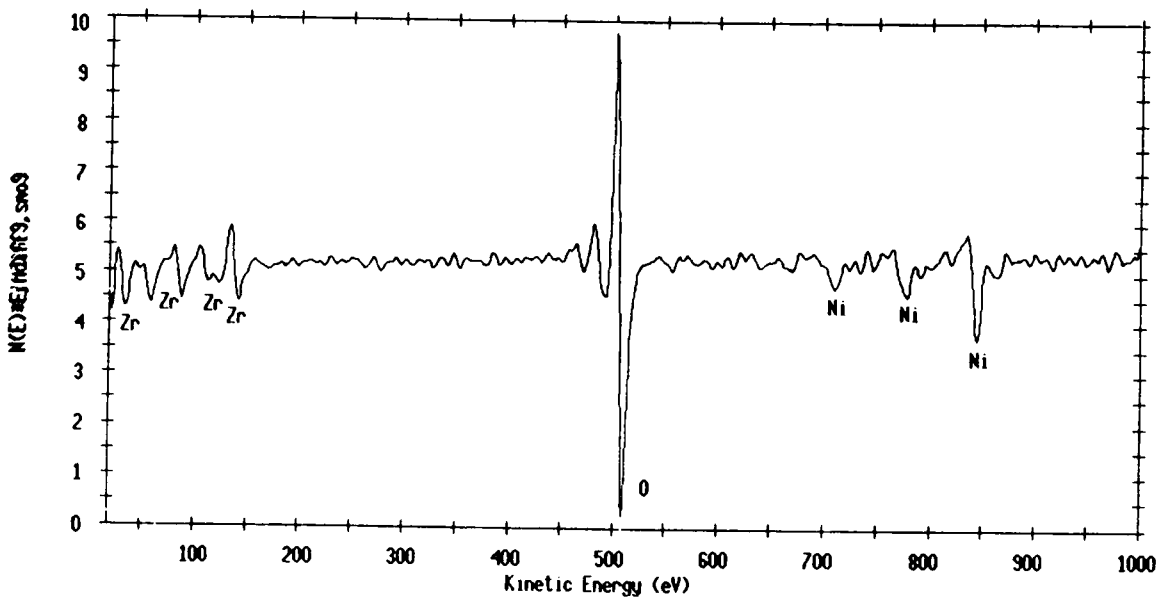

Element	Peak-to-peak	Sensitivity Factor	Concentration (%)
Zr1	487133	0.220	21.80
O1	2907533	0.500	57.26
Ni1	574266	0.270	20.94

Figure 65: AES scan and atomic concentration of boxed off area which appears in Figure 64. Oxygen and zirconium are present in roughly a 2:1 ratio. This was taken to be ZrO_2. The remainder of the oxygen is believed to be present in nickel oxide.

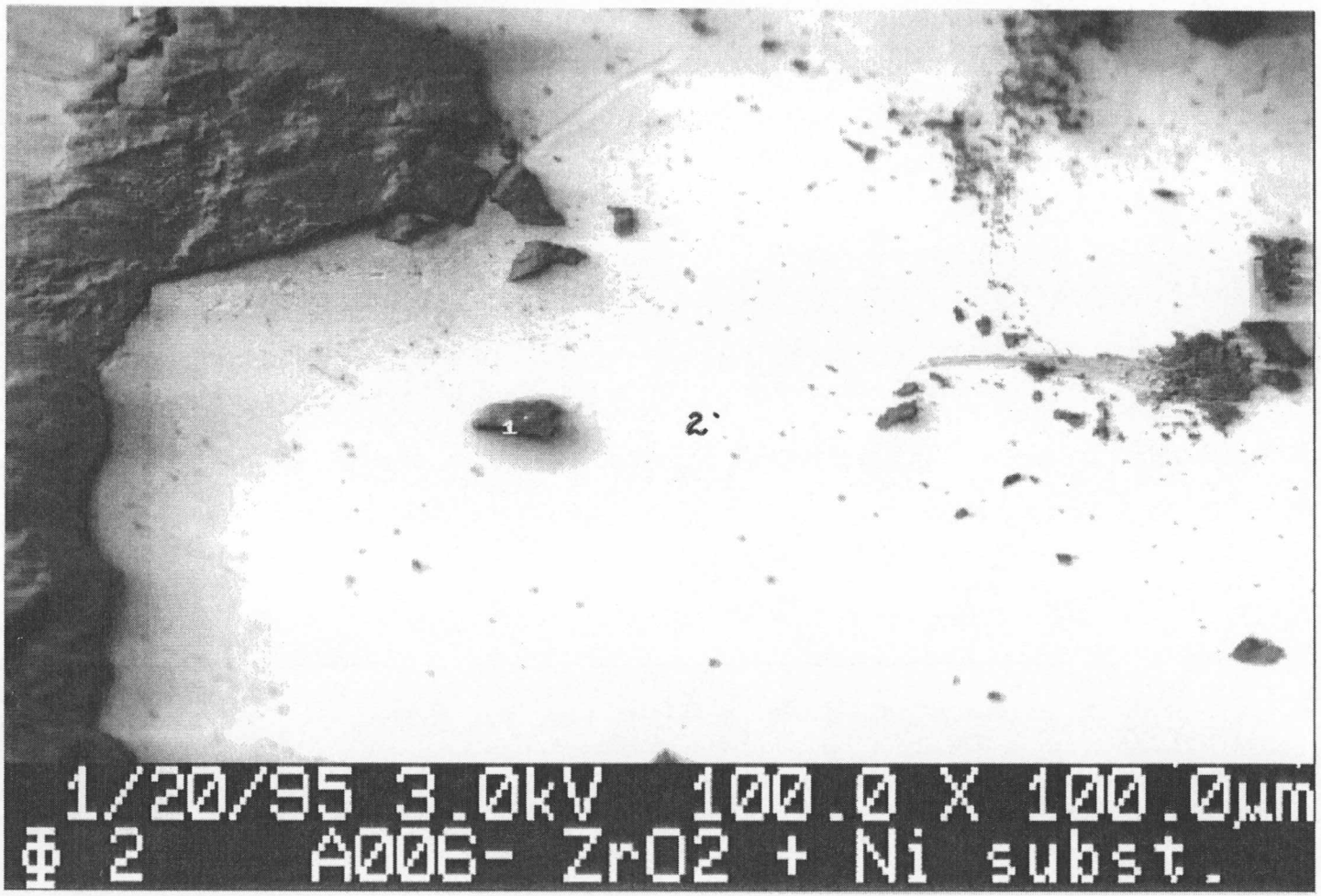

Figure 66: Deposit made at 750 °C using zirconium metalorganic precursor and areas scanned using AES (denoted 1 and 2). The results of the two scans appear in Figures 67 and 68, respectively.

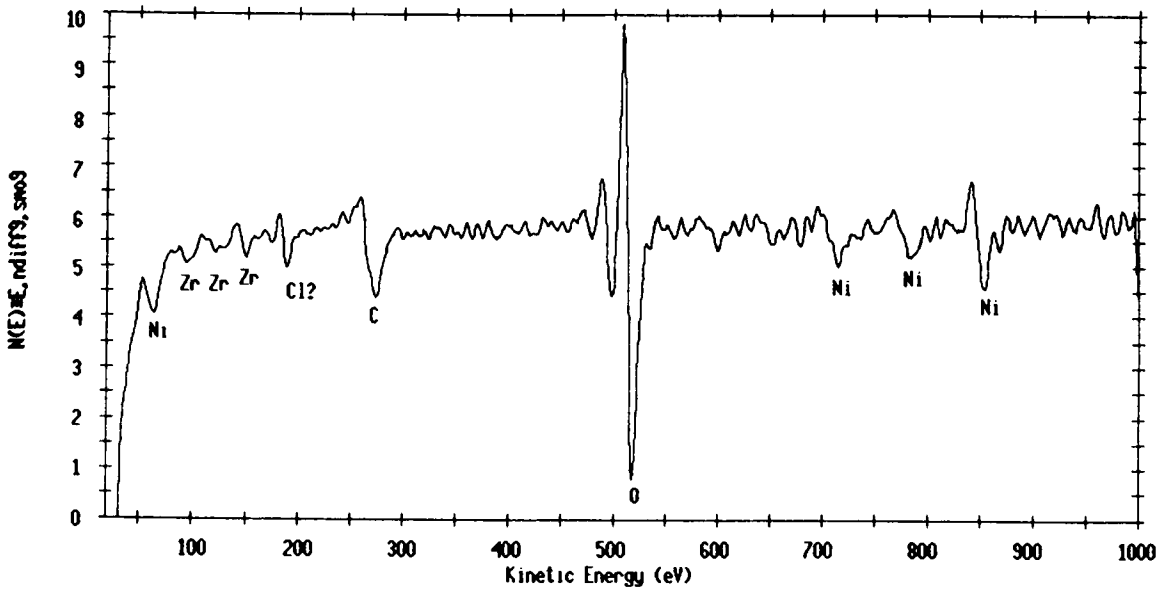

Element	Peak-to-peak	Sensitivity Factor	Concentration (%)
Zr1	184200	0.220	9.61
Cl1	271400	1.100	2.83
C1	406466	0.180	25.93
O1	1661000	0.500	38.14
Ni1	552133	0.270	23.48

Figure 67: Result of first AES scan from Figure 66. Less zirconium than expected was detected. The chlorine was a contaminant from earlier runs (Al_2O_3 from $AlCl_3$). The carbon contamination was suspected to have resulted from the metalorganic.

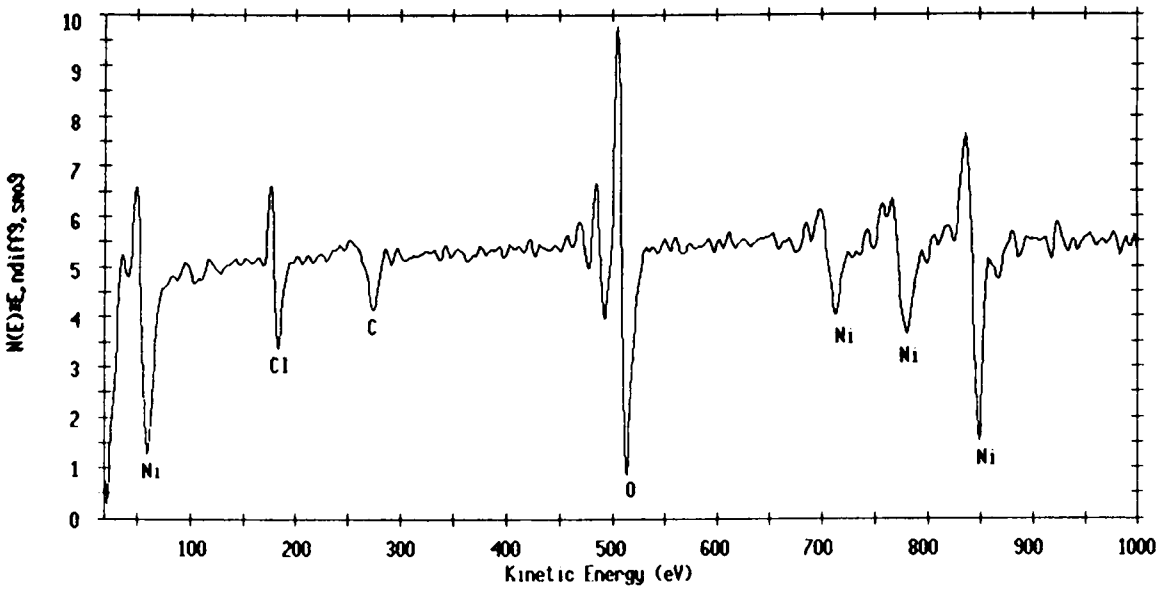

Element	Peak-to-peak	Sensitivity Factor	Concentration (%)
Cl1	769600	1.100	6.69
C1	277333	0.180	14.73
O1	1896466	0.500	36.26
Ni1	1195200	0.270	42.32

Figure 68: Result of second AES scan from Figure 66. No zirconium was detected here. Carbon and chlorine contaminants were, however, along with nickel and oxygen.

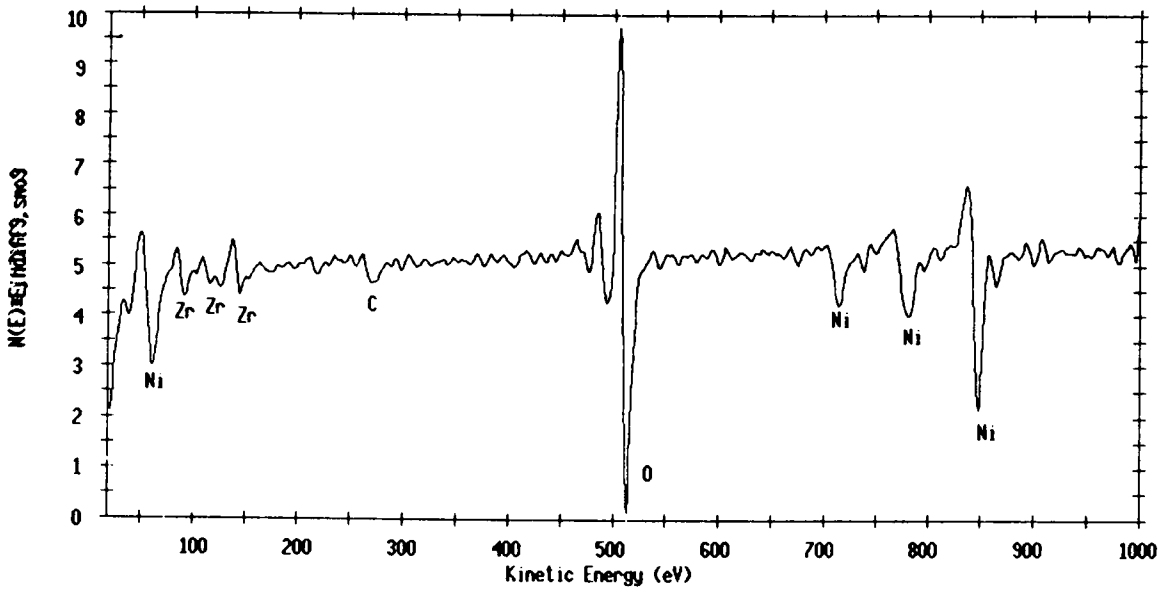

Element	Peak-to-peak	Sensitivity Factor	Concentration (%)
O1	2403400	0.500	42.87
Ni1	996666	0.270	32.92
Zr1	346066	0.220	14.03
C1	205533	0.180	10.18

Figure 69: AES scan conducted on deposit made using $Zr(tmhd)_4$ precursor at 1050 °C. It was hoped that elevating the deposition temperature would promote the formation of CO_2, thus eliminating the carbon contamination. While less carbon was detected, it was still present.

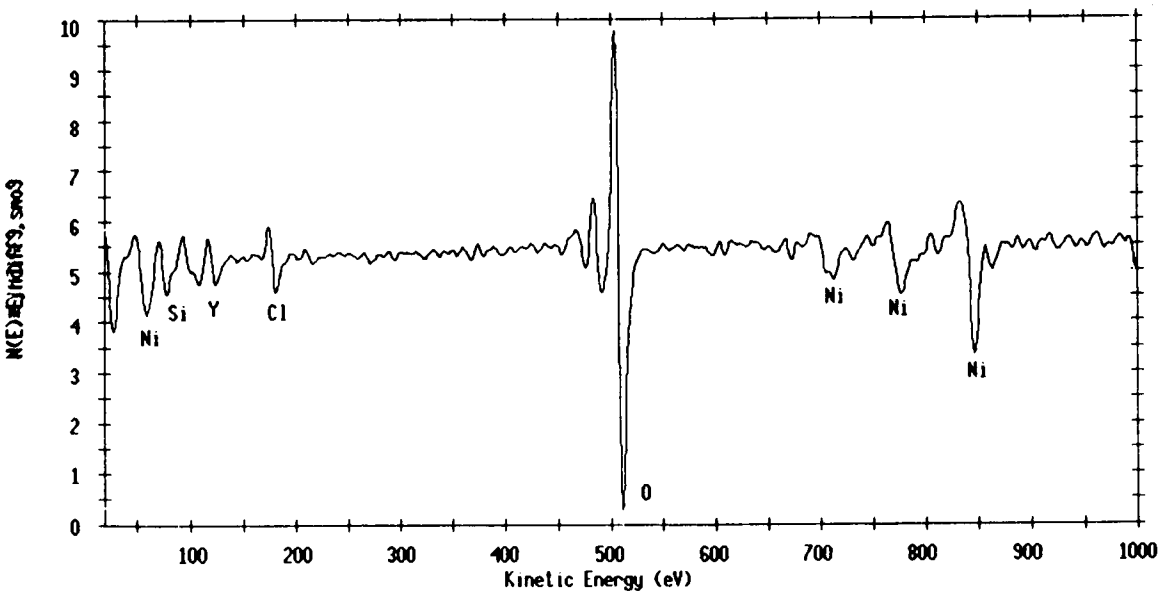

Element	Peak-to-peak	Sensitivity Factor	Concentration (%)
O1	2547066	0.500	48.35
Ni1	733533	0.270	25.78
Si1	307066	0.350	8.33
Y1	257000	0.170	14.35
Cl1	370333	1.100	3.20

Figure 70: AES scan conducted on deposit made using $Y(tmhd)_3$ as a precursor. Yttrium was detected along with oxygen and nickel. Also espied were chlorine and silicon contaminants.

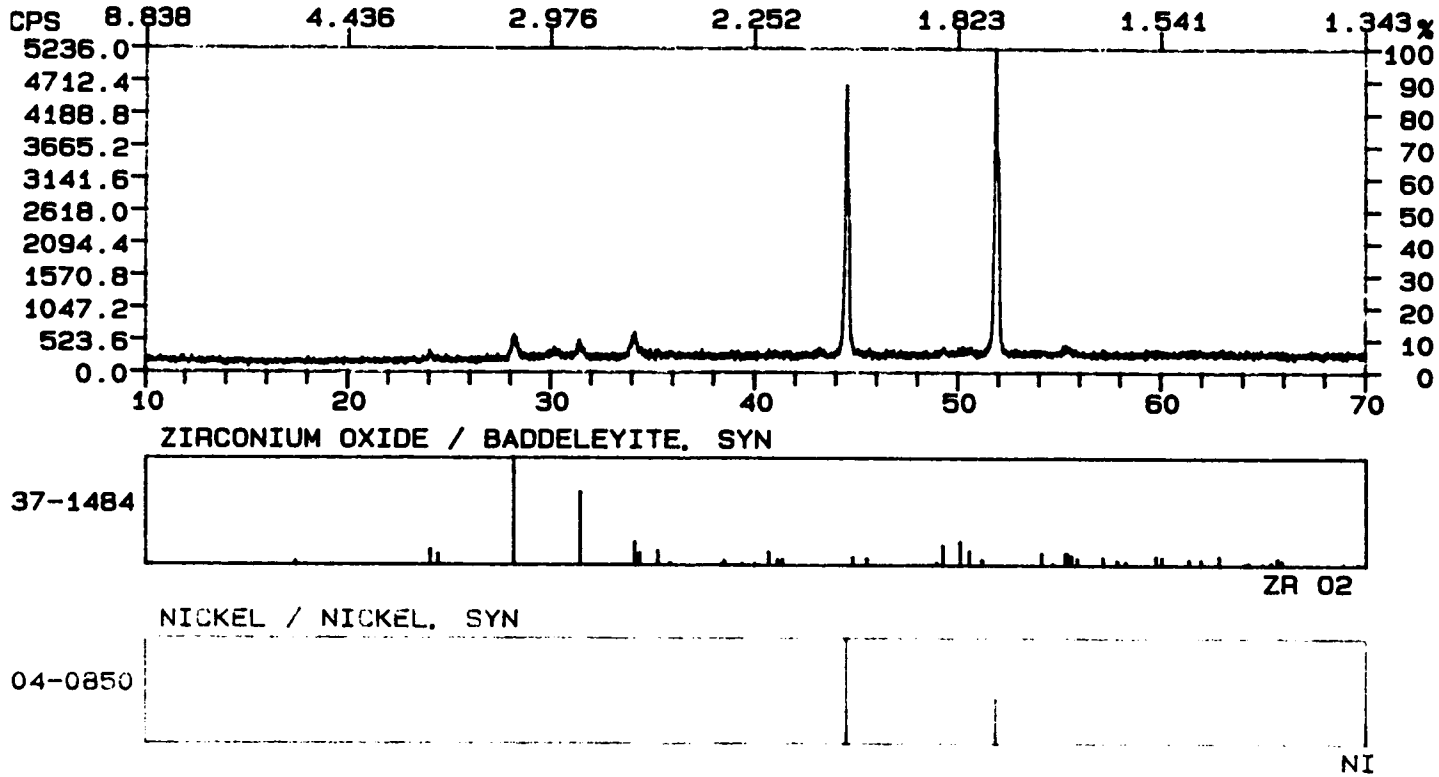

Figure 71: XRD scan of deposit made using zirconium and yttrium metal-organics as precursors. Monoclinic zirconia (baddeleyite) was detected. This was the same form which had been deposited from zirconium tetrachloride. No yttria was detected.

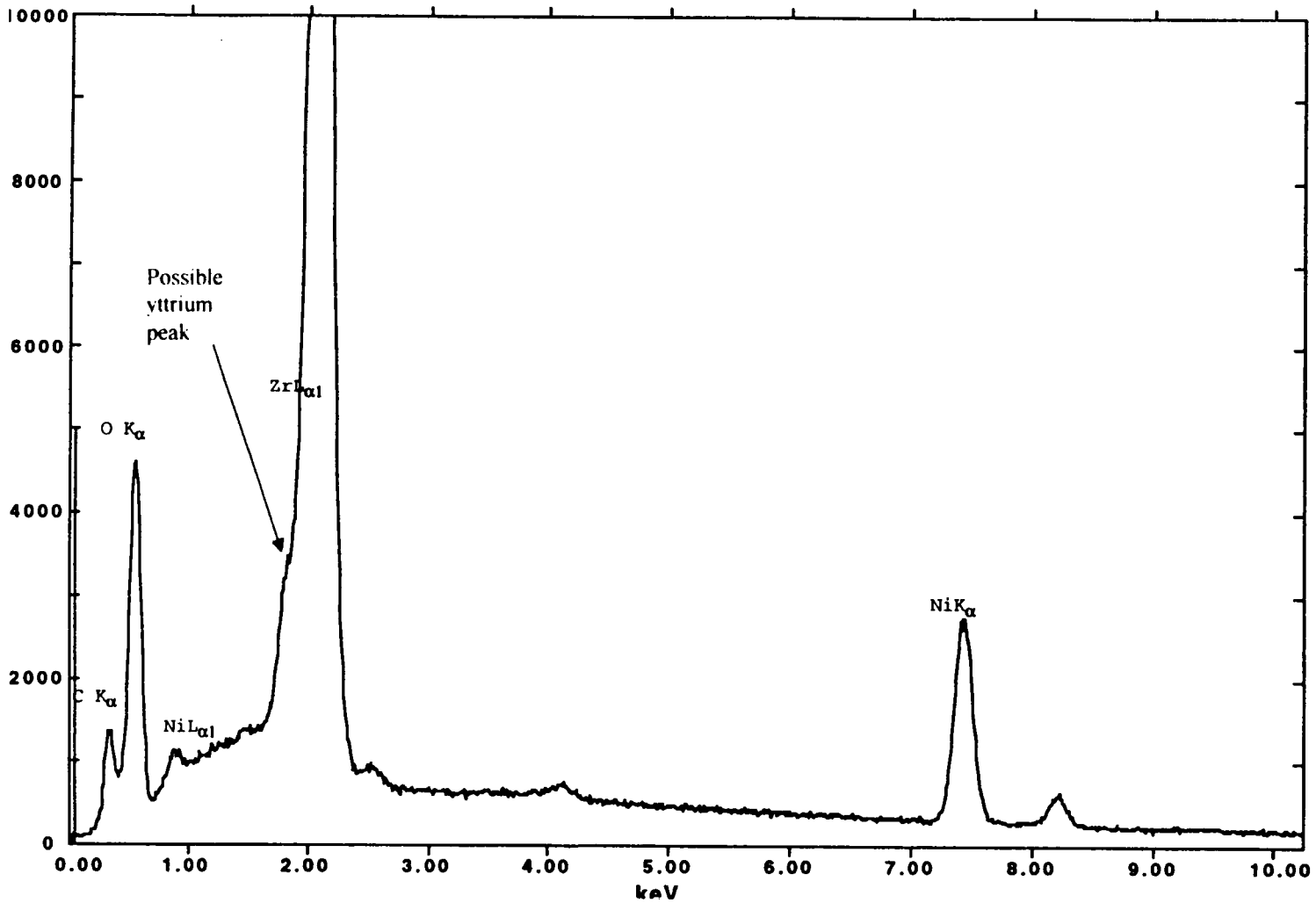

Figure 72: EDS scan of deposit made using zirconium and yttrium precursors. Broadened zirconium peak coupled with small cleft may indicate the presence of yttrium.

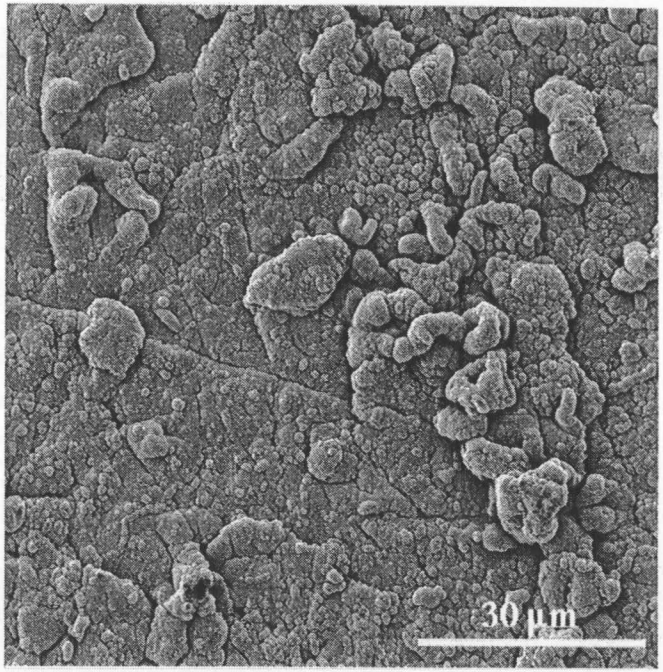

Figure 73: SEM micrograph of deposit made using Zr and Y metalorganic precursors (1,000X). The coating was not uniform. Clearly visible on the surface are what appear to be microcracks.

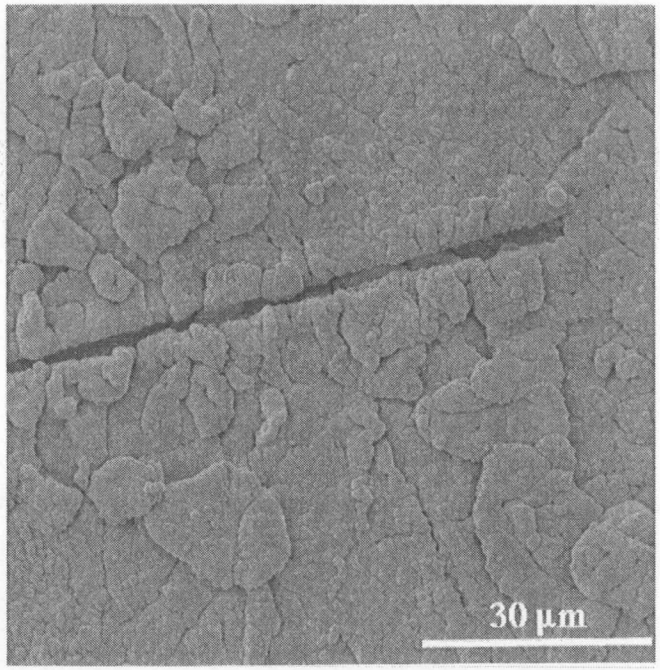

Figure 74: SEM micrograph of scratch made using tweezers on surface of deposit obtained using Zr and Y metalorganic precursors (1,000X). All depositions obtained from the metalorganic precursors appeared soft and scratched easily.

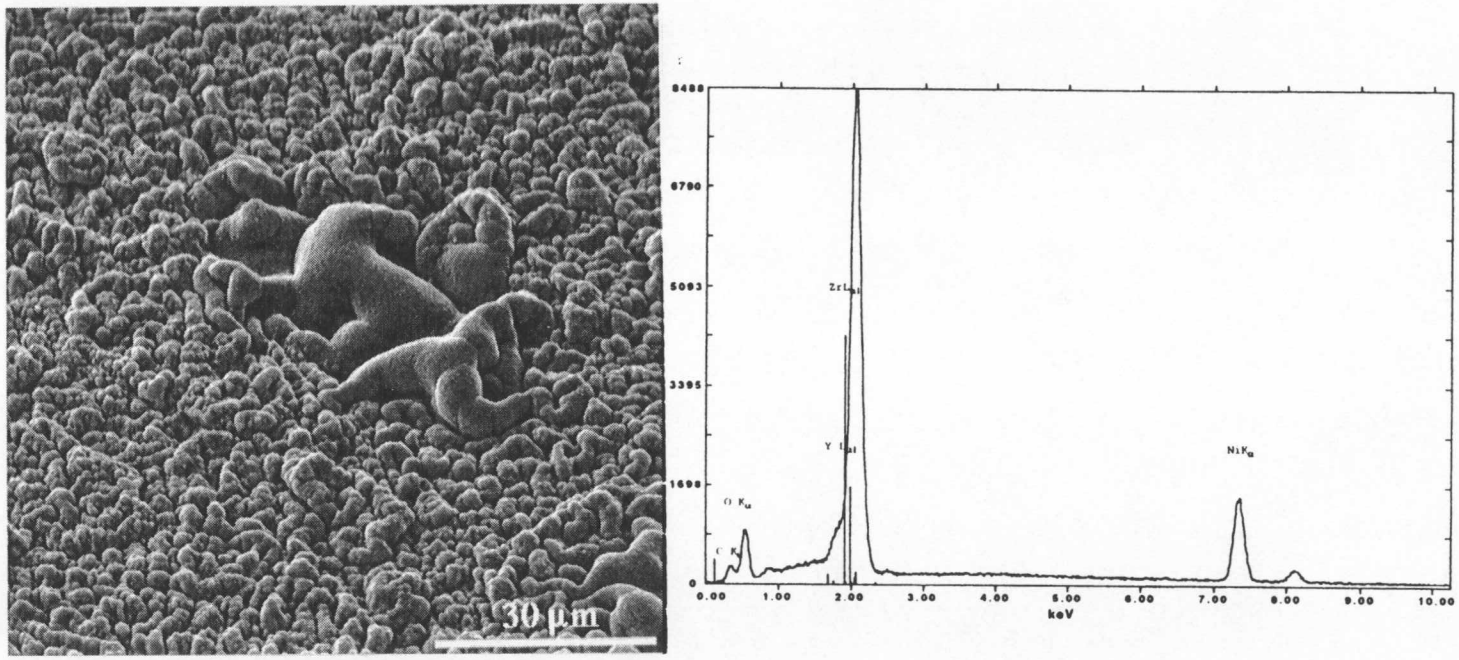

Figure 75: SEM micrograph (1,000X) and EDS scan of large clump formation in deposit formed using zirconium and yttrium metalorganic precursors. The nickel peaks were greatly reduced, indicating that the clump was much thicker than the surrounding area. Zirconium was detected, but nothing definite could be said about the presence of yttrium. Note the carbon peak, suspected to be contamination from the precursor.

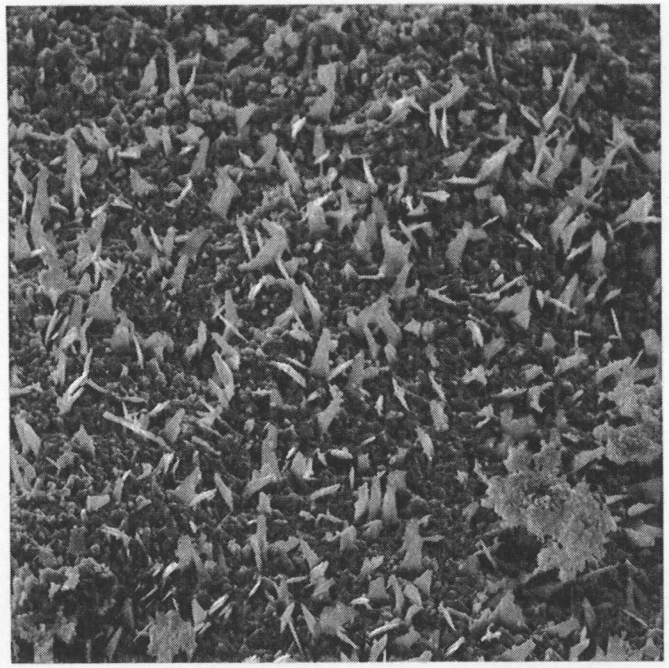

15 μm

Figure 76: SEM micrograph of zirconia coating made using Reactor 4 (2,000X). Note the relatively uniform distribution of blades and smaller crystals.

6 μm

Figure 77: SEM micrograph of zirconia coating made using Reactor 4 (5,000X).

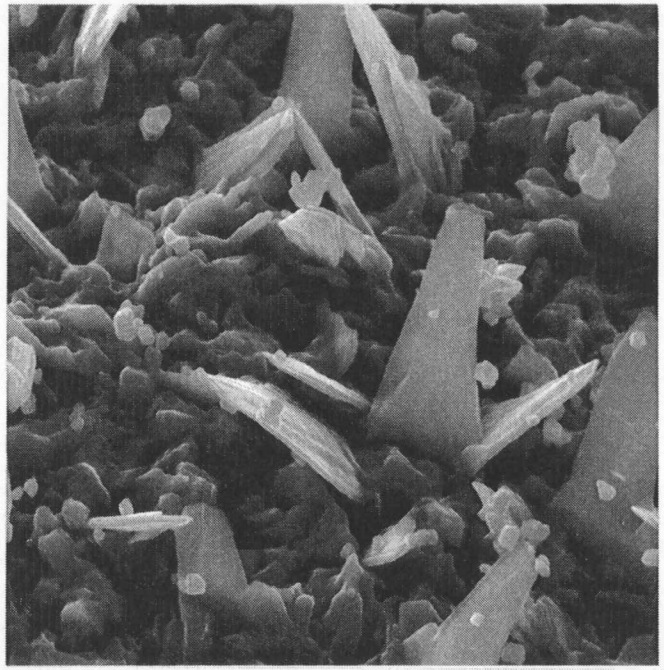

3 μm

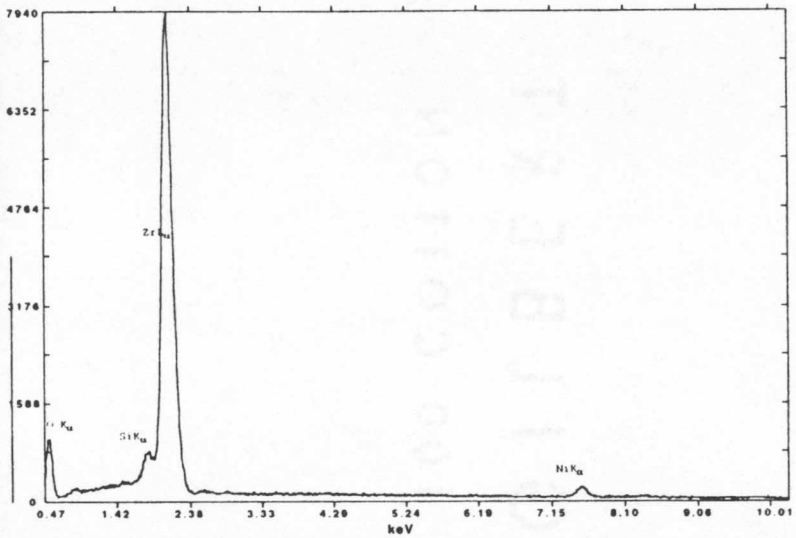

Figure 78: SEM micrograph (10,000X) and EDS scan of zirconia deposit made using Reactor 4. Note highly crystalline, blade-like platelets in micrograph. The EDS scan revealed a strong zirconium peak with lesser peaks indicating oxygen, nickel (substrate) and silicon (contamination).

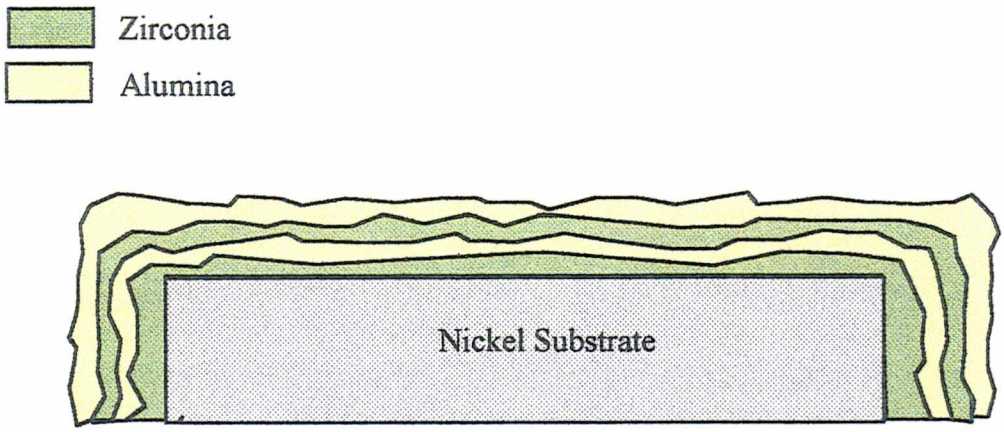

Figure 79: Schematic diagram of layered ZrO_2/Al_2O_3 coating.

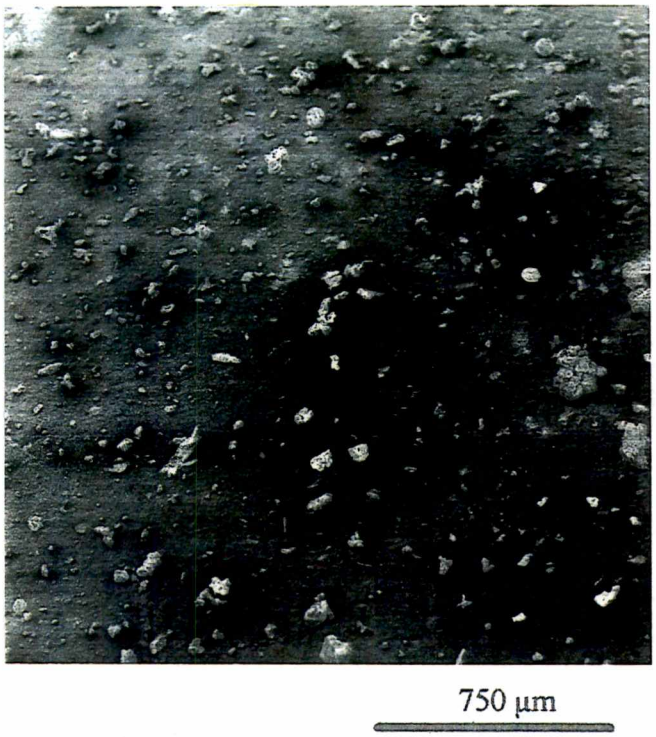

Figure 80: SEM micrograph of surface (Al_2O_3) of layered coating (40X). The majority of the area appears relatively smooth with white nuggets scattered about.

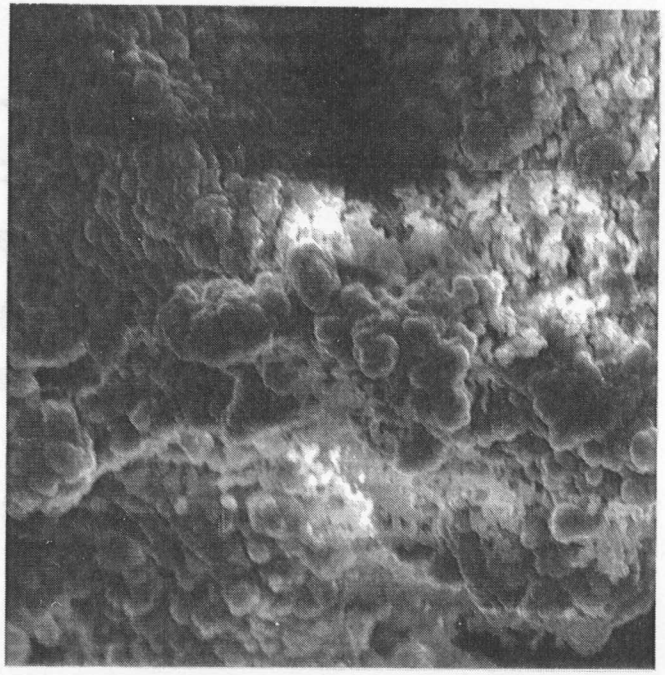

15 μm

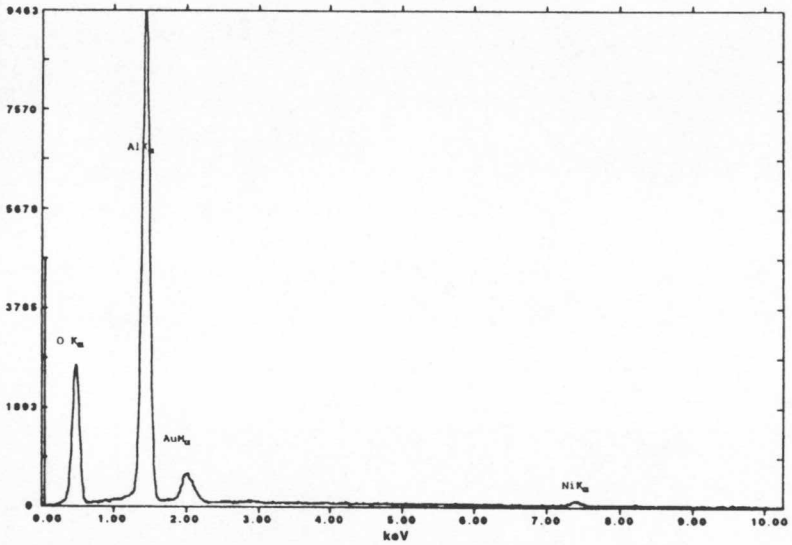

Figure 81: SEM micrograph (2,000X) and EDS scan of a nugget which appeared in Figure 80. The nugget appears to be a collection of much smaller deposits. The EDS scan revealed that it was made up predominantly of aluminum and oxygen, which was taken to be alumina.

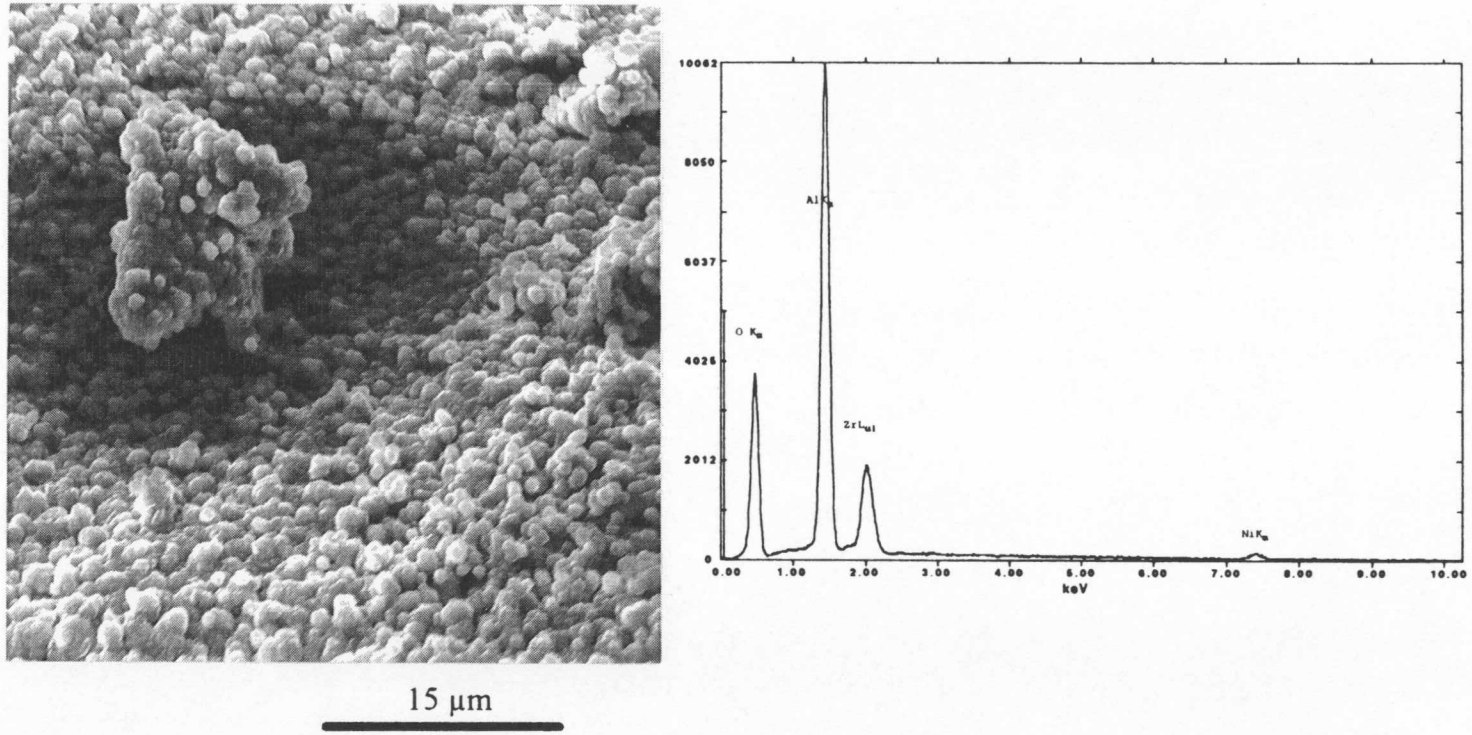

Figure 82: SEM micrograph (2,000X) and EDS scan of smooth area which appeared in Figure 80. It again appeared to be a collection of much smaller deposits. The EDS scan revealed that it was made up predominantly of aluminum and oxygen, which was taken to be alumina. Also present was some zirconium, which was assumed to be zirconia from the underlying

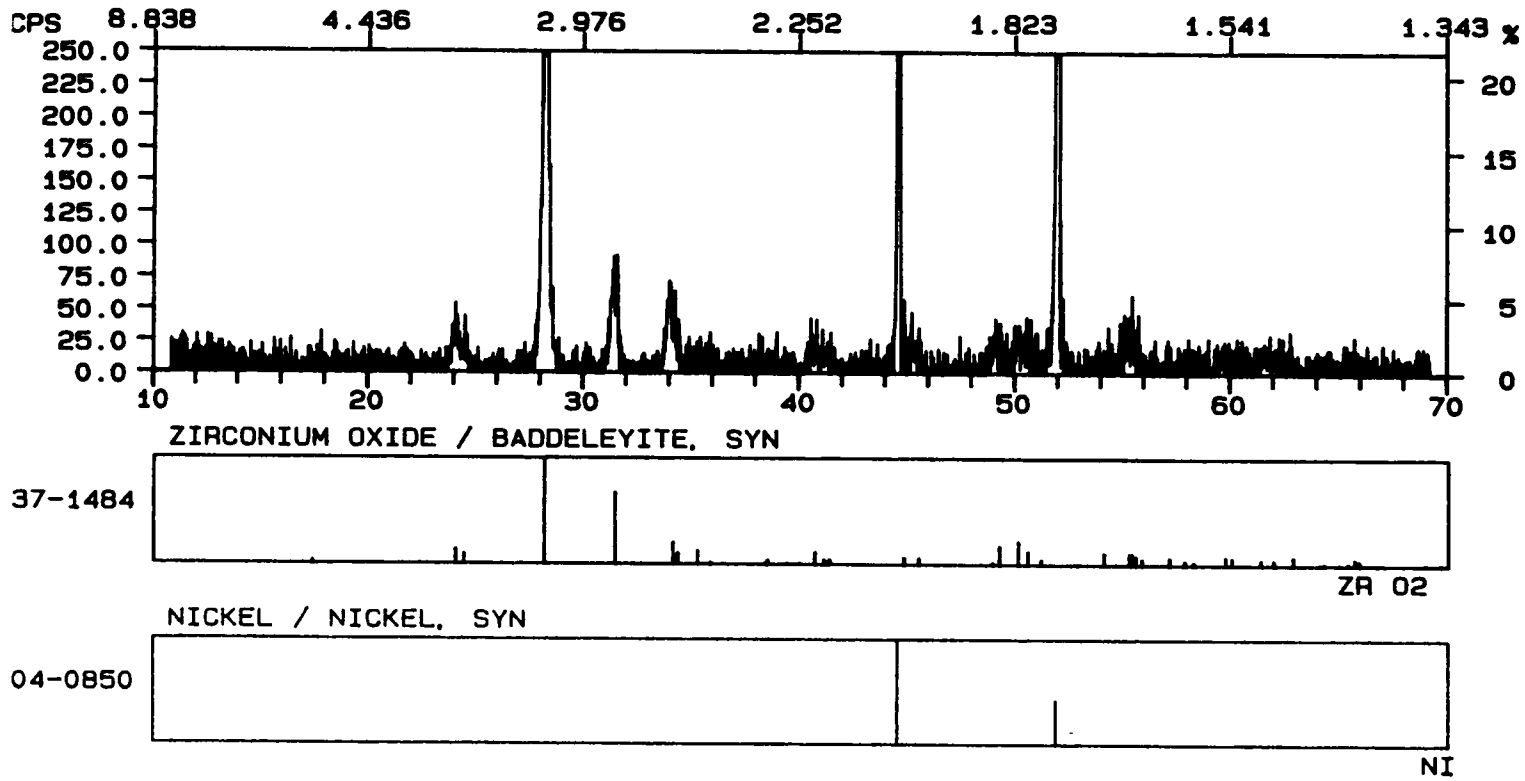

Figure 83: XRD pattern of multi-layered coating with alumina on top surface. No alumina was detected, but monoclinic zirconia was. It was hypothesized that the alumina deposit was penetrated by the X-rays and only the underlying zirconia was detected.

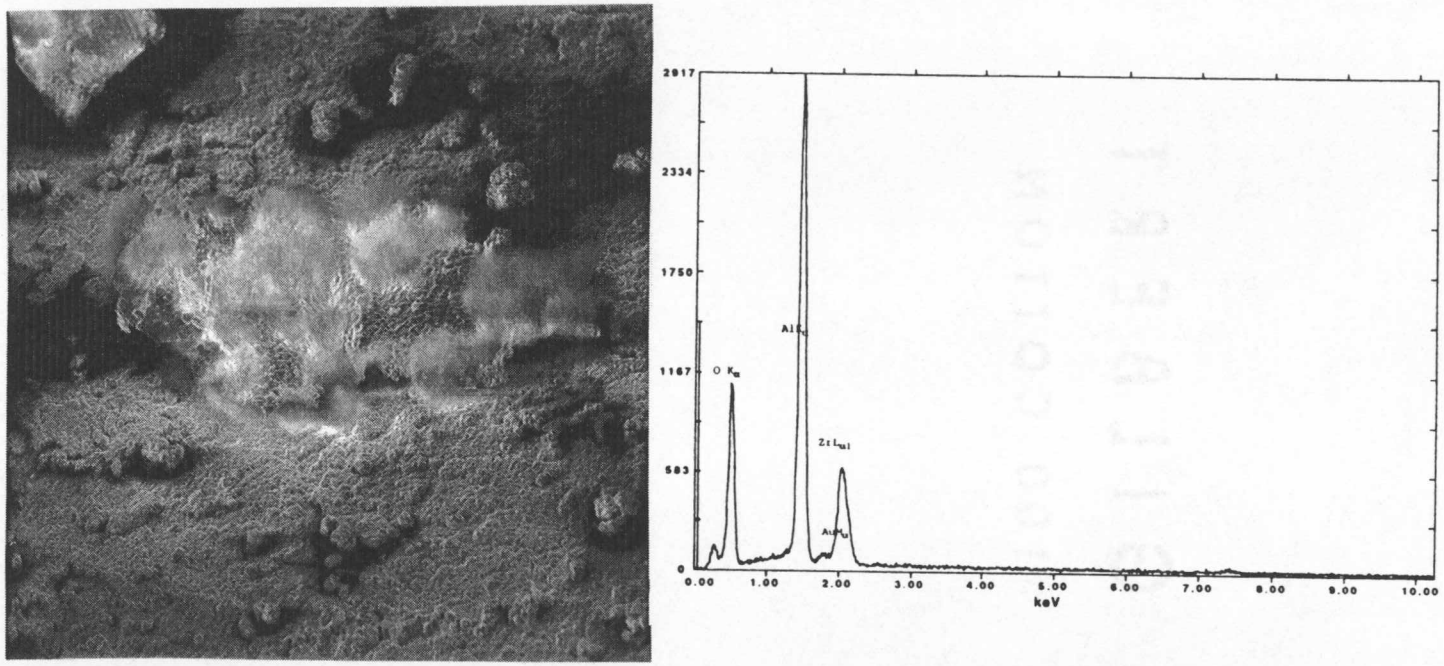

Figure 84: SEM micrograph (150X) and EDS scan of surface of multi-layered coating. This top layer should be alumina and the large aluminum and oxygen peaks of the EDS scan suggest that it is. A smaller zirconium peak from layer beneath surface is evident. No nickel peaks were seen.

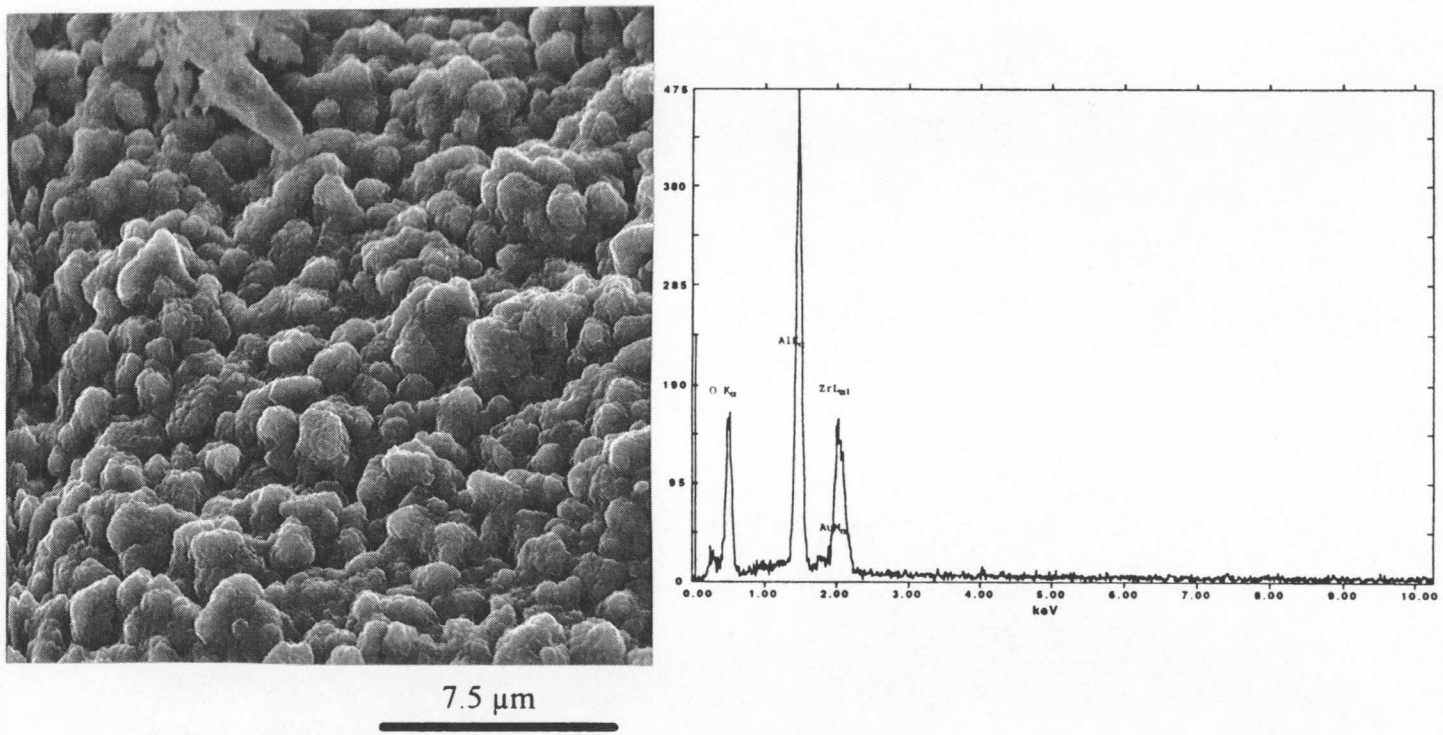

Figure 85: SEM micrograph (4,000X) and EDS scan of coating surface from Figure 84. The EDS scan is virtually identical to that which appeared in Figure 84. The aluminum and oxygen peaks were taken to represent alumina while the zirconium peak was assumed to be due to the underlying zirconia layer.

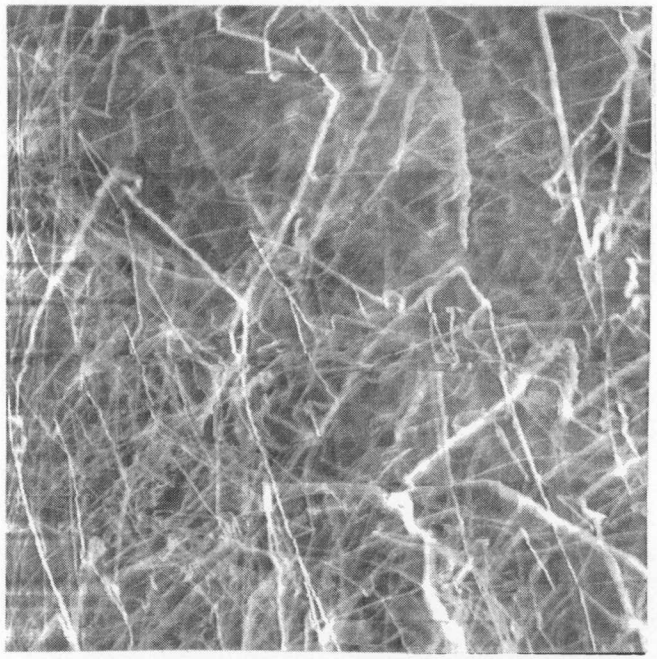

2.5 µm

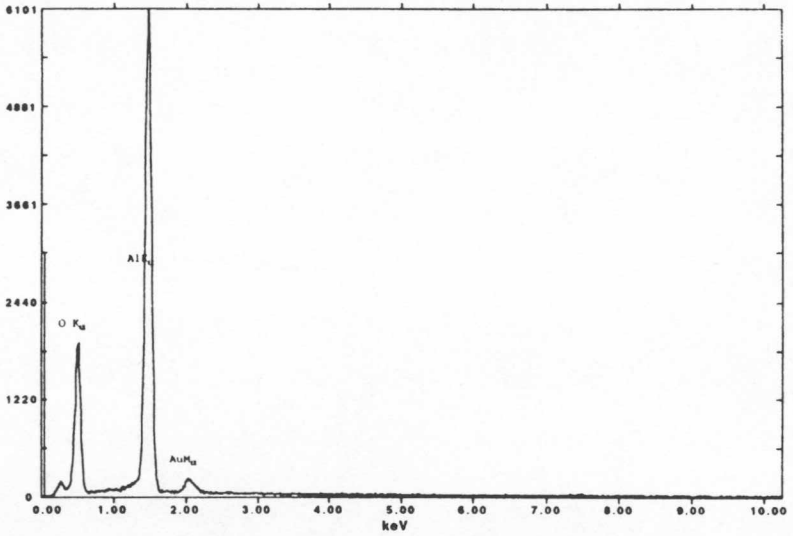

Figure 86: SEM micrograph (12,000X) and EDS scan of ghost-like image from Figure 84. The EDS scan suggests that this thread-like deposit is made up entirely of alumina.

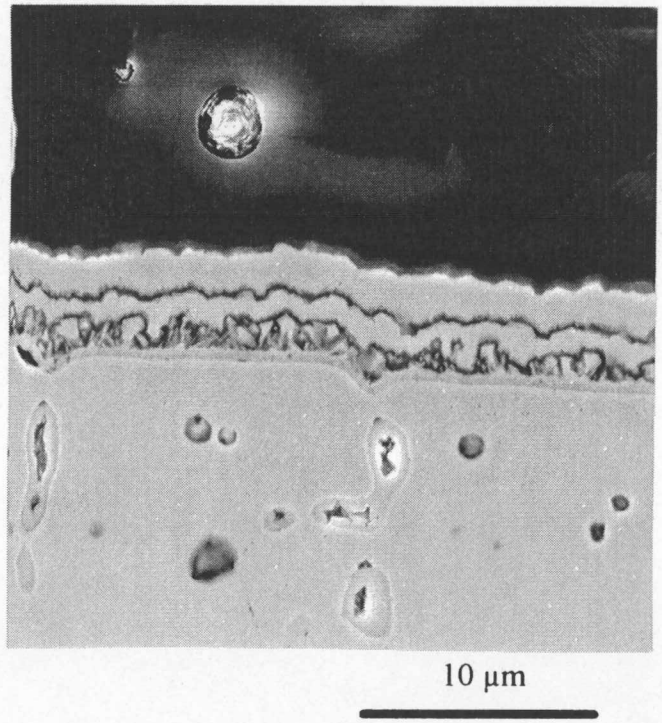

Figure 87: SEM micrograph of sectioned, layered coating (3,000X). Six of eight layers are clearly visible here.

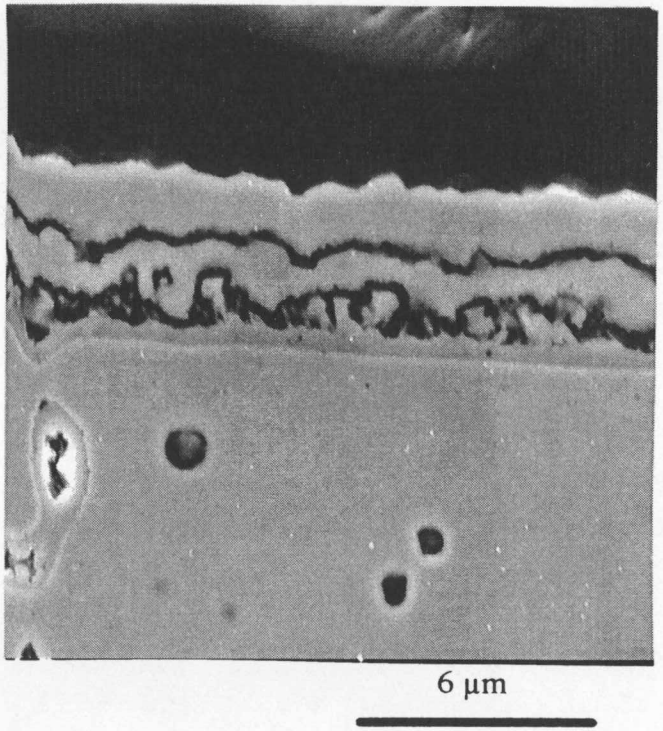

Figure 88: SEM micrograph of sectioned, layered coating (5,000X). Again, six of the eight layers deposited are clearly visible.

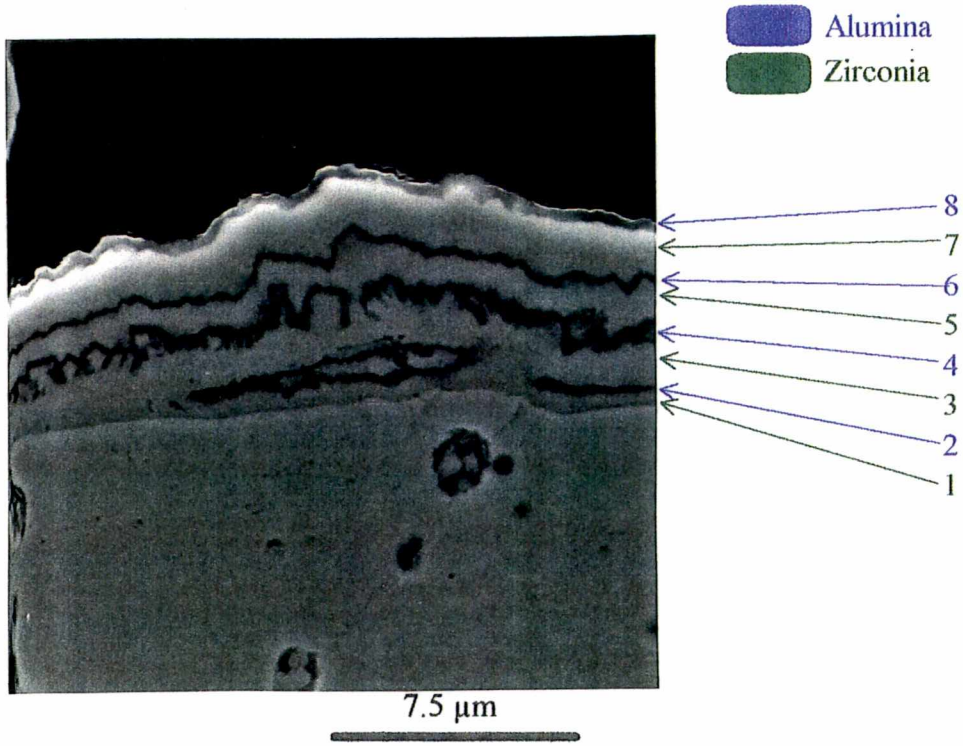

Figure 89: SEM micrograph showing what is believed to be a discontinuous alumina layer (4,000X). It was thought that layers remained reactive after deposition until completely covered by the next layer. This accounts for the absence of eight, continuous layers. Here, are believed to be all eight layers, are enumerated as such in their order of deposition (1-8).

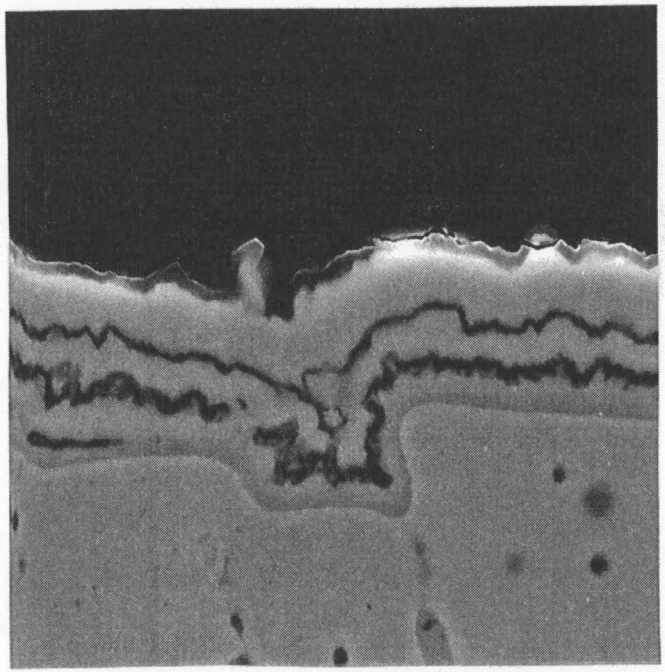

7.5 µm

Figure 90: SEM micrograph of layered coating filling substrate flaw (4,000X). As the deposit filled the flaw, the definition between the alternating layers became blurred.

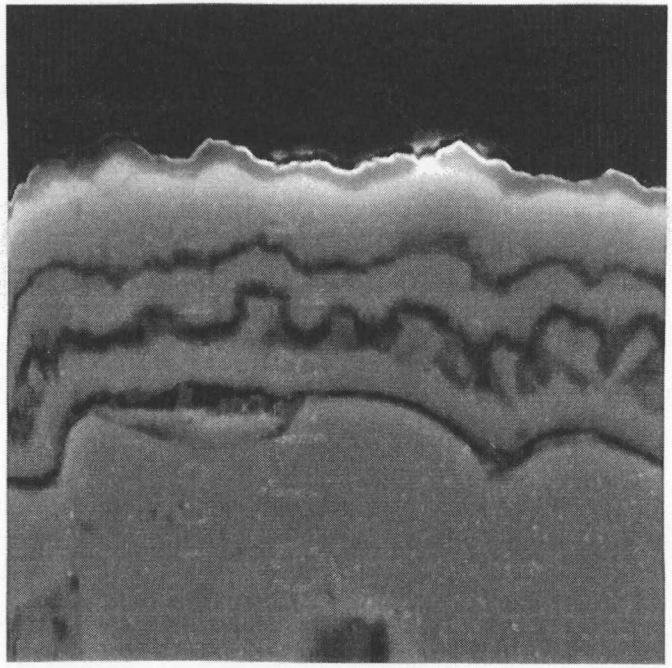

4.3 µm

Figure 91: SEM micrograph of layered coating filling substrate flaws (7,000X). The coating formed in an extremely uniform fashion over substrate flaws, slowly erasing them to form a more even surface.

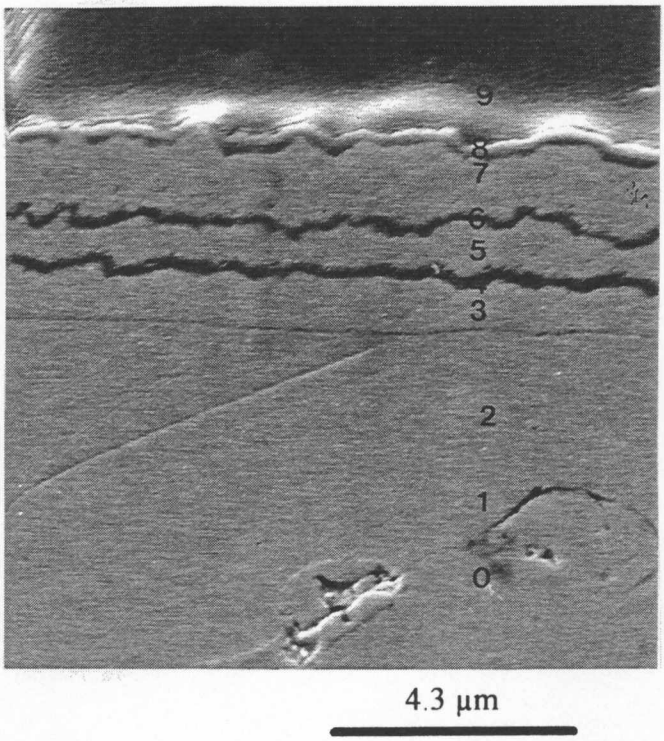

Figure 92: SEM micrograph of mutli-layered coating (7,000X) showing where the sample was examined using spot EDS scans, numbered 0-9.

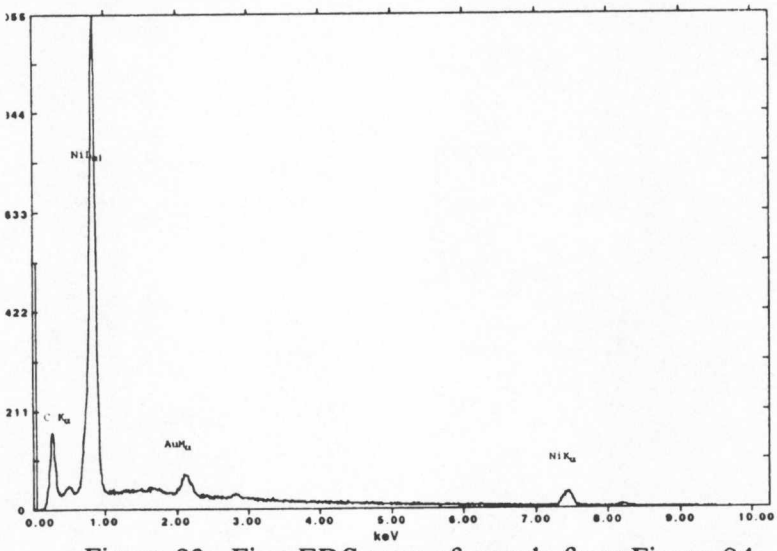

Figure 93: First EDS scan of sample from Figure 94 (number 0). Made on nickel substrate, nickel peaks dominate.

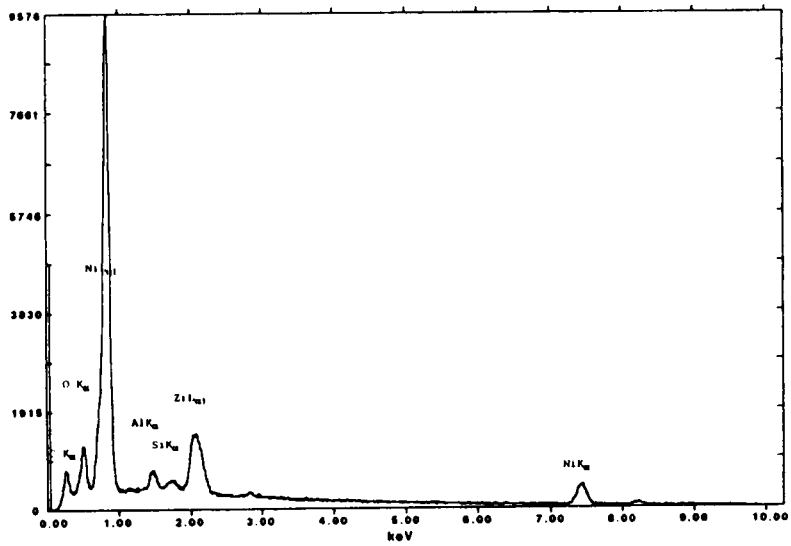

Figure 94: Second EDS scan of sample from Figure 92 (number 1). Made on nickel substrate, nickel peaks dominate. While some Zr, Al and Si were detected, it was thought to be the result of smearing during polishing.

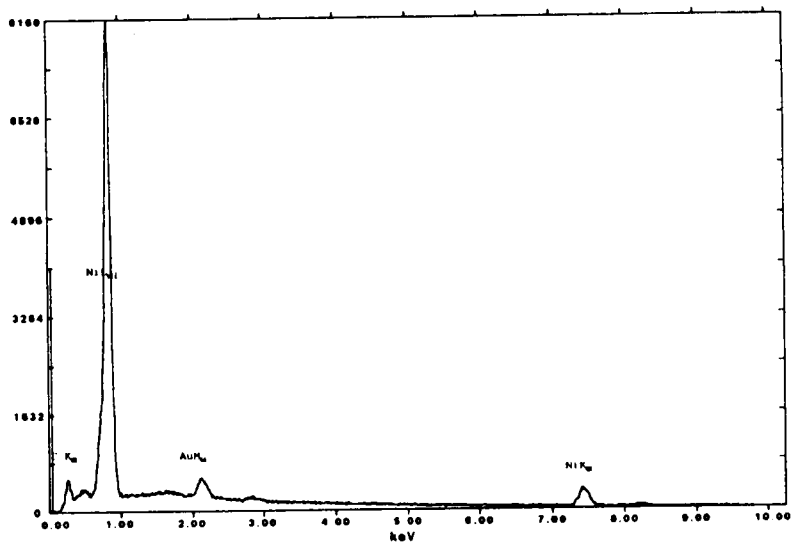

Figure 95: Third EDS scan of sample from Figure 92 (number 2). Again made on nickel substrate with nickel peaks dominating.

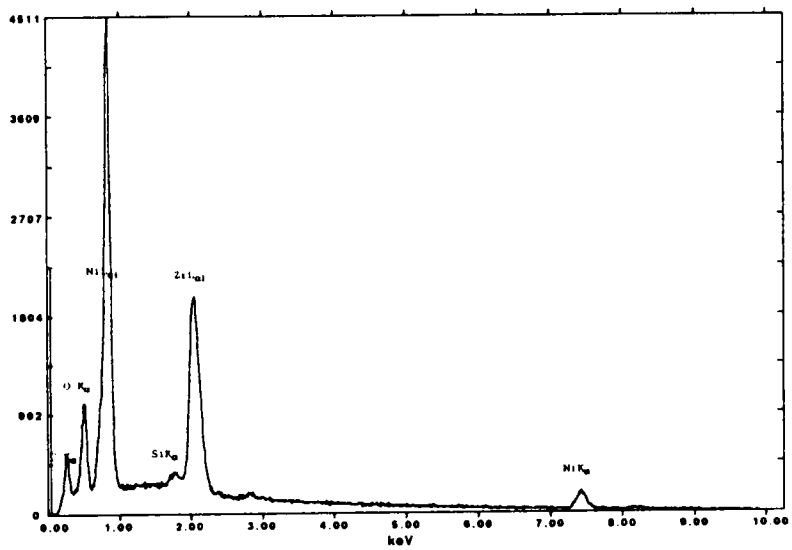

Figure 96: Fourth EDS scan of sample from Figure 92 (number 3). Made on first zirconia layer. There is a strong zirconium peak along with oxygen (taken to be zirconia). The scan was near the substrate and nickel was detected.

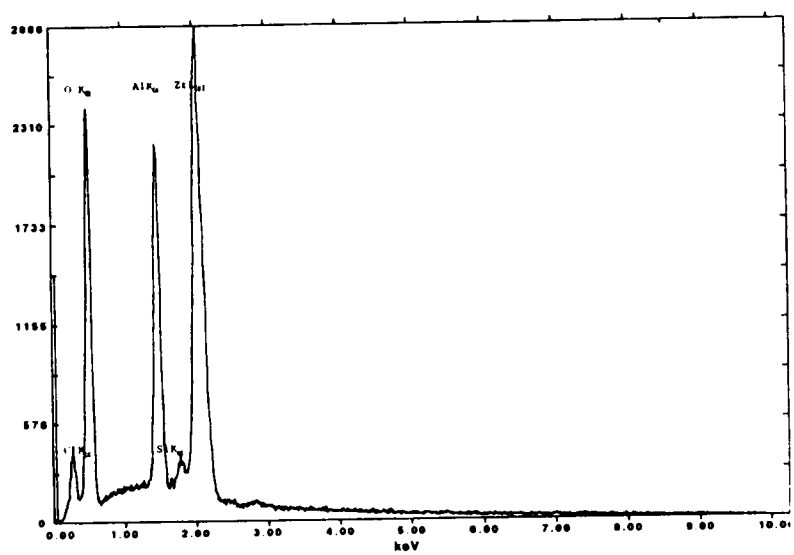

Figure 97: Fifth EDS scan of sample from Figure 92 (number 4). Made on second layer (first alumina layer) there was a strong aluminum peak. This layer was thin and this resulted in an overlap, causing the zirconium peak.

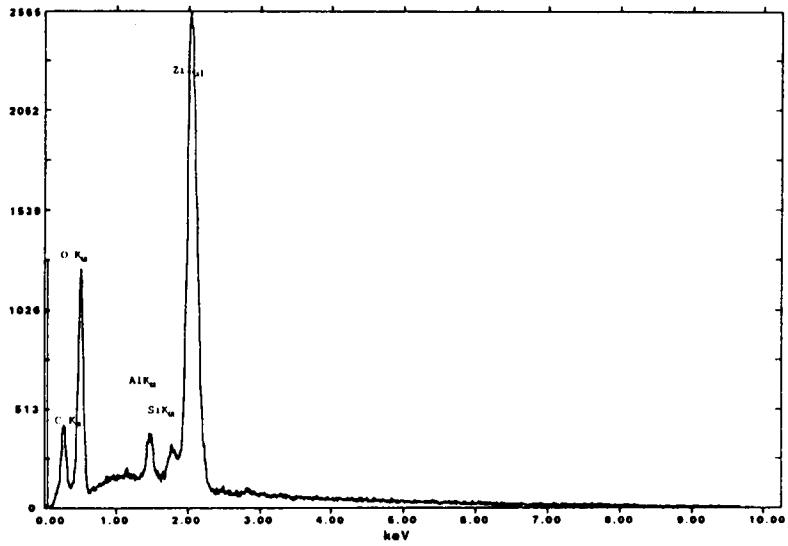

Figure 98: Sixth EDS scan of sample from Figure 92 (number 5). Made on second zirconia layer. Again, there was a strong zirconium peak. The aluminum peak, which appeared strong in Figure 97, has dropped substantially.

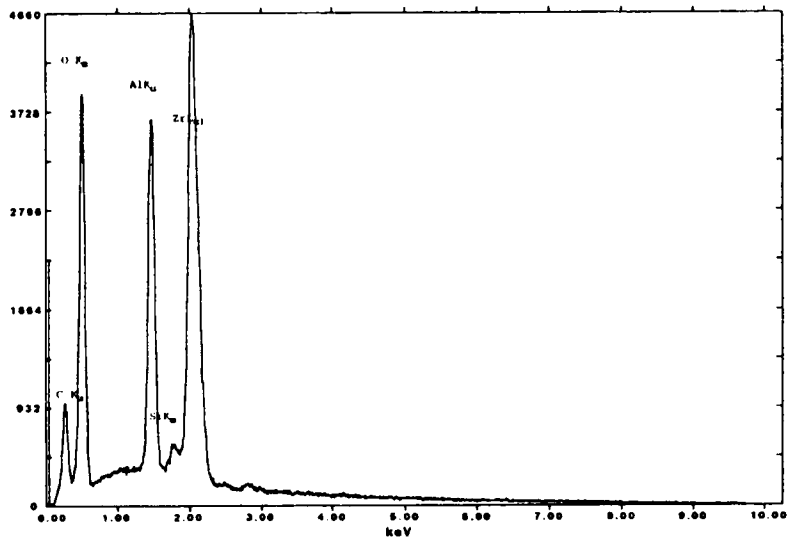

Figure 99: Seventh EDS scan of sample from Figure 92 (number 6). Made on second layer of alumina, there was rebound in the strength of the aluminum peak. The zirconium peak remained strong due to the thinness of the alumina layer.

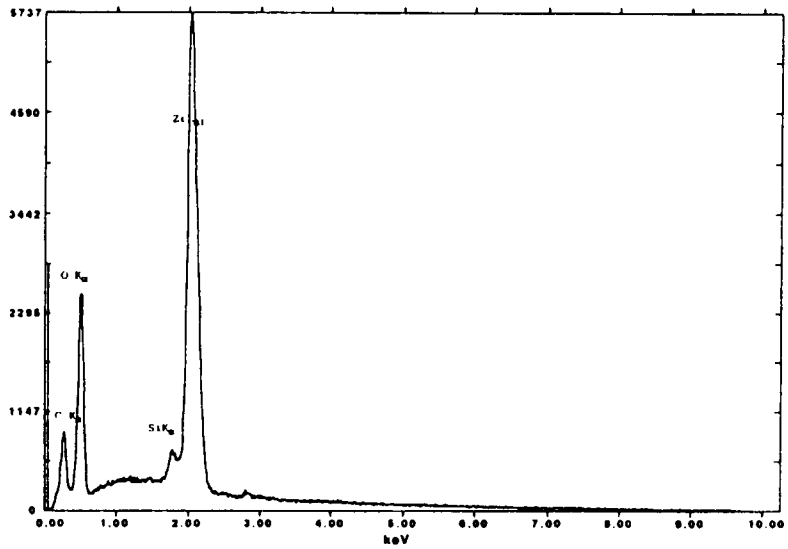

Figure 100: Eighth EDS scan of sample from Figure 92 (number 7). Made on third zirconia layer. Again, there are strong zirconium and oxygne peaks. No aluminum was detected.

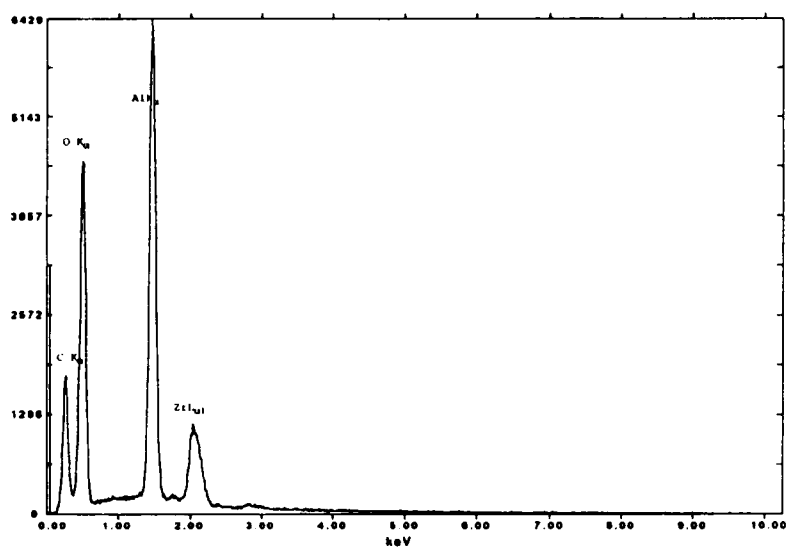

Figure 101: Ninth EDS scan of sample from Figure 92 (number 8). Made on top layer (last alumina layer) there was a strong aluminum peak. The peak labeled as zirconium may be a gold peak from the conductive coating.

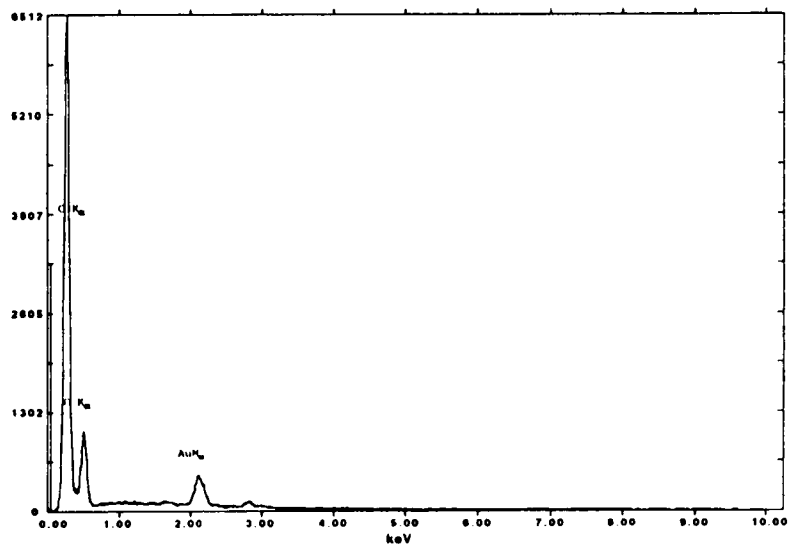

Figure 102: Tenth and final EDS scan of sample from Figure 92 (number 9). Made on the epoxy mounting, only carbon, oxygen and gold were detected. No sign of either aluminum or zirconium was detected.

VITA

Mark Borst was born in Memphis, Tennessee on November 21, 1963. In 1969, he and his family moved to Barrington, Illinois, where he attended elementary school at St. Annes Catholic School. He graduated from Barrington Consolidated High School in May, 1982 and attended The University of Southern California (USC) in Los Angeles, California where he majored in Biomedical and Electrical Engineering, minoring in Chemistry. While at USC, he was a Varsity oarsman with the USC Rowing Club. In addition, he attended International Summer School at the University of Cambridge in Cambridge, England, studying Shakespearian literature and European Economics. He left USC before being awarded his degree and began work at the Oncology unit of Johns Hopkins Hospital in Baltimore, Maryland. During this time he continued his engineering studies at Johns Hopkins School of Continuuing Studies in Baltimore, Maryland. He returned to school fulltime in 1991 at Loyola College in Baltimore, Maryland. He received his B.S. in Engineering Science with an emphasis on materials from Loyola in 1993. That same year, he began his graduate studies at the University of Tennessee, Knoxville (UTK). He received his M.S. degree in Metallurgical engineering from UTK in 1995. Following the completion of his graduate studies, Mr. Borst began work as a Program Mananger, Level 1, at GROVE Worldwide in Shady Grove, Pennsylvania.

GROVE Worldwide is the world leader in the manufacture of mobile hydraulic lifting equipment.